Summer 8-31-2009

Electrical and optical properties of carbon nanotube intra-connects and conductive polymers

Seon Woo Lee
New Jersey Institute of Technology

ABSTRACT

ELECTRICAL AND OPTICAL PROPERTIES OF CARBON NANOTUBE INTRA-CONNECTS AND CONDUCTIVE POLYMERS

by
Seon Woo Lee

Growth of individual carbon nanotube (CNT) intra-connects (bridges) between two pre-fabricated electrodes is a great challenge and a pre-requisite to the development of single electron devices. In this thesis, CNT intra-connects were fabricated and studied. Later on, the intra-connects were deposited with electrically conductive polymer (ECP) in the realization of CNT/ECP hybrids.

The process started by realizing two electrodes with sharp end on a silicon wafer using e-beam lithography. The intra-connects were then grown by use of chemical vapor deposition (CVD) technique. The intra-connects were later electroplated by various conductive polymers. The morphology, electrical conductivity of these intra-connects as well as their Raman spectroscopy signatures were studied. Scanning electron microscopy (SEM) was also employed. The CNT intra-connects were well-aligned from tip to tip. Their Raman spectra indicated the existence of CNT channels between metal tips and nowhere else on the wafer. Enhancement of photoconductance has been shown to correlate with a novel negative differential resistance (NDR) effect. Electroplated intra-connects exhibited unique properties both for multi-walled and single-walled carbon nanotube channels.

ELECTRICAL AND OPTICAL PROPERTIES OF CARBON NANOTUBE INTRA-CONNECTS AND CONDUCTIVE POLYMERS

by
Seon Woo Lee

A Dissertation
Submitted to the Faculty of
New Jersey Institute of Technology
in Partial Fulfillment of the Requirements for the Degree of
Doctor of Philosophy in Electrical Engineering

Department of Electrical and Computer Engineering

August 2009

APPROVAL PAGE

ELECTRICAL AND OPTICAL PROPERTIES OF CARBON NANOTUBE INTRA-CONNECTS AND CONDUCTIVE POLYMERS

Seon Woo Lee

Dr. Haim Grebel, Dissertation Advisor — Date
Professor of Electrical and Computer Engineering, NJIT

Dr. Andrei A. Sirenko, Committee Member — Date
Associate Professor of Physics, NJIT

Dr. Leonid Tsybeskov, Committee Member — Date
Professor of Electrical and Computer Engineering, NJIT

Dr. Kenneth S. Sohn, Committee Member — Date
Professor of Electrical and Computer Engineering, NJIT

Dr. Durgamadhab Misra, Committee Member — Date
Professor of Electrical and Computer Engineering, NJIT

BIOGRAPHICAL SKETCH

Author: Seon Woo Lee

Degree: Doctor of Philosophy

Date: August 2009

Undergraduate and Graduate Education:

- Doctor of Philosophy in Electrical Engineering,
  New Jersey Institute of Technology, Newark, NJ, 2009
- Master of Science in Electrical Engineering,
  New Jersey Institute of Technology, Newark, NJ, 2004
- Bachelor of Science in Electronics Engineering,
  Kwangwoon University, Seoul, Republic of Korea, 2001

Major: Electrical Engineering

Publications:

S. W. Lee, D. Lopez, A. Kornblit, S. V. Rotkin, A. A. Sirenko, and H. Grebel, "Gate-controlled negative resistance and photoconductance enhancement of individually addressable carbon nanotube intra-connect," Nano Letters, 9(4), 1369-1373, 2009.

S. W. Lee, H. Grebel, A. Kornblit and D. Lopez, "Electrical and optical properties of carbon nanotube/polypyrrole addressable intra-connects," Synthetic Metals, 159, 462-466, 2009.

S. W. Lee, A. Kornblit, D. Lopez and H. Grebel, "Optical sensor based on individually addressable carbon nanotube intraconnect and polycarbazole," Materials Research Society (MRS) Proceedings, Fall 2008.

S. W. Lee, A. Kornblit, D. Lopez, S. V. Rotkin, A. A. Sirenko, and H. Grebel, "Gate-controlled negative resistance and photoconductance enhancement of individually addressable carbon nanotube intra-connect," Materials Research Society (MRS) Proceedings, Fall 2008.

S. W. Lee, D. Katz, A. Kornblit, D. Lopez and H. Grebel,
"Synthesis of controllably grown carbon nanotubes interconnects," Materials Research Society (MRS) Proceedings, Spring 2007.

D. Katz, S. W. Lee, D. Lopez, A. Kornblit and H. Grebel,
"Synthesis of carbon nanotubes: controlled interconnects growth," J. Vac Sci. and Tech. B, 25, 1191-1195, 2007.

J. Chen, S. W. Lee and H. Grebel,
"Controlled growth of single-wall carbon nanotubes within three-dimensional silica templates," Carbon, 44, 608-610, 2006.

Presentations:

S. W. Lee and Haim Grebel,
"Gate controlled negative differential resistance and photoconductivity enhancement in carbon nanotube intra-connects," The Dana Knox Student Research Showcase, NJIT, New Jersey, April 8, 2009.

S. W. Lee and Haim Grebel,
"Gate controlled negative differential resistance and photoconductivity enhancement in carbon nanotube intra-connects," NJIT Advance Research Showcase, NJIT, New Jersey, March 30, 2009.

S. W. Lee, A. A. Sirenko, D. Lopez, A. Kornblit and Haim Grebel,
"Carbon nanotube intra-connects with conductive polymers," American Physical Society (APS), Pittsburgh, PA, March 2009.

S. W. Lee, S. V. Rotkin, A. A. Sirenko and Haim Grebel,
"Gate controlled negative differential resistance and photoconductivity enhancement in carbon nanotube intra-connects," American Physical Society (APS), Pittsburgh, PA, March 2009.

S. W. Lee, A. Kornblit, D. Lopez and H. Grebel,
"Optical sensor based on individually addressable carbon nanotube intraconnect and polycarbazole," Materials Research Society (MRS), Fall 2008.

S. W. Lee, A. Kornblit, D. Lopez, S. V. Rotkin, A. A. Sirenko, and H. Grebel,
"Gate-controlled negative resistance and photoconductance enhancement of individually addressable carbon nanotube intra-connect," Materials Research Society (MRS), Fall 2008.

S. W. Lee and H. Grebel,
"Single electron devices based on as-grown individual carbon nanotube bridges and conductive polymers," Fourth Annual Provost's Student Research Showcase, First Prize (Graduate Student Division), NJIT, New Jersey, April 9, 2008.

S. W. Lee, H. Grebel, D. Katz, D. Lopez and A. Kornblit,
"Carbon nanotube/conducting polymer addressable intra-connects," Conference on Lasers and Electro-Optics (CLEO) 2007, Baltimore, Maryland, May 2007.

S. W. Lee and H. Grebel,
"Properties of carbon nanotube/conducting polymer addressable intra-connects," WOCC (Wireless and Optical Communications Conference), Outstanding Research Poster Award, First Prize, Newark, New Jersey, April 27-28, 2007.

S. W. Lee and H. Grebel,
"Single electron devices based on as-grown individual carbon nanotube bridges and conductive polymers," Third Annual Provost's Student Research Showcase, NJIT, New Jersey, April 11, 2007.

S. W. Lee, D. Katz, A. Kornblit, D. Lopez and H. Grebel,
"Synthesis of controllably grown carbon nanotubes interconnects," Materials Research Society (MRS), Spring 2007.

To My Beloved Parents, Sun-Nam An and Byung-Wan Lee
For Their Encouragement and Endless Love.

ACKNOWLEDGMENT

I would like to give my special thanks and appreciation to my advisor, Prof. Haim Grebel for providing me full support and guidance throughout my PhD study, not only as an academic supervisor but also as a great mentor in life. He has always been available to discuss matters and to advise me. I truly appreciate Prof. Andrei Sirenko for valuable advice and continuous encouragement during my study, giving me knowledge on physics and helping me with optical experiments. Thanks to my PhD dissertation committee members, Dr. Leonid Tsybeskov, Dr. Kenneth S. Sohn, Dr. Durgamadhab Misra for serving as my dissertation committee members.

TABLE OF CONTENTS

TABLE OF CONTENTS
(Continued)

LIST OF FIGURES

LIST OF FIGURES
(Continued)

Figure **Page**

LIST OF FIGURES
(Continued)

LIST OF FIGURES
(Continued)

Figure **Page**

LIST OF FIGURES
(Continued)

Figure **Page**

LIST OF FIGURES
(Continued)

Figure **Page**

CHAPTER 1

INTRODUCTION

Carbon nanotubes (CNTs) and electrically conductive polymers (ECPs) have been extensively studied each for its own merit for various applications in nanotechnology [1-3]. Carbon nanotubes are rolled graphene layers into tubes whose diameter is on the order of 1 nm [4]. ECPs are polymers: unlike most polymers they exhibit conductance of charges and are sometimes called synthetic metals [5].

Since the discovery of CNT by Iijima in 1991 [6], CNTs were considered for biosensors, field effect transistors, single electron transistors, mechanical devices and coatings [1-3, 7, 8], owing to their remarkable electrical, chemical and mechanical properties [9-12].

However, growth of CNT at designated positions has been a great challenge. Most metal contacts to CNTs for device purposes were made after dispersing, or, randomly growing the tubes on the substrates [13]. Otherwise CNTs were randomly grown [14] or mechanically attached [1] between two pre-fabricated electrodes or pads. Such techniques were deemed crude and incompatible with modern integrated circuit (IC) fabrication standards.

Electrically conductive polymers have been discovered in the late nineteen seventies (1977) by Alan Heeger, Hideki Shirakawa and Alan MacDiarmid when conjugated polymer polyacetylene exhibited electrical conductivity through halogen doping [5, 15, 16]. In recent years, electrical and optical properties of conductive polymers were applied to field-effect transistors, gas sensors, batteries, light emitting diodes and flexible optoelectronic devices [17-21]. Typically, ECPs are mechanically weak and

fragile. They are susceptible to oxygen, which degrades its conductance [22, 23]. The strength of ECP may be improved by copolymerization with a second polymer at the expense of conductivity [24]. One of the advantages of ECP is the ability to conjugate them with oligonucleotides, thus making them useful biosensors [25]. The integration of CNT and ECP did not escape researchers, yet, so far, such structures have only been realized as bulk composites [13].

Effective field effect biosensors require narrow channels. Yet, polymers tend to make good films and fabricating narrow channels has been demonstrated only recently [26-28]. One would therefore, consider integrating the CNT and ECP components: grow a narrow CNT channel and electroplate it with ECP for the realization of an efficient biosensor. A schematic of such element is shown in Figure 1.1. It is made of as-grown CNT channel between two electrodes (Figure 1.1a). The electrodes and the CNT are then used to electroplate the ECP component (Figure 1.1b).

In Chapter 2, a brief introduction to carbon nanotubes, electrically conductive polymers and negative differential resistance will be given.

Chapter 3 presents the experimental setup for this study, including metal electrode preparation, the growth method of individual CNT intra-connects by chemical vapor deposition (CVD), electro-polymerization process used to wrap the CNT intra-connect with electrically conductive polymer, such as polypyrrole and polycarbazole, current-voltage characteristic measurement setup, material characterization techniques (SEM and AFM) and the system for Raman spectroscopy.

The experimental results are extensively discussed in Chapter 4, 5 and 6. In Chapter 4, multi-walled carbon nanotube (MWCNT) channels, electroplated with polypyrrole were

characterized by electrical and optical techniques. Negative differential resistance was observed for channels made of single-walled carbon nanotube (SWCNT) intra-connects. Details of the experimental results are discussed in Chapter 5 as well. In addition, Chapter 6 describes single-walled carbon nanotube (SWCNT) elements with and without electroplated polycarbazole (PCZ).

Conclusions are provided in Chapter 7. Future Work is suggested in Chapter 8.

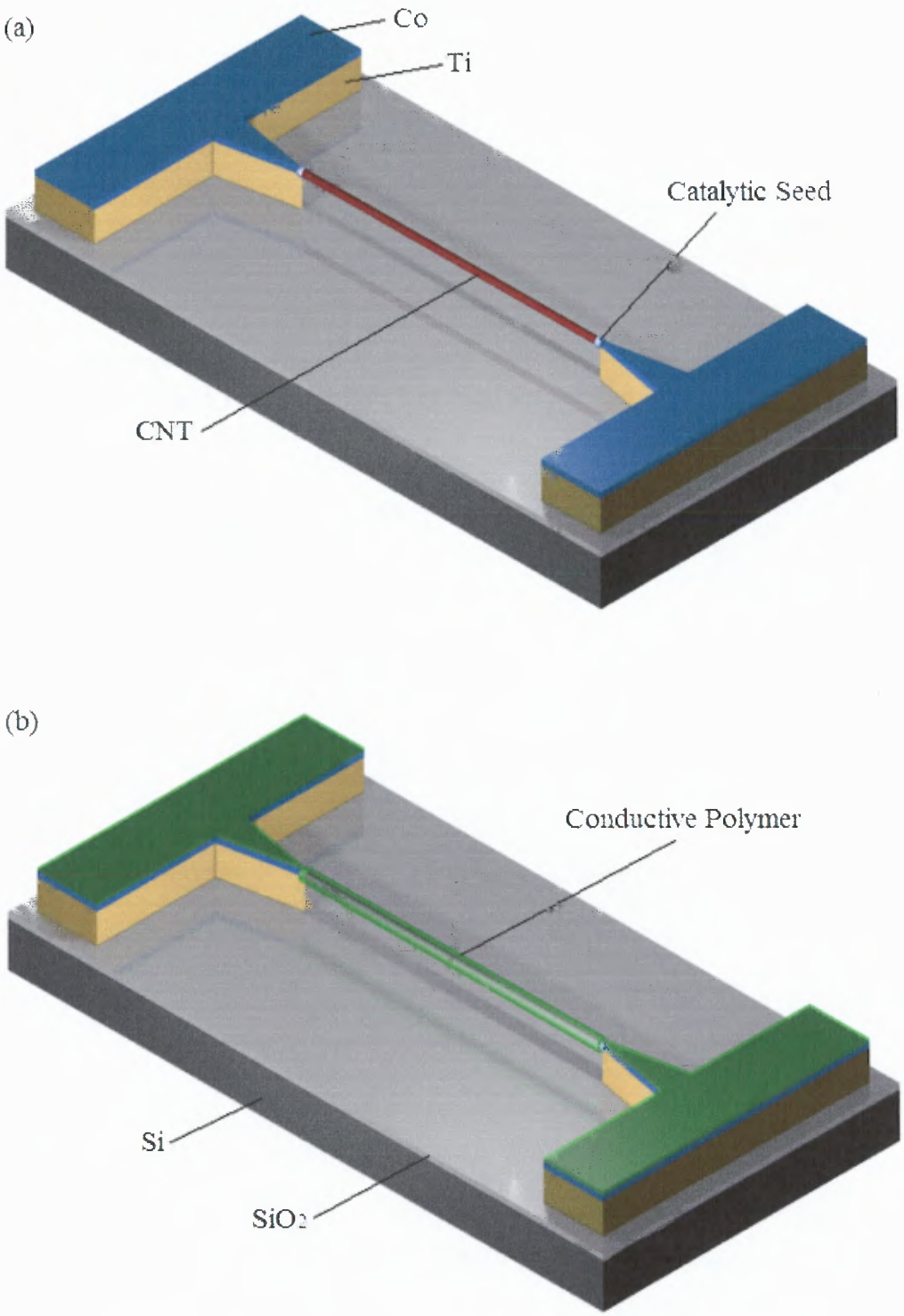

Figure 1.1 Schematics of 1-D device, which is based on CNT/ECP composite bridge. (a) Growth of individual CNT intra-connect between two pre-determined addressable metal tips by CVD. (b) Electro-polymerization of ECP on top of a CNT bridge.

CHAPTER 2

BACKGROUND

2.1 Carbon Nanotubes

Carbon nanotubes are cylindrically symmetric allotrope of carbon. In general, each carbon atom has six electrons in the outermost shell. Two electrons fill the 1*s* orbital and the remaining four electrons fill the sp^3 or, sp^2 orbitals. Such bonds, thus, contribute to the formation of diamond, graphite or graphene, fullerene and carbon nanotube (Figure 2.1) [4].

The sp^3 hybrid orbitals in diamond have four valence electrons for each carbon atom. Four other neighbor carbons are connected to each atom via four σ covalent bonds. This tetrahedral structure makes diamond the hardest material known. The electrons in diamond are tightly bounded, which makes diamond an insulator [29].

Graphite has planar hexagonal structure, which is composed of three electrons in planar sp^2 hybrid orbitals and one electron in an out-of-plane π orbital. The electrons in out-of-plane π orbital are loosely held on the graphite plane and contribute to its electrical conductivity [30]. A monolayer of graphite is called graphene.

Carbon nanotube is a rolled graphene sheet to form a cylindrical hollow tube. Nanotubes also have sp^2 orbitals. However, the σ and π bonds are rehybridized in carbon nanotubes since the σ bonds are a bit out of plane and the π bonds are out-of-plane as well. This structure makes carbon nanotubes mechanically stronger and more electrically conductive than graphene. Figure 2.2 shows transmission electron microscope (TEM) image of carbon nanotubes [4].

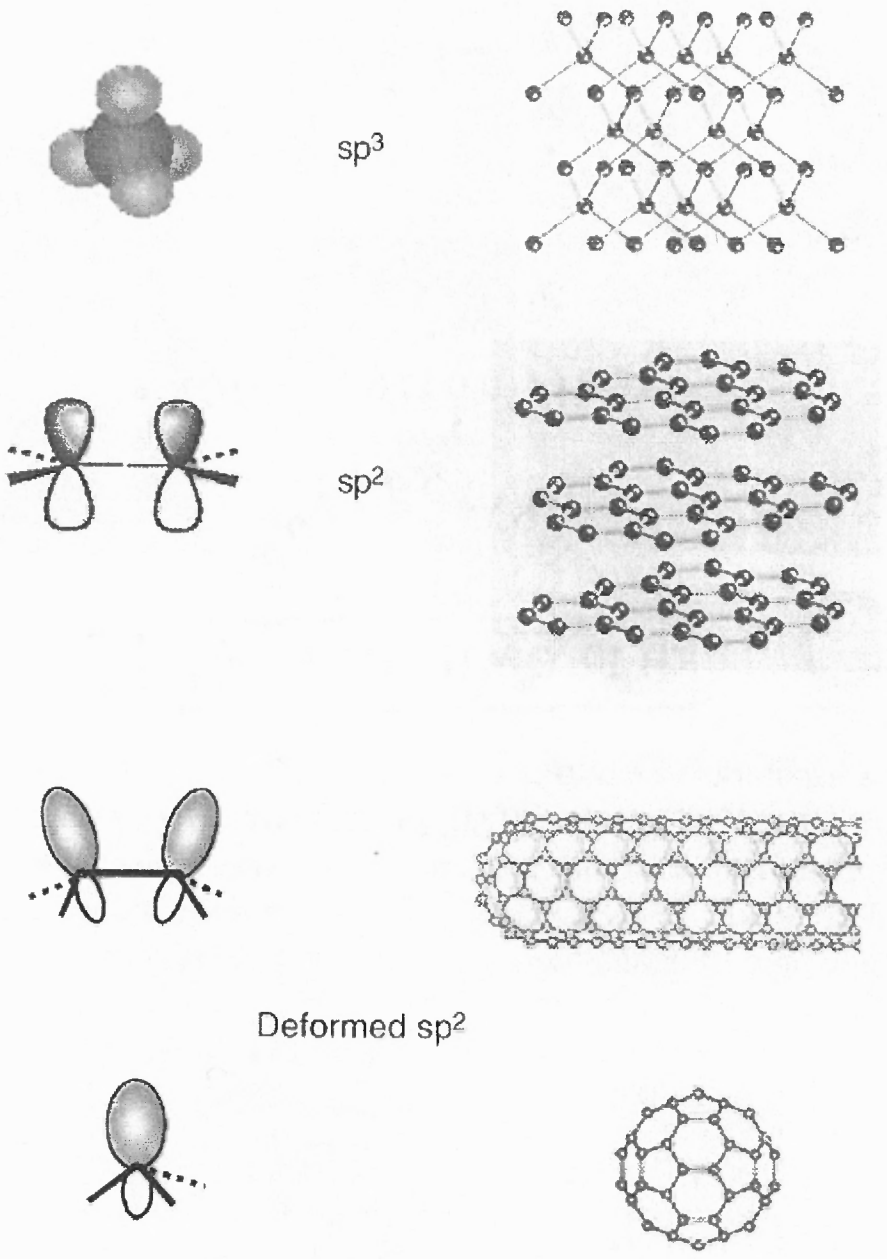

Figure 2.1 The bonding structures of carbon allotropes, diamond, graphite, carbon nanotube, fullerene. Deformed sp^2 structures give carbon nanotubes unique mechanical, electronic, optical and chemical properties [4].

Fullerenes, also known as buckyballs, are large molecular clusters [31]. Soccer ball shaped C_{60} structure is made of 20 hexagons and 12 pentagons. Fullerenes have deformed sp^2 structure with high curvature, which results in interesting physical properties [32].

Carbon nanotubes may be either metallic or semiconducting depending on their morphology [11, 33, 34]. Single-walled carbon nanotubes have direct band gap and quasi one-dimensional band structure, which makes carbon nanotubes applicable for optoelectronics. Bonding structures of carbon nanotubes make them biologically and chemically active [35, 36] more than graphite or, graphene [4, 12]. Current size limitation in silicon technology turned many to carbon nanotubes: their nanometer diameter and conductance properties raised hopes of realizing nano-size field effect devices.

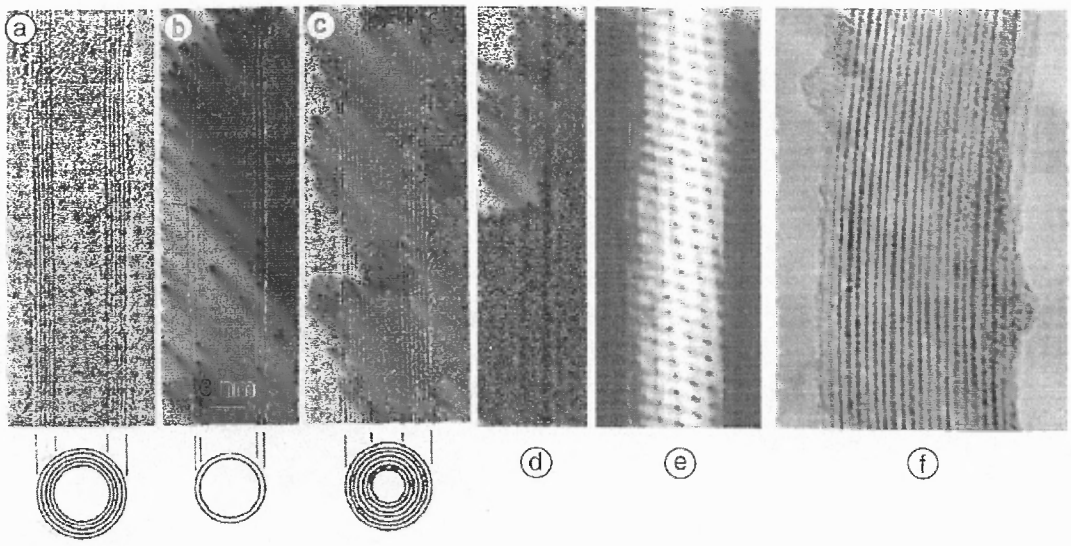

Figure 2.2 Images of carbon nanotubes [4] (a), (b) and (c) multi-walled carbon nanotubes [6] (d) STM image of single walled carbon nanotube [37] (e) SWCNT - TEM image [38] (f) SWCNT ropes [39].

2.1.1 Synthesis of Carbon Nanotube

There are various ways to grow carbon nanotubes: thermal chemical vapor deposition (CVD), plasma enhanced chemical vapor deposition (PECVD), carbon arc discharge method and laser ablation [40].

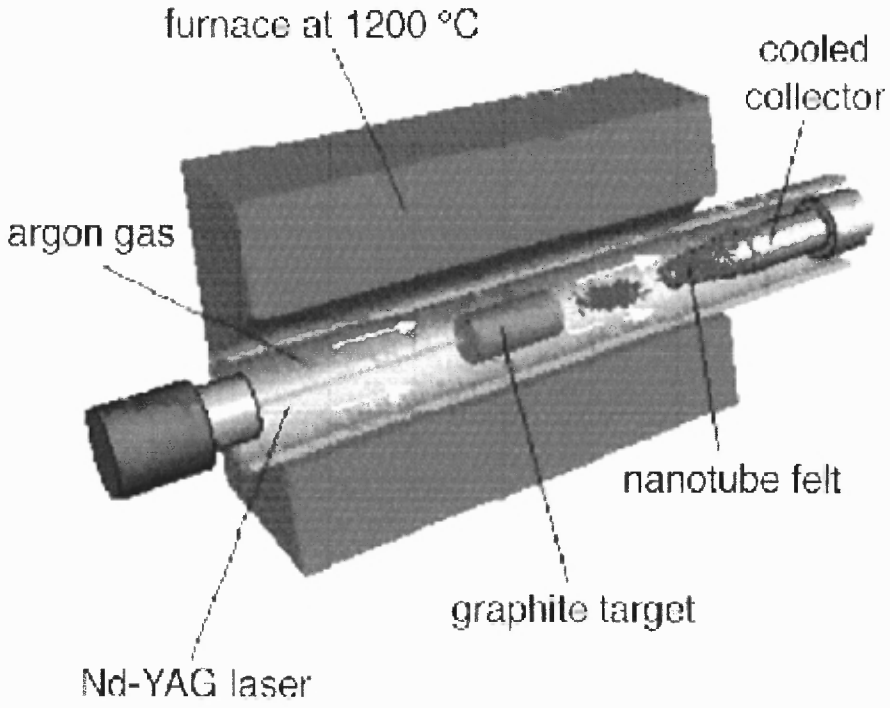

Figure 2.3 Laser vaporization method is employed in the growth of single-walled carbon nanotube using quatz tubes at 1200 °C, a graphite target and a water-cooled copper collector [41].

Arc discharge method was developed to produce macroscopic amount (~several grams) of carbon nanotubes by Fundamental Research Laboratory at NEC Corporation in Japan. Voltage bias, of approximately 20 V, is applied between carbon rods, which are separated by a distance of 1 mm. Carbon atoms are evaporated from the positive electrode at high temperatures, and the growth starts on the negative electrode. Transition metals such as cobalt, nickel, or, iron are required for the growth of single-walled carbon

nanotubes (SWCNT). Catalyst is not necessary for the growth of multi-walled carbon nanotubes. This method requires purification process to separate carbon nanotubes from impurities (catalysts) and soot [42].

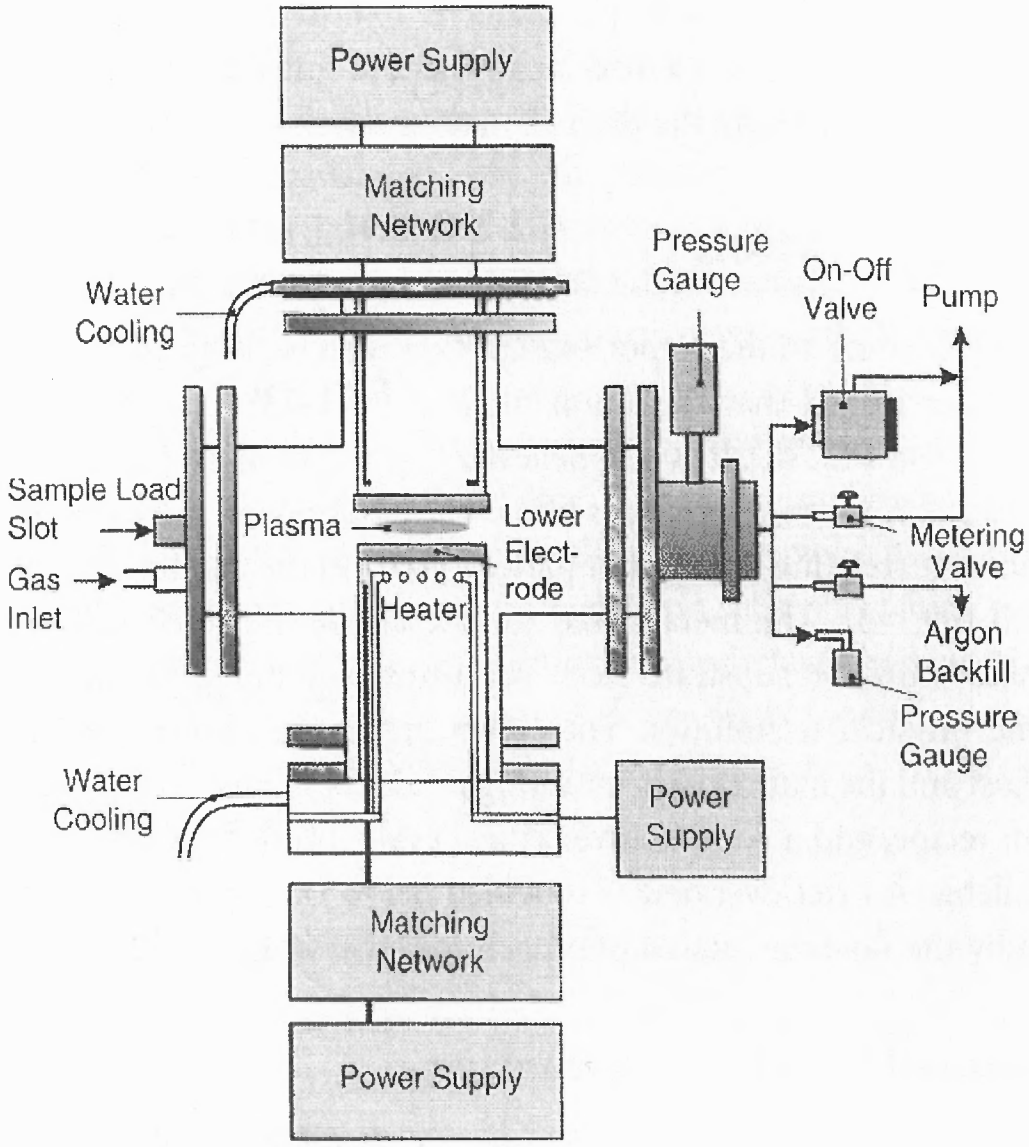

Figure 2.4 Schematic for Plasma Enhanced Chemical Vapor Deposition (PECVD) technique [4].

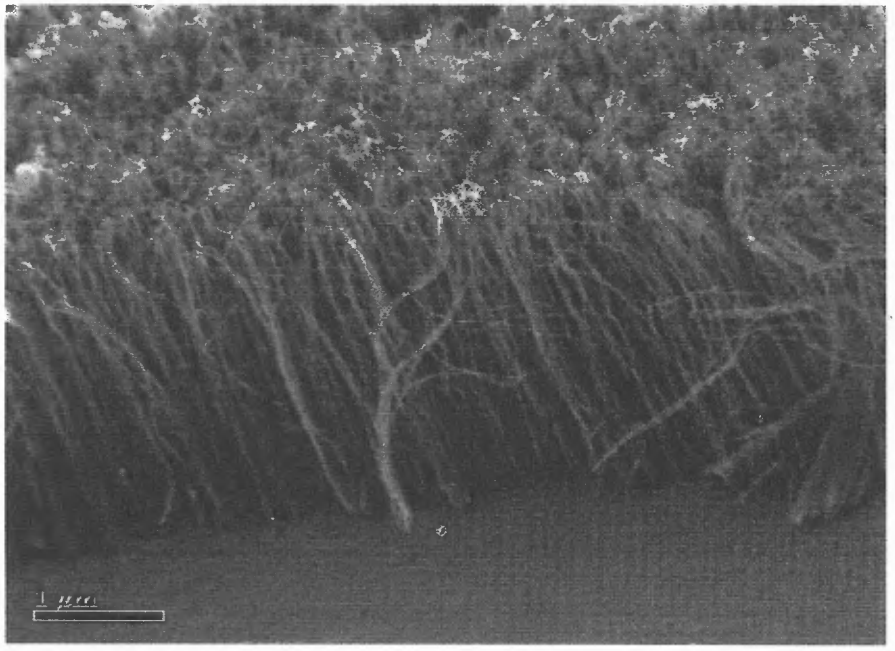

(a)

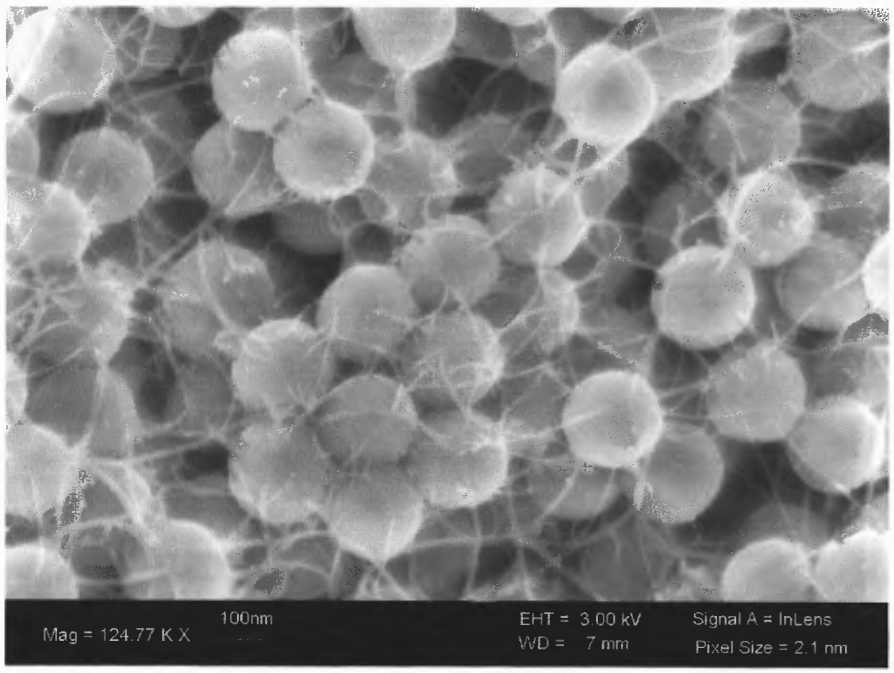

(b)

Figure 2.5 Images of carbon nanotubes (a) Vertically aligned MWCNT grown by PECVD using CH_4/H_2 [4] (b) Randomly grown carbon nanotubes by CVD using carbon monoxide gas as a precursor.

Laser evaporation with intense pulses is another method to grow carbon nanotubes [43, 44]. Targets are prepared by uniformly mixing nickel, cobalt and graphite. The graphite target is heated up to 1200 °C. The laser pulses evaporate the carbon atoms in the target. This method reduces the amount of contamination in a form of soot, or, amorphous carbon. Carbon nanotubes with diameters of 10-20 nm and up to 10 μm long may be grown by this method.

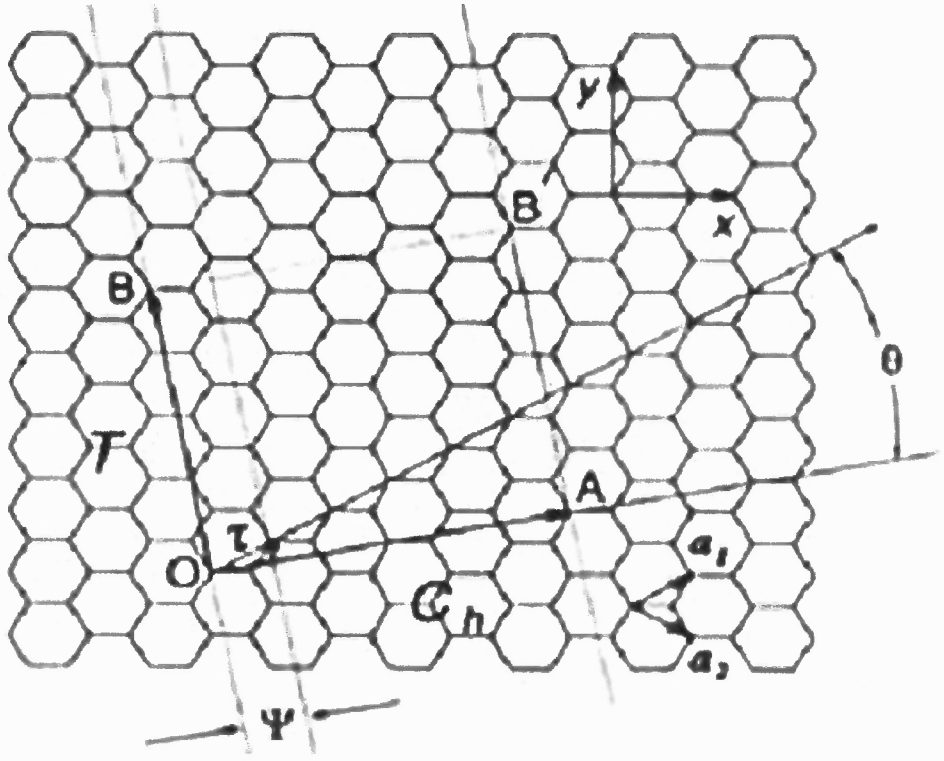

Figure 2.6 A carbon nanotube is a two-dimensional rolled-up graphene sheet. The vector OA is defined as a chiral vector, $C_h = n\hat{a}_1 + m\hat{a}_2$, where $\hat{a}_1$ and $\hat{a}_2$ are unit vectors on the hexagonal structure, n and m are integers. The chiral angle , θ, defines the angle between the unit vector $\hat{a}_1$ (the zigzag direction) and the vector OA (the chiral vector C_h) [12].

Chemical Vapor Deposition (CVD) is a widely used technique to grow carbon nanotubes. It requires a flow of hot carbon feedstock in a form of gas containing carbon. Most commonly used gases are ethylene, methane, carbon monoxide and ethanol.

Transition metal catalytic layers are deposited on the substrate in order to initiate tube's growth. Iron (Fe), cobalt (Co), nickel (Ni) are used as metal catalysts. The size of metal particles dictates the diameter of the resultant carbon nanotubes [45, 46]. Typical temperature range is within 700 °C - 1000 °C. The growth of CNT by CVD is rather random in terms of position and direction. Efforts to align the tubes were made by applying a large electric field [47]. The growth position is typically dictated by the position of catalytic seeds. In this thesis we show that by defining the catalytic seed to be at a sharp tip of an electrode, one may control the place at which the tubes are grown.

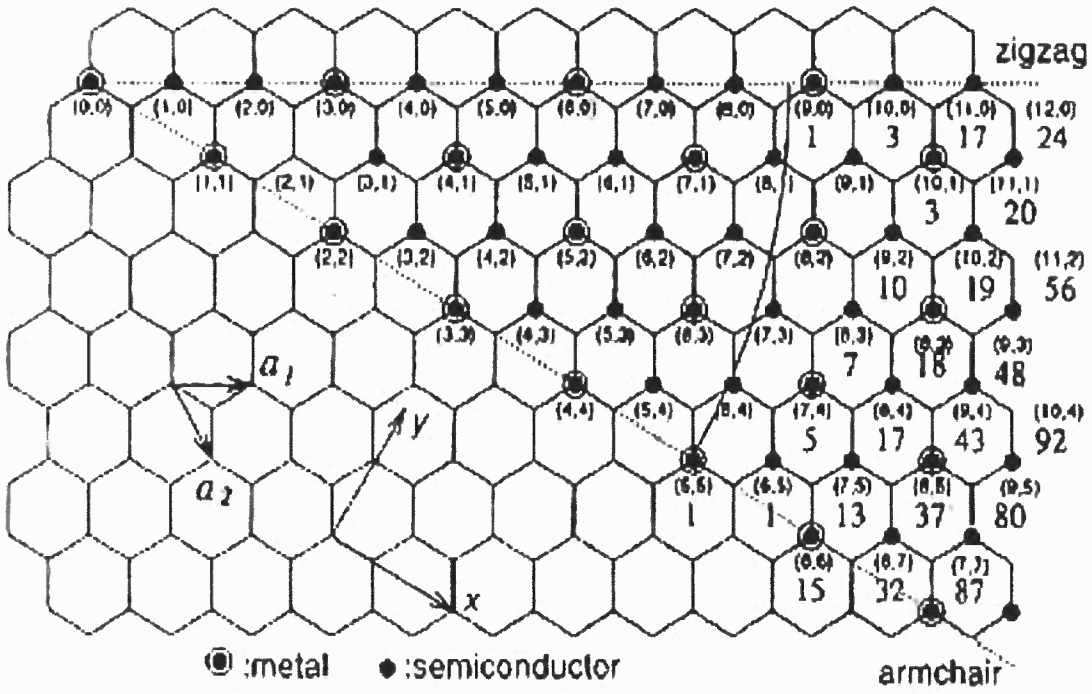

Figure 2.7 The integer set (n,m) will describe different types of carbon nanotubes. Zigzag carbon nanotube can be expressed as the vector (n,0) or (0,m), which denotes zero degree chiral angle. (n,n) states armchair carbon nanotubes. All other integer sets (n,m) states chiral carbon nanotubes with a chiral angle between 0° and 30°. Carbon nanotubes can be either semiconducting or metallic depends on their chirality [12].

A modification to thermal CVD is plasma enhanced CVD (PECVD). The plasma may be generated by a DC or AC, electric or magnetic fields. The plasma enhances the tube's growth and typically results in vertically grown tubes. The carbon nanotube growth follows the direction of the externally applied electric field. For example, a DC plasma reactor, consisting of ground and positive electrodes is shown in Figure 2.4. Pressure levels employed are normally in the range of 1 to 20 Torr.

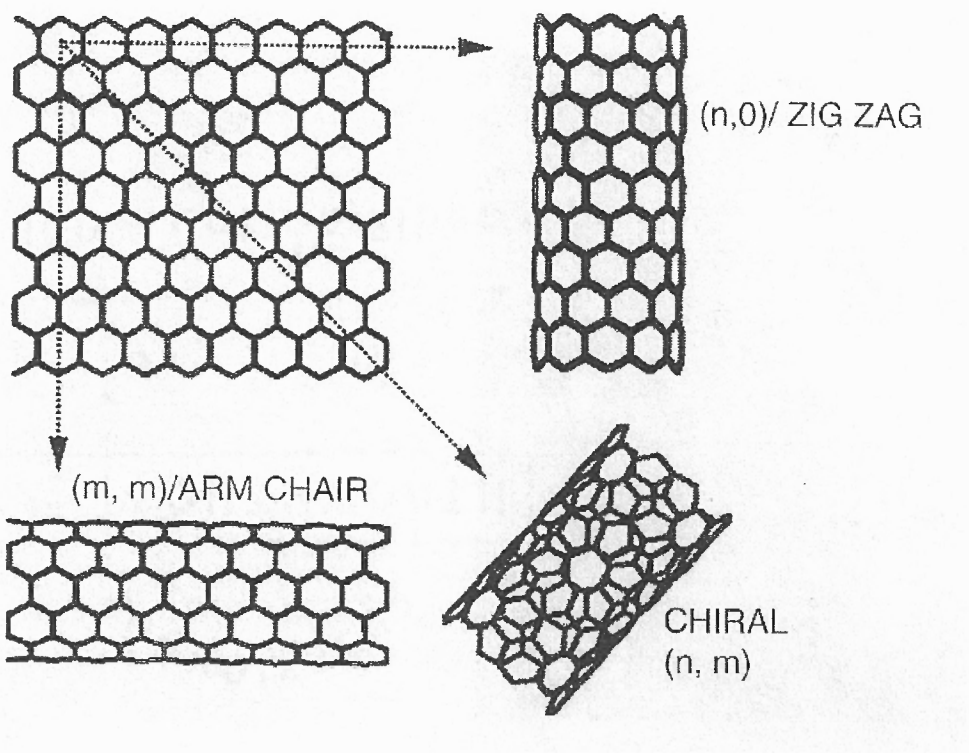

Figure 2.8 Some structures of single-wall carbon nanotubes (a) armchair nanotube, chiral angle $\theta = 30^{\circ}$ and chiral vector (n,n) (b) zigzag nanotube, chiral angle $\theta = 0^{\circ}$ and chiral vector $(n,0)$ (c) chiral nanotube, chiral angle $0^{\circ} < \theta < 30^{\circ}$ and chiral vector (n,m) [12].

In this study, chemical vapor deposition process was used to grow carbon nanotubes with various gases at different temperatures. Details of the chemical vapor deposition process are provided in Chapter 3.

2.1.2 Structure of Carbon Nanotubes

A graphene sheet is a monolayer of graphite. Carbon nanotubes are seamless cylindrical rolled-up graphene sheet (Figure 2.6). The rolling orientation of carbon nanotube (CNT) is called chirality. The physical properties of carbon nanotubes are determined by their chirality factor. Two dimensional hexagonal structures may be expressed by a chiral vector

$$C_h = n\hat{a}_1 + m\hat{a}_2 \tag{2.1}$$

Here n and m are integers and $\hat{a}_1$ and $\hat{a}_2$ are unit vectors of the hexagonal lattice. Chiral vector states the rolling direction of a graphene sheet when forming a hollow tube. A chiral vector is usually expressed by its integer set (n,m) [48]. The chiral angle θ is defined as an angle between the chiral vector C_h and the zigzag nanotube direction (Figure 2.6). The rectangular unit cell of a graphene sheet is composed of a vector T and chiral vector C_h. The chiral vectors (n,m) are used to specify the different types of carbon nanotubes. The chiral vectors $(n,0)$ and $(0,m)$ define zigzag carbon nanotubes, which refer to a chiral angle of zero degrees. Armchair carbon nanotubes may be expressed by the vector (n,n) with a chiral angle of θ=30°. All other (n,m) carbon nanotubes in the range of $0° < \theta < 30°$ are simply referred to as chiral carbon nanotubes (Figure 2.8). The diameter of carbon nanotubes may be calculated from the chiral vector (n,m)

$$D = (a\sqrt{m^2 + n^2 + mn})/\pi \tag{2.2}$$

Here D is the diameter of carbon nanotube and a is the lattice constant (2.49 angstroms, see also Figure 2.6). The chiral angle θ is calculated using the relation

$$\tan\theta = (\sqrt{3}m)/(2n+m)\,. \tag{2.3}$$

Carbon nanotubes appear in two flavors: metallic and semiconducting (Figure 2.7). Carbon nanotube becomes metallic when its chiral vectors satisfy the condition,

$$n - m = 3q\,. \tag{2.4}$$

Here *n, m* and *q* are integers. Therefore, all armchair carbon nanotubes are metallic tubes. One third of the tubes are metallic and the remaining two thirds are semiconducting tubes. Current technologies do provide for separation between metallic and semiconducting tubes yet, do not provide for full control of their chirality [12, 49].

There are two types of carbon nanotubes: single-walled carbon nanotubes (SWCNT) and multi-walled carbon nanotubes (MWCNT). SWCNTs are made of a tube with a single wall. MWCNTs are composed of several concentric cylindrical layers. Each layer may be either metallic or semiconducting depending on its chirality. This makes difficult to use MWCNT for electronic applications. Large current through the MWCNT usually eliminates the metallic carbon nanotube layer leaving the semiconducting layer intact [50-52].

2.1.3 Electronic Properties of Carbon Nanotube

The electronic energy dispersion relations for 2D graphite as a function of wave vector in Brillouin zone is shown in Figure 2.9 and calculated by solving the eigenvalue problem [33], $\det(H - ES) = 0$, for a (2×2) Hamiltonian H and a (2×2) overlap integral matrix S,

$$H = \begin{pmatrix} \varepsilon_{2p} & -\gamma_0 f(k) \\ -\gamma_0 f(k)^* & \varepsilon_{2p} \end{pmatrix} \quad \text{and} \quad S = \begin{pmatrix} 1 & sf(k) \\ sf(k) & 1 \end{pmatrix}, \tag{2.5}$$

$$f(k) = e^{ik_x a/\sqrt{3}} + 2e^{-ik_x a/2\sqrt{3}} \cos\frac{k_y a}{2}. \tag{2.6}$$

Here k_x and k_y are the wave vectors in the x and y directions, γ_0 is the nearest neighbor overlap integral, $a = \sqrt{3}d_{cc}$, ε_{2p} is the site energy of the 2p orbital [53].

$$E_{g2D}^{\pm}(\vec{k}) = \frac{\varepsilon_{2p} \pm \gamma_0 w(\vec{k})}{1 \mp s w(\vec{k})}, \tag{2.7}$$

$$\text{where} \quad w(\vec{k}) = \sqrt{\left|f(\vec{k})\right|^2} = \sqrt{1 + 4\cos\frac{\sqrt{3}k_x a}{2}\cos\frac{k_y a}{2} + 4\cos^2\frac{k_y a}{2}} \tag{2.8}$$

By linear k approximation for $w(\vec{k})$ from near the K point at the hexagonal Brillouin zone of graphite

$$w(\vec{k}) = \frac{\sqrt{3}}{2}ka + \cdots, \quad \text{for} \quad ka << 1 \tag{2.9}$$

The expansion of Equation 2.7 for small k values,

$$E_{g2D}^{\pm}(\vec{k}) = \varepsilon_{2p} \pm (\gamma_0 - s\varepsilon_{2p}) w(\vec{k}) + \cdots, \tag{2.10}$$

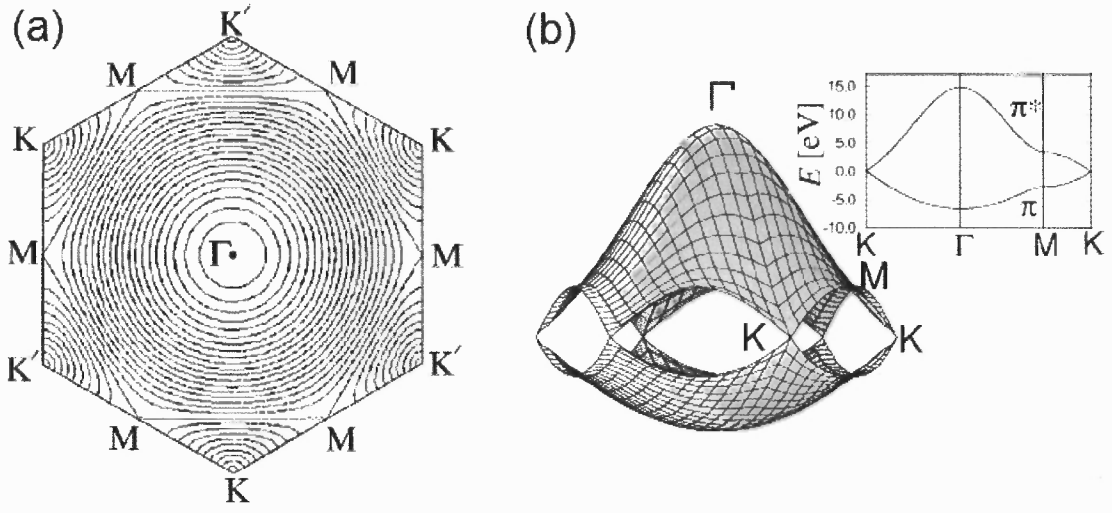

Figure 2.9 (a) The equivalent energy contour plot of 2D energy of graphite. (b) The energy dispersion relations in 2D graphite [53].

The 1D electron density of states of carbon nanotubes is given by zone folding of the 2D energy dispersion relation of a graphene layer [54] and assuming a linear k approximation for w(k), $\varepsilon_{2p}=0$ and s=0 for the Equation (2.7)

$$E(k) = \pm\frac{\sqrt{3}}{2}\gamma_0 ka = \pm\frac{3}{2}\gamma_0 k d_{cc} \tag{2.11}$$

The peak positions depending on the diameter of carbon nanotubes can be induced by the linear dispersion approximation of Equation 2.11 [54, 55]. The energy difference $\varepsilon_{ii}(D)$ for metallic and semiconducting carbon nanotubes are given by

$$\varepsilon_{11}^{M}(D) = \frac{6\gamma_0 d_{cc}}{D} \tag{2.12}$$

$$\varepsilon_{11}^{S}(D) = \frac{2\gamma_0 d_{cc}}{D} \tag{2.13}$$

where d_{cc} is the nearest cabon-carbon distance, D is the diameter of carbon nanotube, γ_0 is the carbon-carbon tight binding overlap energy integral [49]. The band diagram of carbon nantubes is comprised of discrete energy levels. The density of states, plotted as a function of energy (the Fermi level is located at zero) contains peaks known as van Hove singularities (VHS) as shown in Figure 2.10. The left hand side of Fermi level defines the valence band. The right hand side of Fermi level defines the conduction band. The energy band gap of semiconducting carbon nanotubes (zero density of state at the Fermi level) is proportional to $1/D$. The energy between the lowest resonance energy in the conduction band and the highest resonance energy in the valence band is larger for metallic carbon nanotubes and smaller for semiconducting carbon nanotubes. Figure 2.11 shows the energy band gap for single-walled carbon nanotubes as a function of tubes diameter. The energy difference between i^{th} VHS peaks $\varepsilon_{ii}(D)$ in the conduction band and valence band decreases with increasing diameter of carbon nanotubes. This result is from the tight-binding

band-structure calculations and the one-dimensional quantum confinement of the electrons in the nanotube [56].

Similarly to quantum wires, the conductance of a carbon nanotube may be written as

$$G = G_o M = (2e^2 / h)M . \tag{2.14}$$

Here $G_o = (2e^2 / h) = (12.9k\Omega)^{-1}$ is the quantized conductance and M is the number of conductive channels. However, there are many factors which affect the value of M: intertube coupling, electron-electron coupling, defects, impurities, distortion of structure, contacts on carbon nanotubes and substrate effects. Therefore, the experimentally measured conductance value of SWCNT is typically smaller than the theoretically predicated value. For example, the calculated resistance value for a single-walled carbon nanotube is 6.45 kΩ and the experimentally measured resistance is approximately 10 kΩ [4, 57-60].

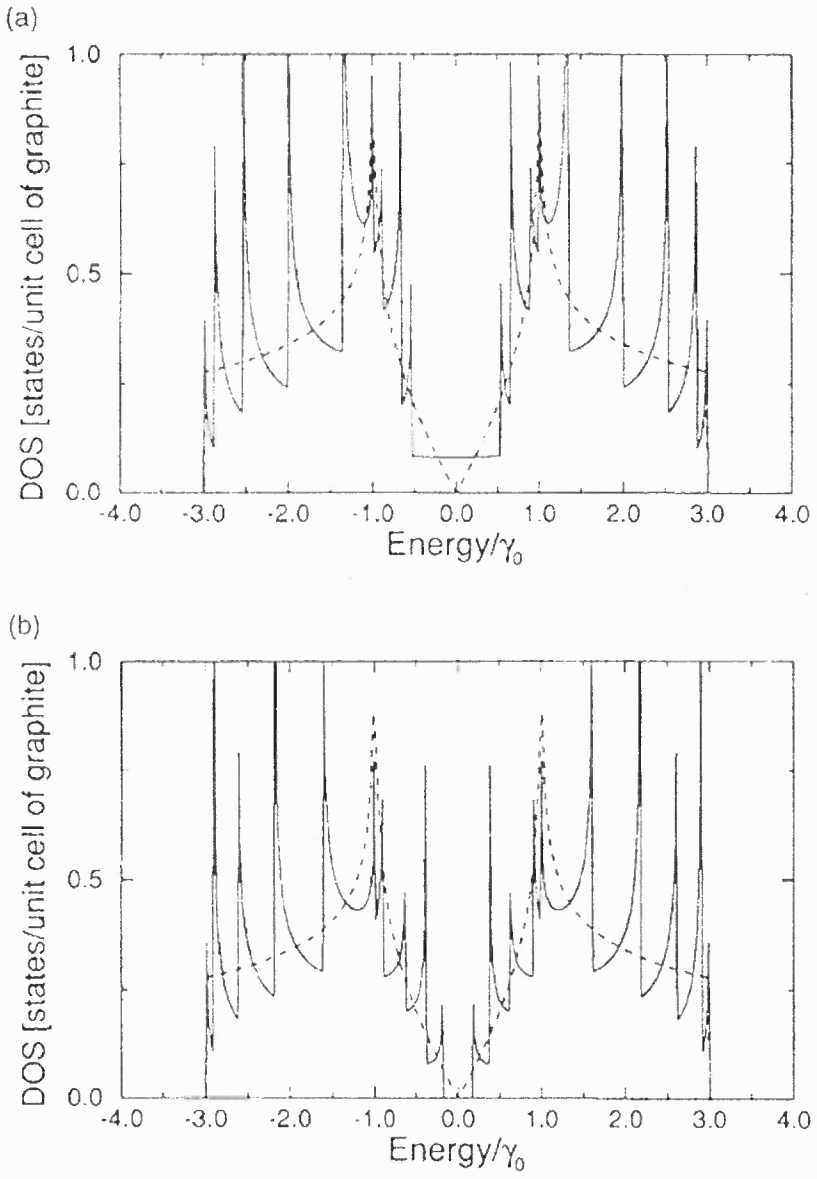

Figure 2.10 Electronic density of states (DOS) of (a) metallic and (b) semiconducting carbon nanotubes [61].

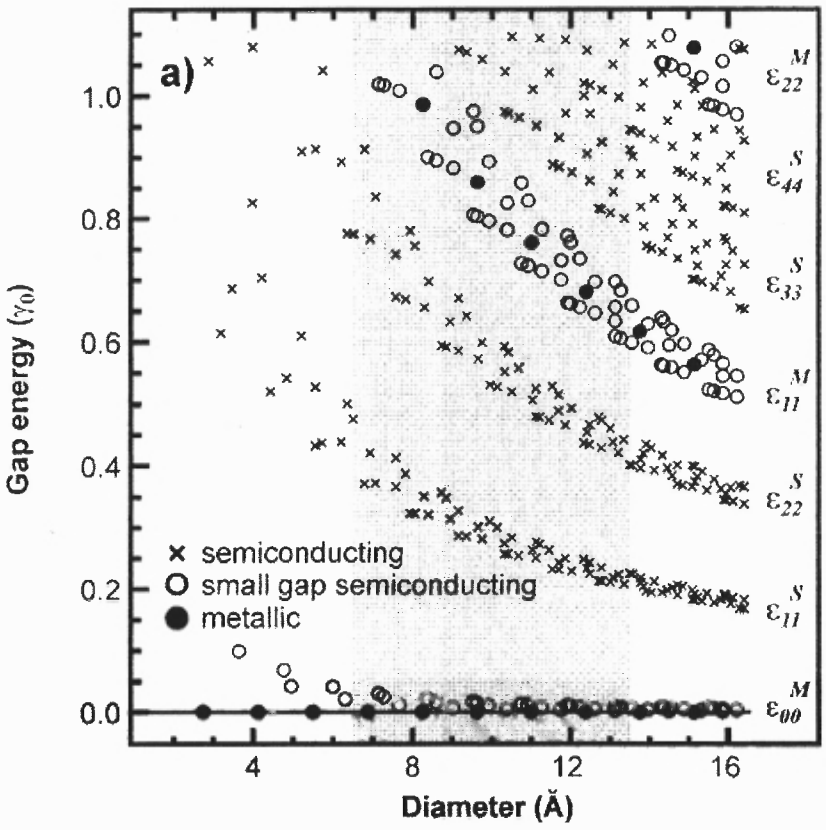

Figure 2.11 Energy band gap (ε_{ii}) for single-walled carbon nanotubes as a function of tubes diameter. The index *i* denotes the transition between van Hove singularities of the same index number. Small index *i* defines a closer position to the Fermi level [62].

2.1.4 Raman Scattering from Carbon Nanotube

Raman spectroscopy is a useful technique to study the structure, electronic and phonon properties of carbon nanotubes.

A carbon nanotube has N hexagons Each carbon nanotube has 6N phonon modes - 4 acoustic modes, including the rotation around the nanotube axis (R_z) at the Γ point, and 6N-4 optical modes. The number of Raman active modes may be calculated by group theory using the specified lattice structure and symmetry. The total number of phonon modes varies as a function of tube chirality. Group theory selection rules have predicted that there are between 15 or 16 Raman active modes for typical carbon nanotube [33].

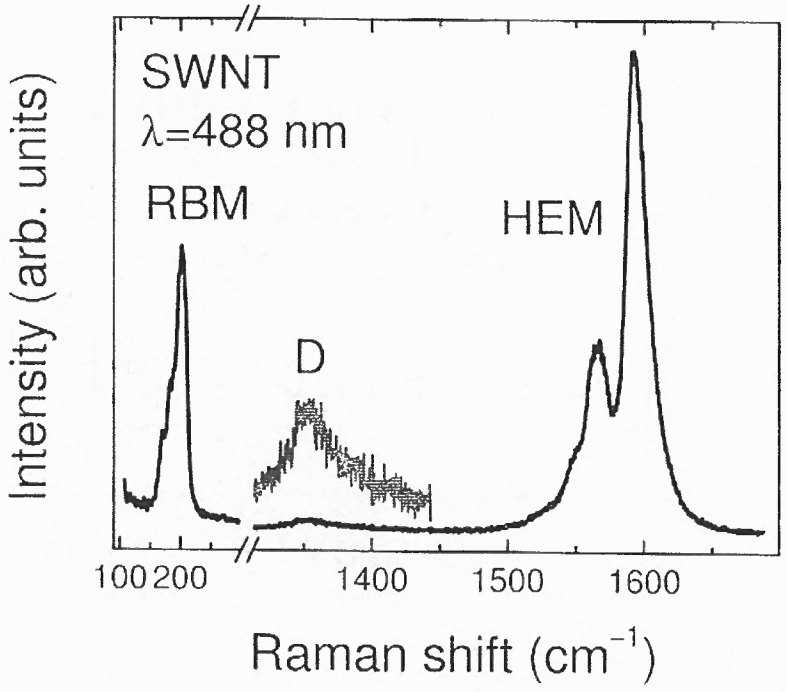

Figure 2.12 Typical Raman spectra of single-walled carbon nanotubes. RBM: Radial Breathing Mode. D: Defect mode. HEM: High Energy Mode – Tangential vibration [63].

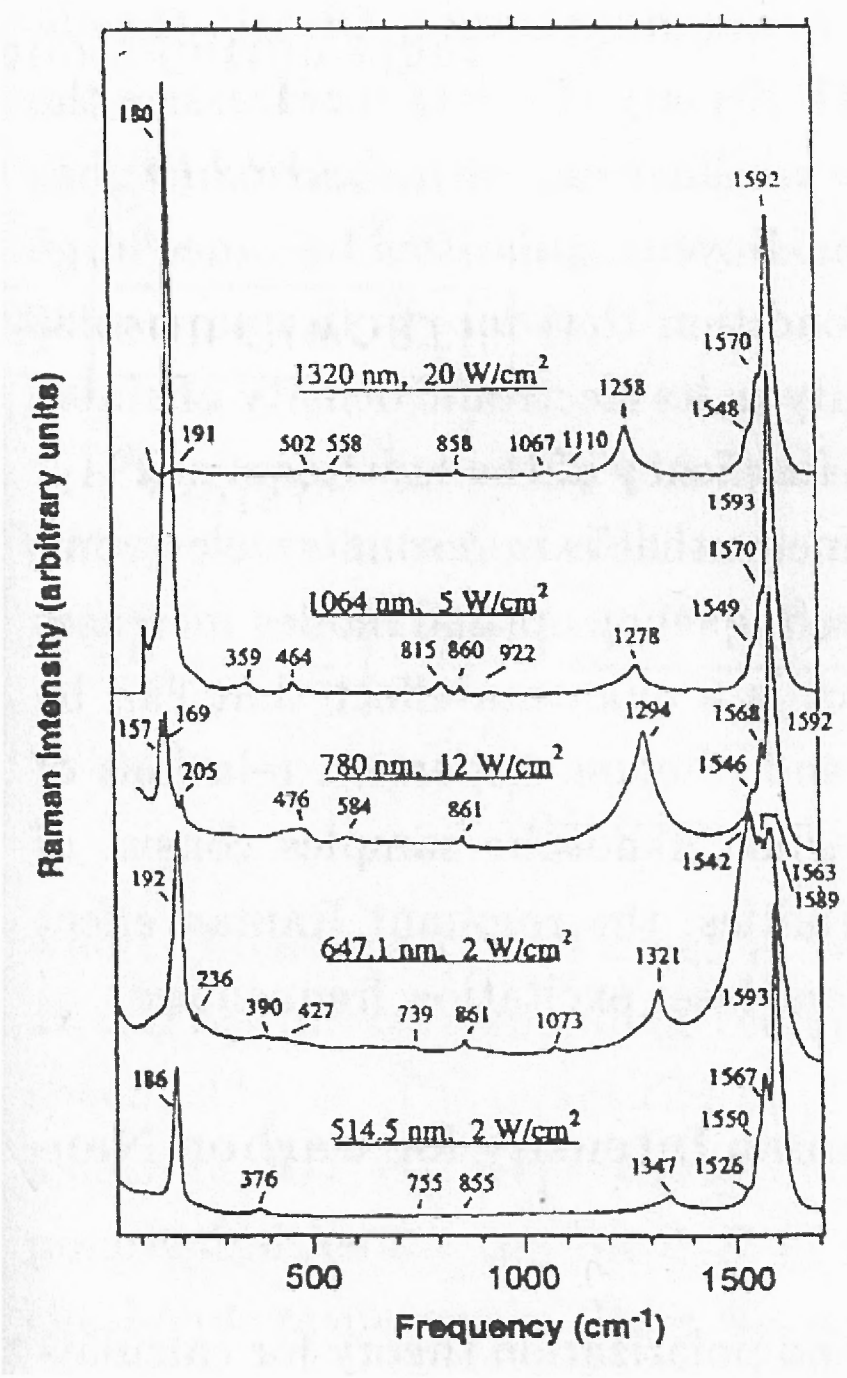

Figure 2.13 Raman spectra of purified single-walled carbon nanotubes using five different laser frequencies. The high frequency mode at 1600 cm^{-1} shifts upward as the laser frequency is increased. This is attributed to resonance enhancement, which is related to the van Hove singularities [33, 64].

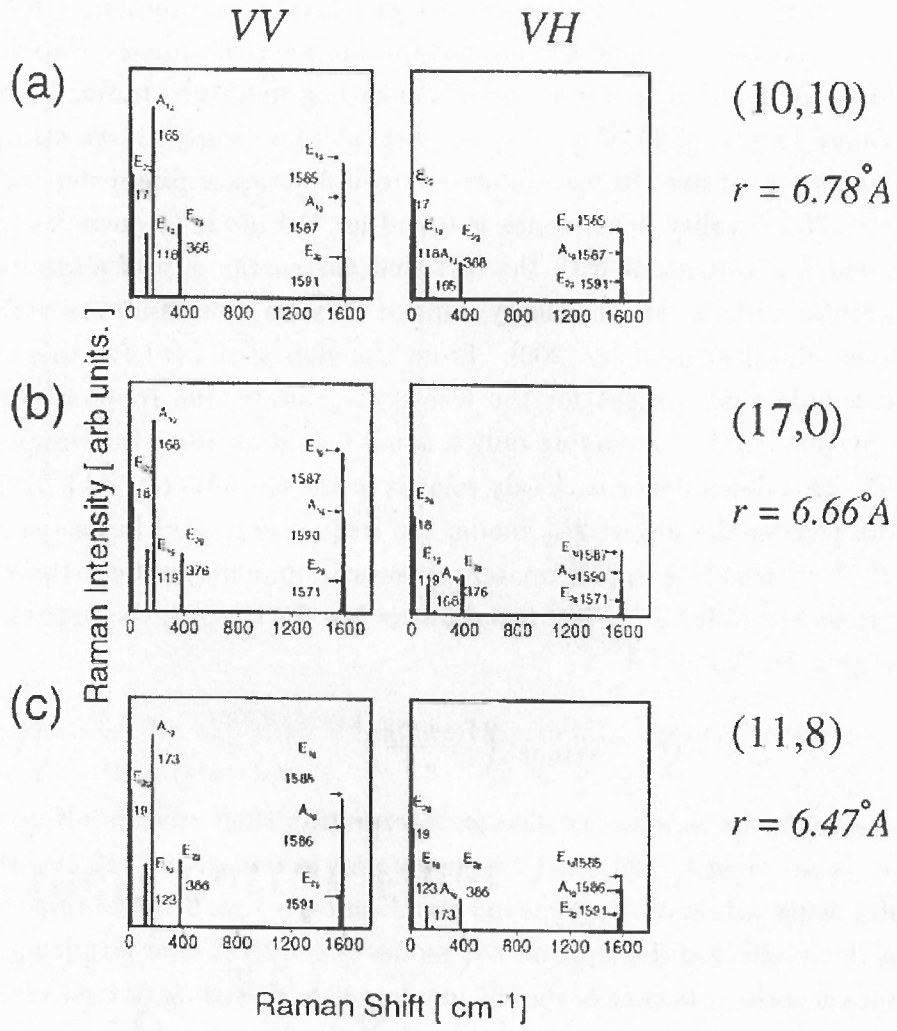

Figure 2.14 Polarization dependence of Raman spectra of single-walled carbon nanotubes. The chiral vector and the diameter of the carbon nanotubes are provided on the right. The VV (the incident and the scattered polarization states are parallel) configuration is shown on the left column. The VH (the incident and the scattered polarization states are perpendicular to each other) configuration is shown on the right column [33].

Raman scattering of carbon nanotubes is typically divided into the three main regions. Radial breathing modes (RBM) are located at the low-frequency range between 100 and 400 cm^{-1}. A defect induced mode (D-mode) lies between 1200 and 1400 cm^{-1}. The high energy mode (HEM) is in the range of 1500-1600 cm^{-1}. Typical Raman spectra are shown in Figure 2.12.

The Raman peaks depend on the laser frequency used. Intensity of the peaks is enhanced by electron-phonon coupling when the excitation energy is close to a resonance (transition between two van-Hove singularities) as shown in Figure 2.13.

Figure 2.14 shows the polarization dependence of the Raman intensity. The VV polarization means that the linear polarization states for the incident and the scattered optical beams are parallel to one another. The VH polarization means that the linear polarization states for the incident and the scattered light are perpendicular to each other. The intensity of Raman scattering is normalized to the maximum intensity value. At low frequencies, the intensity of the E_{1g} and E_{2g} modes is similar for the VV and VH configurations. The intensity of the A_{1g} mode, the most dominant mode among low frequency spectra, is greatly reduced for the VH scheme [33].

Low-frequency Raman modes depend on the diameter of the carbon nanotubes. Figure 2.15 shows a log plot for the calculated Raman-active modes as a function of the tube's diameter. Therefore, the diameter of carbon nanotubes may be assessed by the peaks of its RBM modes. Larger force is required to deform small diameter tubes [63]. Therefore, the smaller the diameter is, the larger is its corresponding RBM frequency. The relationship between the diameter of a carbon nantube and its RBM peak frequency is given by

$$\omega_{RBM} = \frac{228}{d_t} + 16cm^{-1}, \tag{2.9}$$

where d_t is the diameter of the tube [61].

The mid frequency range is characterized by the D modes signifying structural defects. The ratio between the G mode (high frequency peak: 1500-1600 cm^{-1}) and the D mode (G/D) is used to assess the quality of carbon nanotubes grown. Sometimes referred to

as the disordered mode, the D mode is located in the range between 1330 and 1360 cm^{-1}. Large intensity of the D mode is usually observed in multi-walled carbon nanotubes. Defect free carbon nanotubes are expected to portray small D mode peak.

The high-frequency mode - the G mode or Tangential Mode, corresponds to the stretching mode in the graphite plane. This mode is located around 1580 cm^{-1}. The peak position of that mode is relatively insensitive to the tube diameter. Figure 2.16 shows the calculated Raman frequency for the (10, 10) carbon nanotubes. The Raman modes in Figure 2.16 do not have strong dependence of the tube's chirality either.

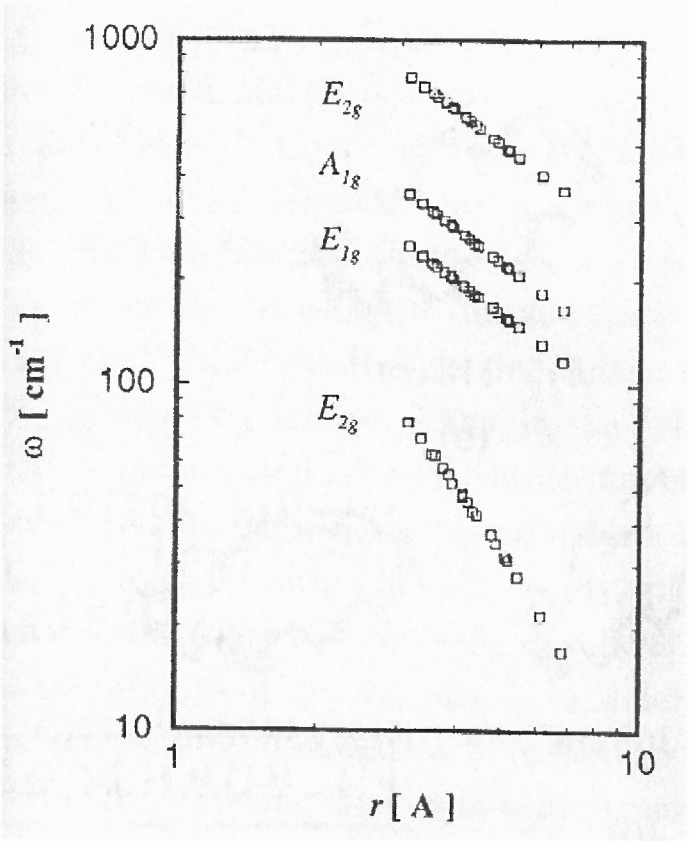

Figure 2.15 Low-frequency Raman lines as a function of the radius of carbon nanotubes [33].

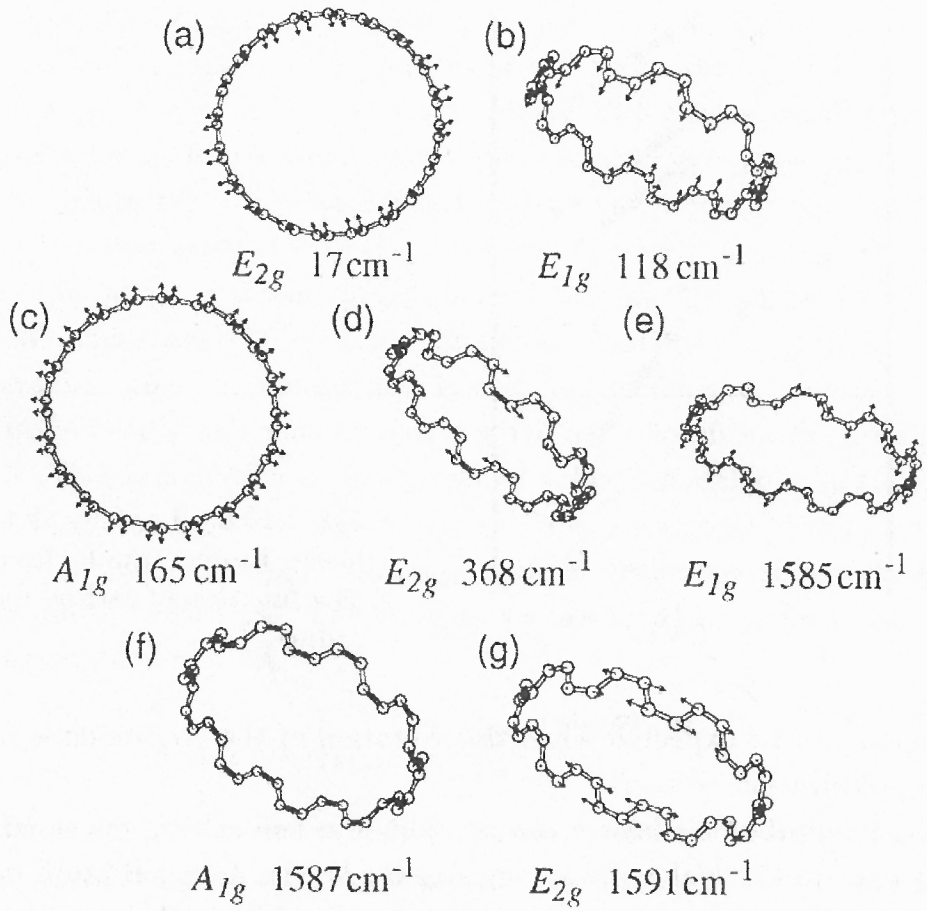

Figure 2.16 Raman modes, atomic displacement and frequencies. These were calculated for (10, 10) nanotubes. The modes shown above are independent of the chirality of the nanotube [33].

2.2 Conductive Polymer

Polymers are long chains of monomers, which are composed of repeated molecular units and connected by covalent bonds. In general, polymers are good insulators: for example, polyethylene is used for packaging of electronic devices due to its environmental stability. In the late 1970s, Alan J. Heeger, Alan G. MacDiarmid and Hideki Shirakawa discovered polyacetylene, a conductive polymer, which becomes conductive upon oxidation with iodine. The iodine removes an electron from the π bonds and makes the remaining electrons movable throughout the chain [65]. The discovery of conductive polymer enabled new applications for otherwise insulating polymers. Polypyrrole, polythiophene, polyaniline, poly(p-phenylenevinylene), polycarbazole and their derivatives are but a few examples of commonly used conductive polymers. Unlike metals, conductive polymers are light weight and flexible. Their characteristics may be chemically tuned by doping. Nowadays, conductive polymers have been used as light emitting diodes (LED), transistors, solar cells, flexible electronics and as part of flat panel displays [5, 16, 18, 40].

2.2.1 Polymerization

Conductive polymer can be doped by an oxidation and reduction (REDOX) process. There are two primary methods of doping a conductive polymer. One is using chemical doping, which is to expose the polymer to an oxidant, typically iodine or bromine. The other employs electrochemical doping in the form of electron addition (n doping) or removal (p doping) when applying external electrical bias. Negatively doped polymers are rare because the oxygen rich atmosphere is an oxidizing agent. An electron rich n doped polymer will immediately react with elemental oxygen to de-dope (re-oxidize to the

neutral state) the polymer. Thus, chemical n doping has to be made in an inert environment, such as argon atmosphere. Electrochemical n doping is far more common in research because it is easier to exclude oxygen from a solvent in a sealed flask. However there are likely no commercialized n doped conductive polymers [16, 66]. Film thickness may be controlled by adjusting the polymerization conditions such as scan rate, biasing potential and time. Various electrodes may be used for the deposition of a polymer film as long as they are conductive. For example, in this study, polypyrrole and polycarbazole were deposited on the surface of carbon nanotube intra-connects.

2.2.2 Polypyrrole

Polypyrrole is one of the most extensively studied conjugated polymers: it is chemically stable, highly conductive and easily processable. Its good stability under electrochemical conditions made it attractive as an organic material for electronic application. Polypyrrole (PPy) has ring structures of series of pyrrole monomers that exhibit high electrical conductivity when doped. The polymer is made by electrolytic polymerization of a pyrrole monomer (Figure 2.17). Polypyrrole is one of the derivatives of polyacetylene: its conductivity is similar to iodine doped polyacetylene. Typical conductivity of polypyrrole is 10^2~10^3 (S/cm). Details of the polymerization process are shown in Figure 2.18. A radical cation is created by oxidation of the monomer. The positive charges become the carriers through the polymer backbone by deprotonization to form dimer. Polymer chains become longer as the procedure repeats itself [67].

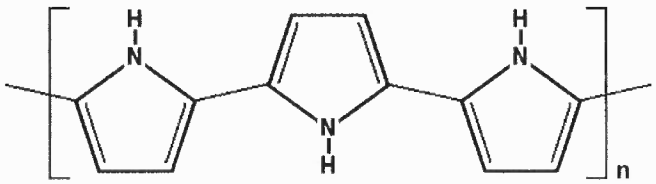

Figure 2.17 Polypyrrole (PPy) [67].

Figure 2.19 shows the Raman spectra of PPy film by Furukawa et al. [68]. The peak at 1595 cm^{-1} is associated with an overlap of two oxidized structures, C=C stretching modes. Peaks at 968 cm^{-1} and 1055 cm^{-1} are considered to be polarons. Bipolaron is located at 934 and 1086 cm^{-1} [68].

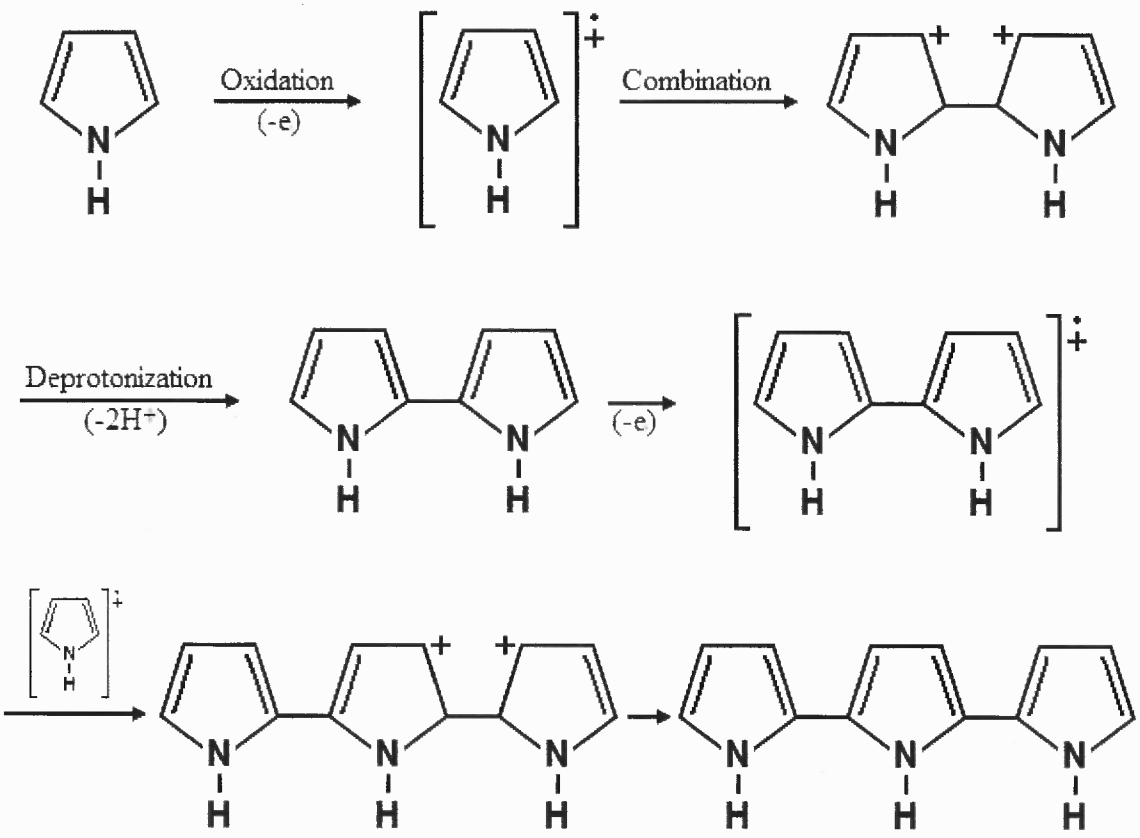

Figure 2.18 Polymerization process of pyrrole [67].

The conductivity of polypyrrole decreases as the temperature decreases. In contrast, the conductivity of metals will increase when the temperature decreases. The conductivity of polypyrrole depends on environmental conditions, such as temperature, electrolyte concentration, doping concentration. Polypyrrole prepared at low temperature will maintain larger conductivity, longer chains and a smaller number of defects [68].

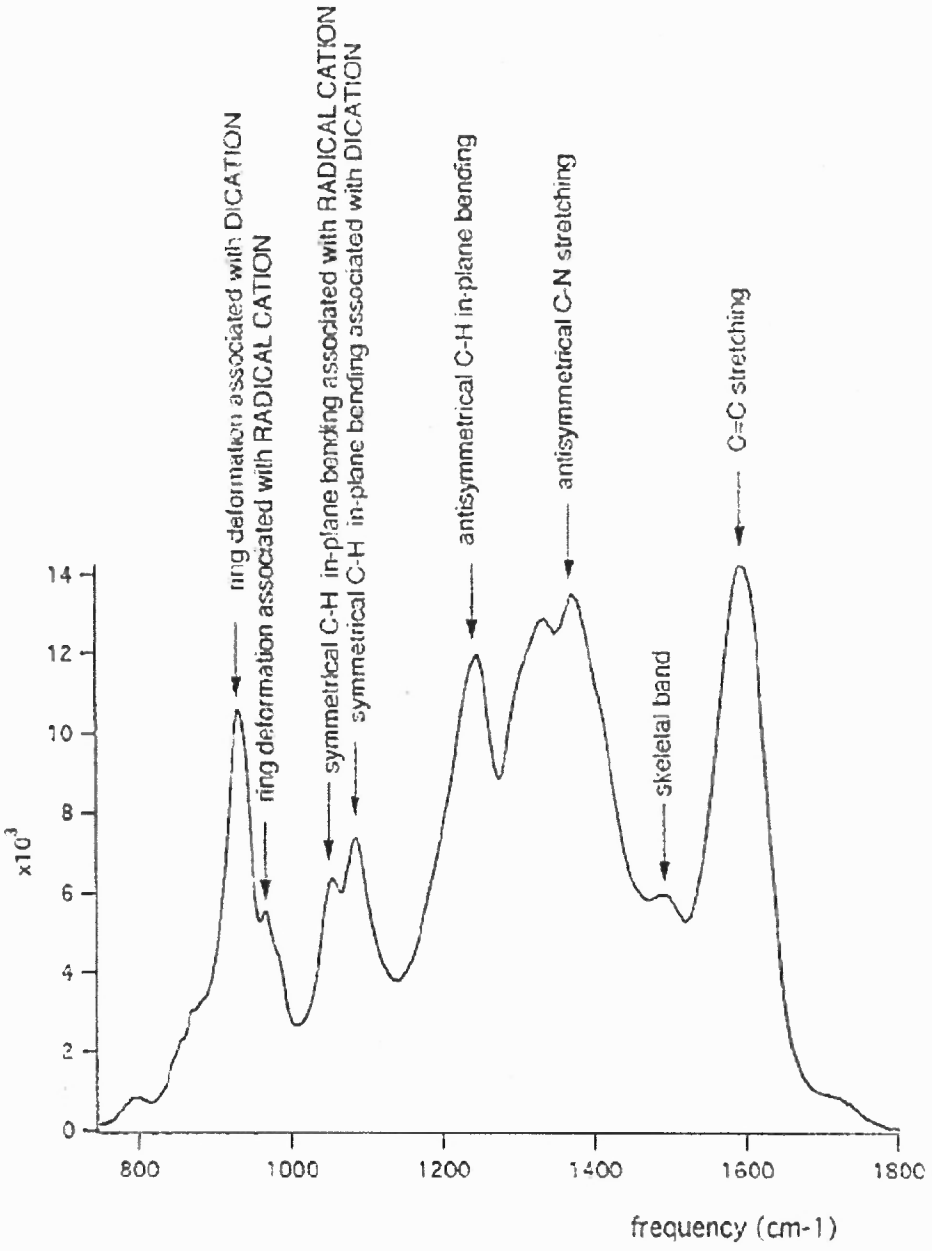

Figure 2.19 Raman spectra of PPy film and bands assignment. (Furukawa et al. [68]).

Polypyrrole (PPy) has low oxidation potential. The conductivity of PPy increases initially as the solvent dries out. After a prolong time, the conductivity decreases due to oxidation in air. The presence of moisture will accelerate the conductivity decrease of PPy [68].

2.2.3 Polycarbazole

Polycarbazole has been synthesized only recently. Polycarbazole [69] may be synthesized electrochemically by electropolymerization of carbazole in acetonitrile under anodic potential. Anodic peak potential is observed at 1.4 V under cyclic voltammetry. The electrolyte was consisted of 0.02M carbazole monomer and 0.2M TBABF4 (tetrabutylammonium tetrafluoroborate) in acetonitrile. The surface of the working electrode was covered with dark green polycarbazole film while potential was applied to the working electrode. The electrolyte also turned green due to formation of dimers and trimers . Higher concentration of monomer helps the radical cation formation and increases the rate of polymerization [69, 70].

Figure 2.20 shows the electrochemical polymerization of carbazole. First, carbazole monomer is oxidized at the anode. Dimer is formed by combining two oxidized monomers. Repeated procedure makes longer conductive polycarbazole chains. The conductivity of polycarbazole (PCz) film is approximately 10^3 S/cm. Conductivity of PCz was recorded for 150 days in air (Figure 2.21). The conductivity decreases substantially during the first 20 days after which the decrease rate is smaller. The conductivity approaches half of its original value after 5 months. Raman spectra of polycarbazole film (Figure 2.22) are due mostly to C-H, C-N and C=C bonds.

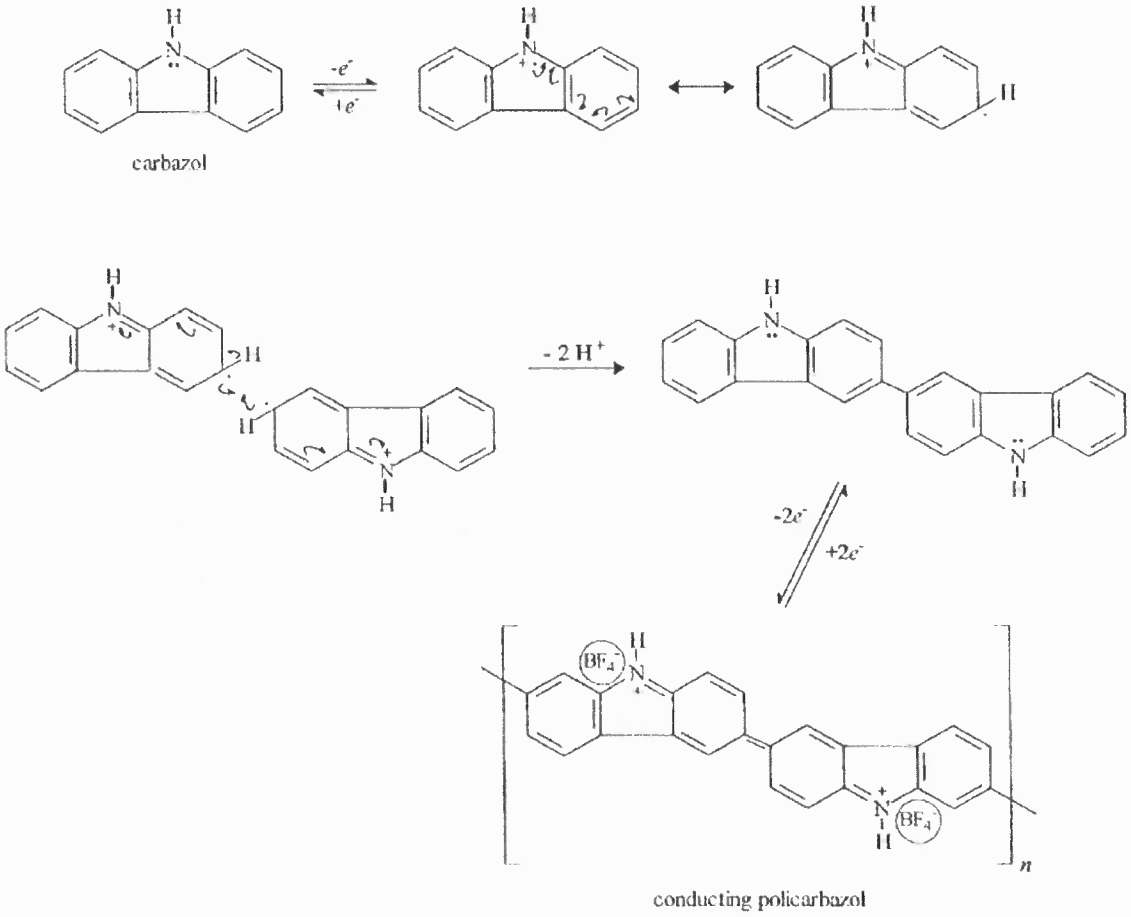

Figure 2.20 Schematic of electropolymerization of polycarbazole [69].

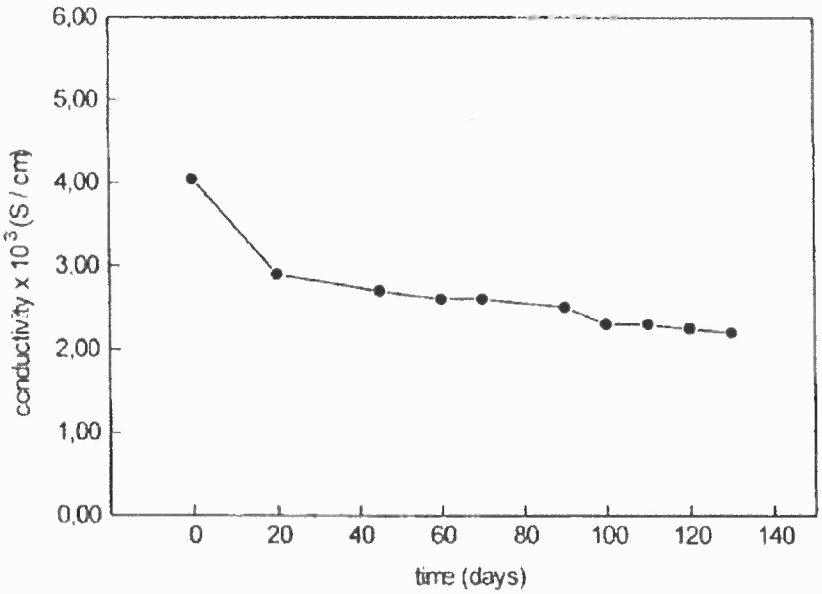

Figure 2.21 Time dependent conductivity of polycarbazole [69].

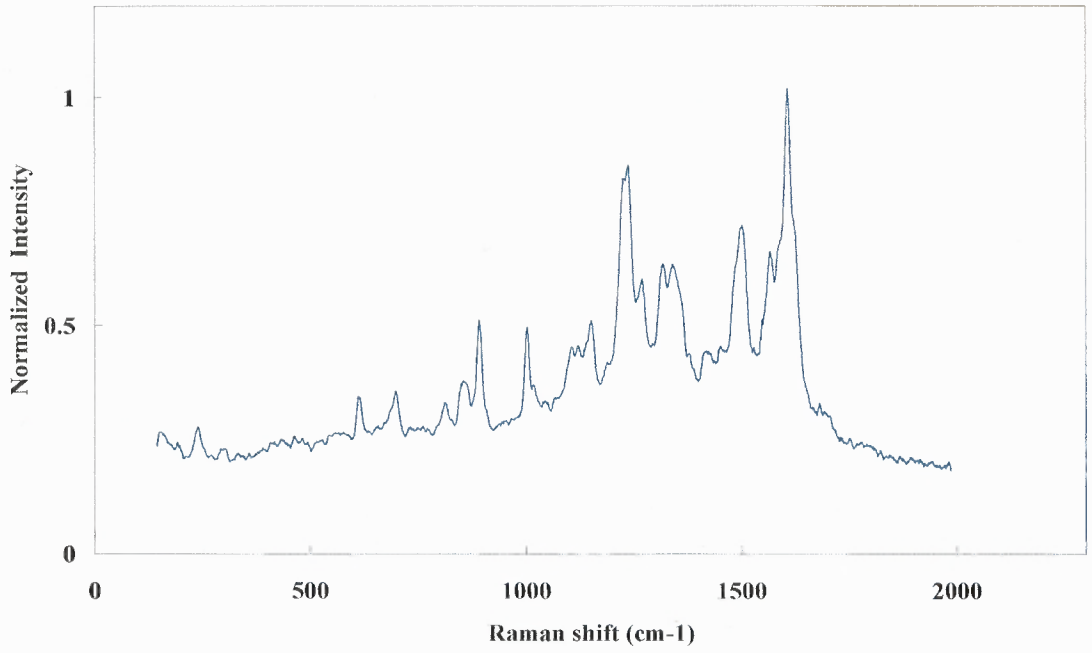

Figure 2.22 Raman spectra of polycarbazole thin film on conductive glass.

2.3 Negative Differential Resistance

When voltage is applied to an electrical element, such as, a resistor, the current-voltage relationship is typically linear. Other elements, such as transistors, exhibit current-voltage saturation. In all of these examples, differential positive current changes follow differential positive voltage changes. However, when the current decreases upon an increase of the voltage, this region is known as negative differential resistance. It may exhibit S-shaped, or N-shaped current-voltage characteristics.

2.3.1 N-shaped Negative Differential Resistance – Esaki Diode

Figure 2.23 shows temperature dependence I-V characteristics for the Esaki diode made of SWCNT p+n+ junction. The Fermi level on the n side shifts down under reverse biasing.

The electrons on the p side tunnel through the junction with increasing reverse bias voltage (Figure 2.23(b)). For small forward bias voltage, electrons flow from the n to the p side (Figure 2.23 (c)). In this region, the current is dominated by tunneling. However, current decreases as we increase the forward bias further since the available states on the p side are reduced as the energy bands pass by each other (Figure 2.23 (d)). Here, the current is dominated by thermal diffusion for larger forward bias values beyond the negative resistance region. Thermal diffusion current will be reduced at low temperature, while the tunneling current will be affected by varying the temperature. Therefore, negative differential resistance becomes clearer at low temperatures [4, 71].

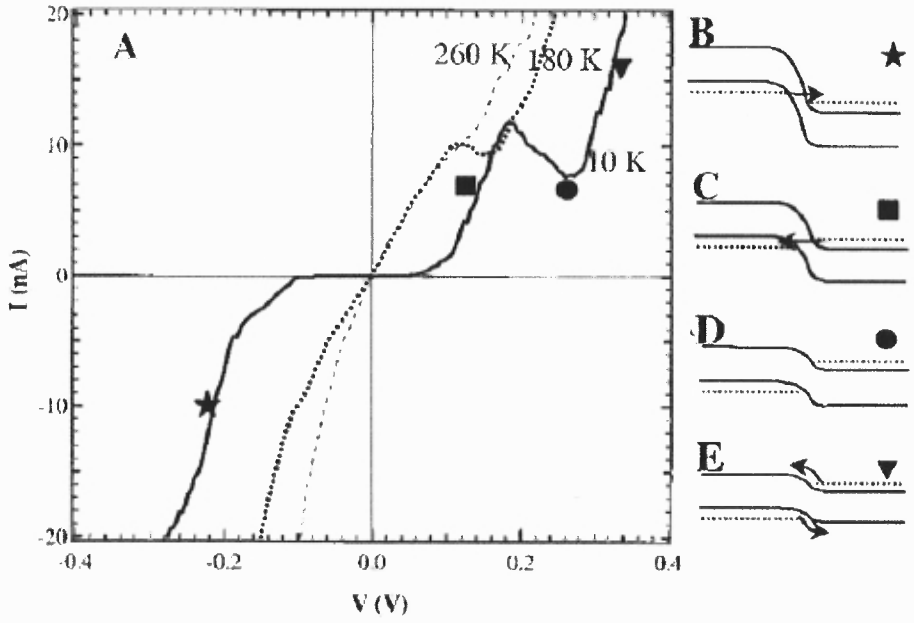

Figure 2.23 Negative differential resistance from CNT Esaki Diode [71].

2.3.2 N-shaped Negative Differential Resistance – CNT FET

Three-terminal devices are utilized in practical applications (Figure 2.24) [72, 73] taking advantage of two metal work functions. Figure 2.25(a) shows a typical geometry of CNT based, field-effect transistor (FET) with un-doped carbon nanotube channel. The channel consists of a semiconducting SWCNT. CNT based FET exhibits ballistic transport if the CNT channel is defect free. The current saturates when a high gate bias voltage is applied. In the case shown in Figure 2.24, the metal work functions are 4.33 eV for Titanium and 5 eV for Cobalt, respectively. As shown in Figure 2.25, the band gap of a semiconducting SWCNT will vary if a gate bias is applied.

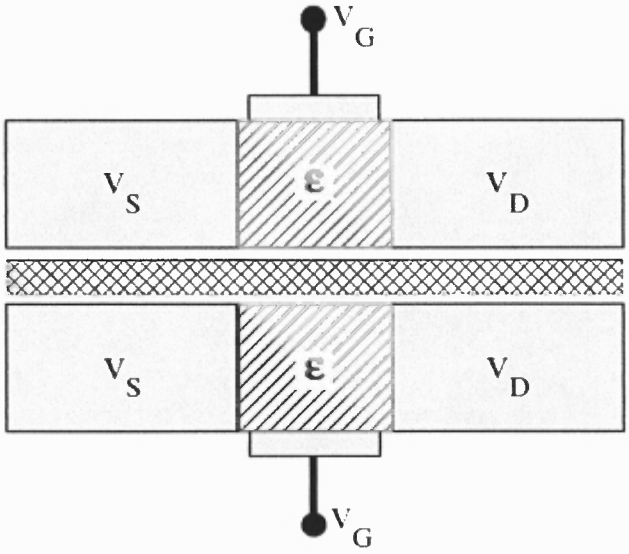

Figure 2.24 Schematic of a nanotube device which exhibits negative differential resistance. The gray regions are metal contacts to carbon nanotube. The cross-hatched line represents the carbon nanotube channel across the metal contact. The gap between the electrodes has a dielectric constant of ε [74].

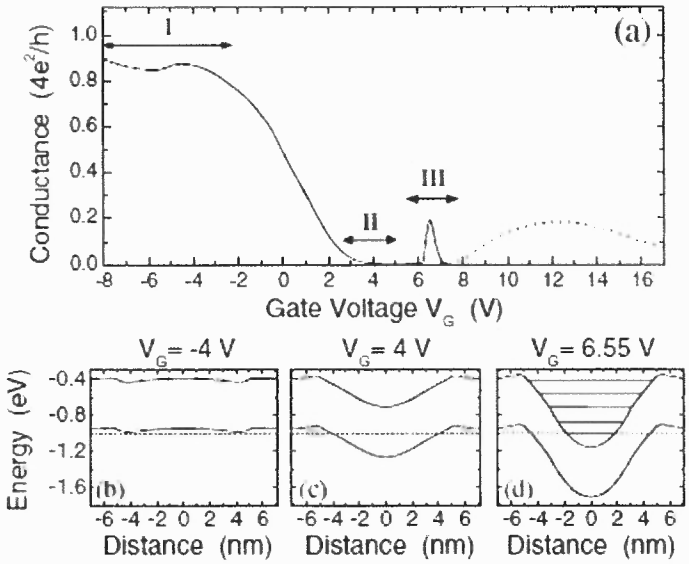

Figure 2.25 (a) Conductance vs. gate voltage. (b)-(d) The valence band and conduction band for the indicated gate voltage. The dotted line is the Fermi level. The NT channel insulated by dielectric was 10 nm long (denoted as distance from -5 nm to +5 nm) [74]. CNT devices have been primarily studied using two-terminal devices [75, 76].

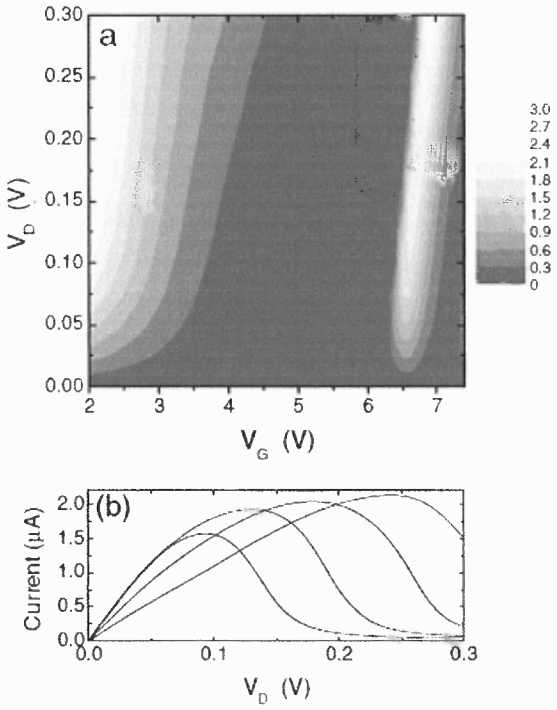

Figure 2.26 (a) Current as a function of drain and gate voltages. (b) The current vs. drain voltage for fixed gate voltages, V_g = 6.5, 6.6, 6.7 and 6.8 V. The peak shifts from left to right as the gate voltage increases [74].

Figure 2.25(a) presents the calculated conductance as a function of a gate voltage, V_g. The conductance is high at negative V_g while the conductance is nearly zero at positive V_g (Region I and II in Figure 2.25(a), respectively). The conductance increases and drops as a function of V_g in region III. Band diagram corresponding to negative gate voltage is shown in Figure 2.25(b). The high metal work function forces the Fermi level below the valence band of the CNT. The gate voltage is used to induce channel inversion. The conductance is high since holes can flow through the CNT channel without facing barriers. The energy bands are pulled down with positive gate voltage. An energy barrier is formed and turns off the current. In Figure 2.25(d), the conduction band is pulled down electrostatically with increasing V_g, thus resulting in the formation of quantum confinement with localized states. Electrons can tunnel through the quantum dot when the lowest energy level of the quantum dot drops below the valence band. Tunneling through nanoscale quantum dot may result in a negative differential resistance at room temperature. This makes CNT based FET a gated resonant-tunneling device.

Figure 2.26 shows the current as a function of both drain and gate voltages. The current can be calculated by the Landauer formula,

$$I(V) = \frac{4e}{h}\int [F(E) - F(E + eV_D)]P(E)dE\,. \qquad (2.10)$$

Here V_D is the drain voltage with the source taken as ground. F is the Fermi function. The source-drain current exhibits an abrupt transition for gate voltages (V_g= 3~4 V) corresponding to region I and region II in Figure 2.25. Negative differential peak appears at high gate voltage. The current increases as the drain voltage increases. Then, the current decreases as there are no available states for tunneling (Figure 2.26(b)). The gate voltage controls the maximum current position by adjusting the energy of the resonant level.

2.3.3 S-shaped Negative Differential Resistance

The component having S-shaped negative differential resistance acts as a voltage un-stable dynamic resistor. Electrically conductive polymer often shows negative differential resistance, for example, polypyrrole [77]. Figure 2.27(a) and Figure 2.27(b) show the current-voltage characteristics of electrochemically grown polypyrrole film. It exhibits a typical S-shaped negative differential resistance. The current was swept up and down and the curves followed the same traces (Figure 2.27(a)). Figure 2.27(b) shows S-shaped negative differential resistance in current-voltage characteristics for various temperatures.

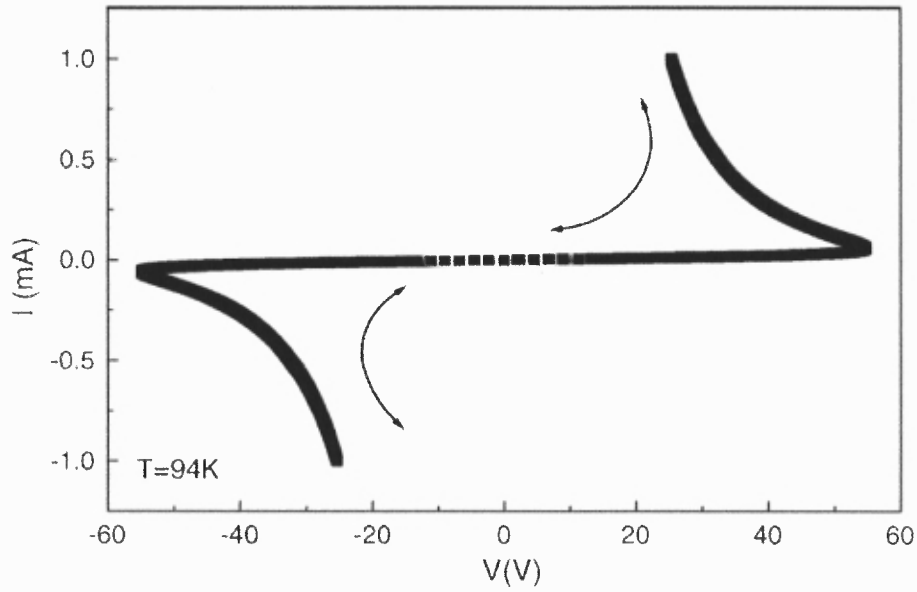

(a)

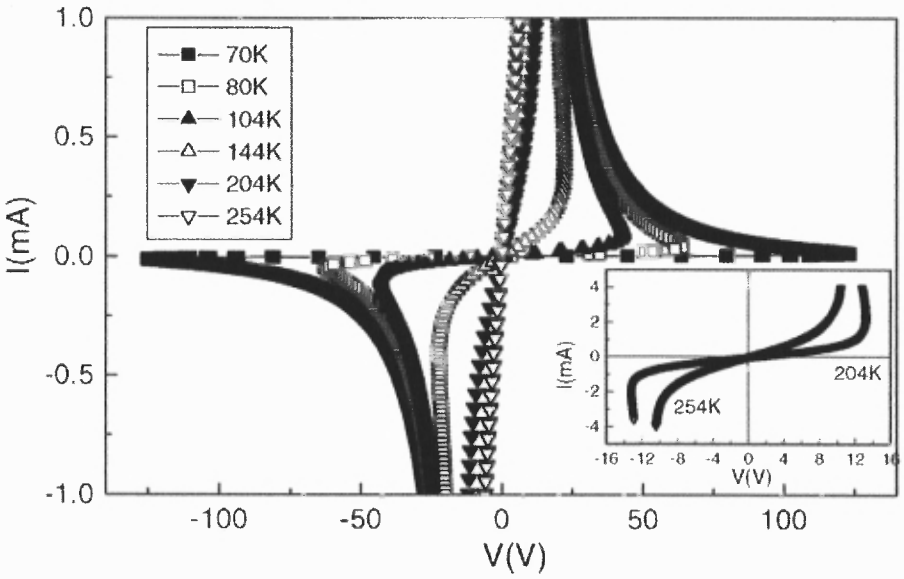

(b)

Figure 2.27 (a) Negative differential resistance (NDR) is exhibited by polypyrrole film at an applied electric field of 500 V/cm. Curves follows same traces for up-down current sweeping direction. (b) NDR measurements at various temperatures [77].

2.4 Schottky Barrier at CNT-metal junction

Carbon nanotube based field effect transistors typically have Schottky barriers (SB) at the CNT-metal interface. SB is one of a key factor which affects the device performance. In this study, metal electrodes are composed of Co layer on top of Ti layer. The work function is 5 eV for Co layer and 4.33 eV for Ti layer, respectively. The electron transport through the SB affects the tunneling current and the thermionic emission. Figure 2.28 is an example of electrical properties of CNT FET by varying metal work function. Reduced metal work function decreases p-channel conductance and increases n-channel conductance by lowering SB barrier height [78].

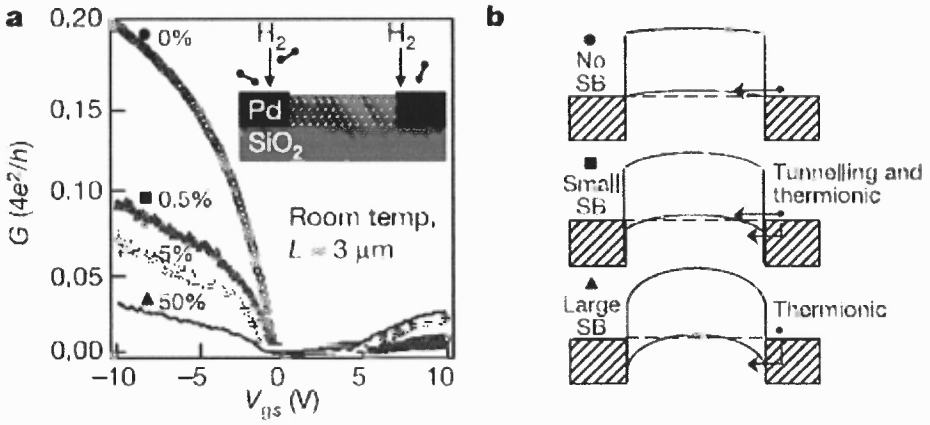

Figure 2.28 Electron transport properties of CNT FET by varying SB height. Metal work function is adjusted by exposure to hydrogen [78].

CHAPTER 3

EXPERIMENT

Carbon nanotube (CNT) intra-connects were grown by chemical vapor deposition (CVD) between a layout of metal electrodes. The CNT intra-connects were later electroplated with electrically conductive polymers (ECPs), such as polypyrrole (PPy) and polycarbazole (PCZ). I_{ds}-V_{ds} characteristics, I_{ds}-V_{gs} characteristics, and photo-conductance were assessed. Raman scattering was analyzed in order to determine the type of CNT grown.

3.1 Metal Electrode Design

Metal electrodes were fabricated by optical lithography (Figure. 3.1). A 30 nm thick of titanium (Ti) electrode was deposited on a Si substrate. The silicon substrate was oxidized prior to the deposition of the electrodes. The oxide layer was approximately 20 nm thick. A 30 nm thick layer of cobalt (Co) was deposited for multi-walled carbon nanotube growth and a 1 nm thick layer of cobalt (Co) was deposited for the growth of single-walled carbon nanotubes . The thin catalytic layer of Co breaks into tiny islands at high temperatures (700 – 900 ^{o}C) thus enabling the growth of the CNT at the electrode tips. The distance from tip to tip was approximately 1 μm.

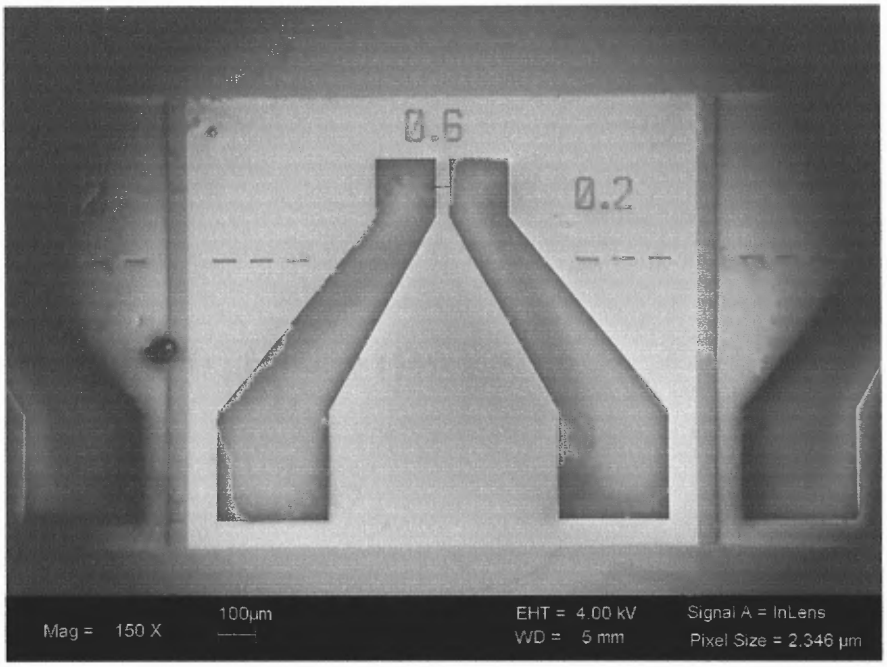

(a)

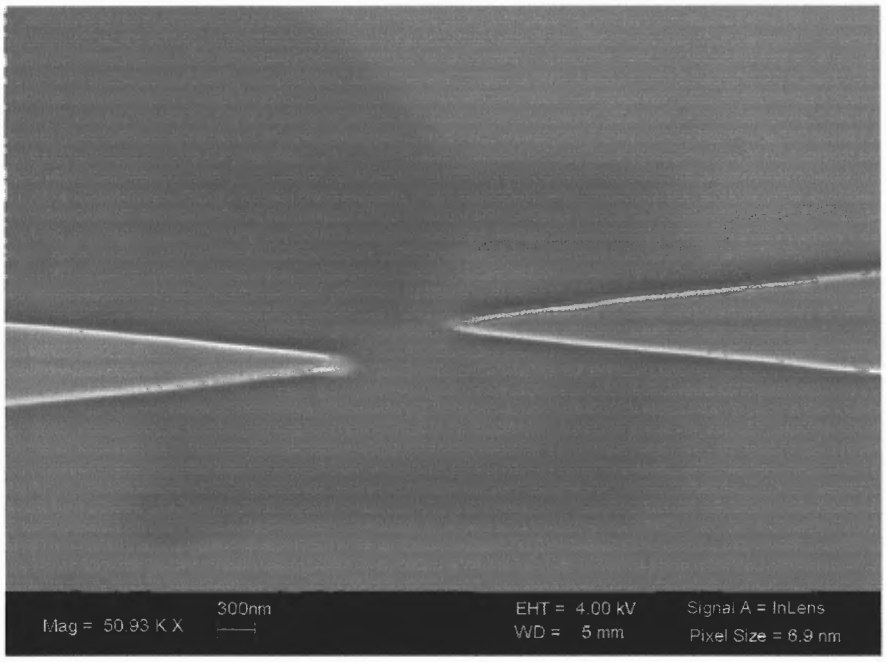

(b)

Figure 3.1 (a) SEM image of metal electrodes. (b) Magnified image of metal tips between two electrodes. The distance between the two tips is approximately 1 um.

3.2 Chemical Vapor Deposition (CVD)

Carbon nanotubes intra-connects have been grown by chemical vapor deposition (CVD) process. The growth of the CNT intra-connects were performed under various conditions. Various gases were used: carbon monoxide (CO), ethanol vapors, methane (CH_4) and hydrogen (H_2) mixture. Figure 3.2 shows the schematic of CVD setup. Temperature was used as a variable, from 600 ℃ to 900 ℃. Usually, multi-walled carbon nanotubes (MWCNT) were grown at relatively low temperatures. It is likely that single-walled carbon nanotubes were grown at higher temperature (approximately 900 °C). Temperature diagrams are most helpful as process trailers and are shown in Figure 3.3.

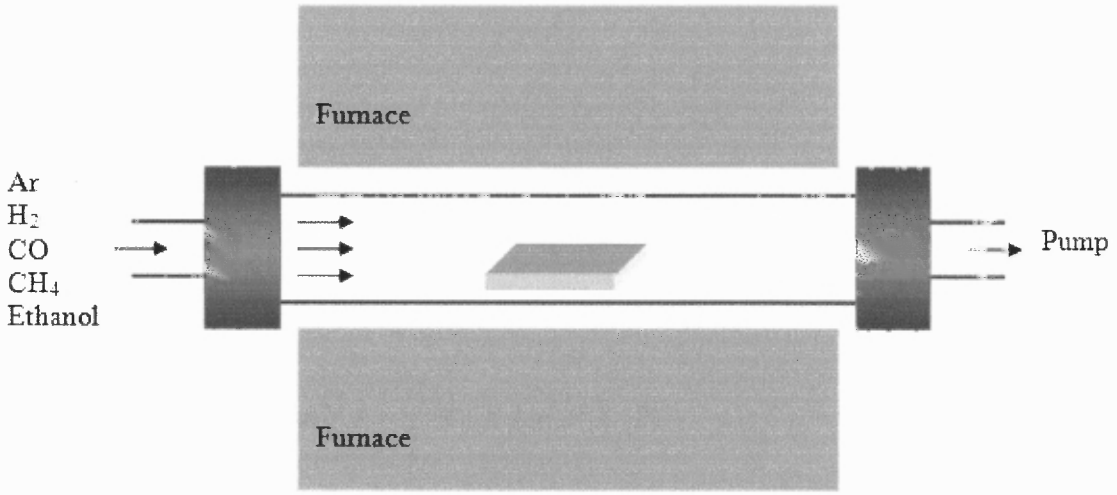

Figure 3.2 Chemical vapor deposition (CVD) setup.

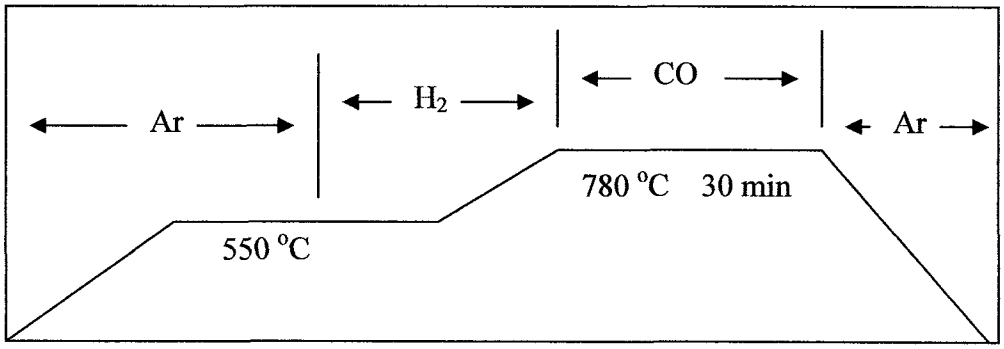

(a)

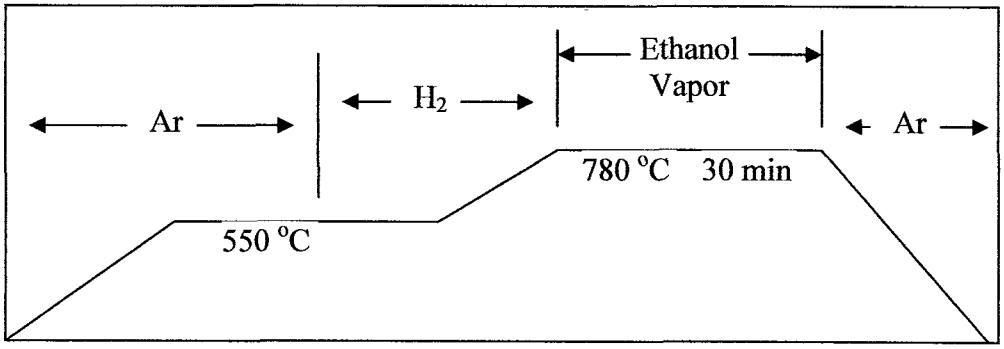

(b)

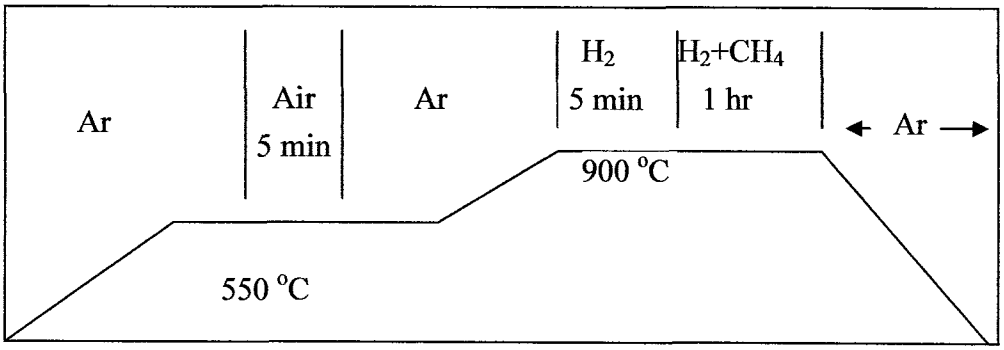

(c)

Figure 3.3 Temperature diagrams: (a) CO CVD. (b) Ethanol CVD (c) Methanol and hydrogen mixture.

In CO CVD (Figure 3.3(a)), samples were placed in the middle of a quartz tube and argon gas was introduced at a flow rate of 100 sccm. Temperature was increased to 550℃, the argon gas was pumped out and H_2 gas was introduced at a flow rate of 100 sccm. The H_2 gas is used to reduce the metal oxide before the CO gas effectively reacts with the Co catalyst. With 20 sccm of H_2 gas flow, temperature was increased to 780 ℃. At 780 ℃, the H_2 gas was pumped out and the CO gas was introduced at a flow rate of 200 sccm for 30 min. The sample was let cool down to room temperature under argon gas flow at a rate of 100 sccm. Figure 3.4 shows a carbon nanotube intra-connect grown by CO CVD.

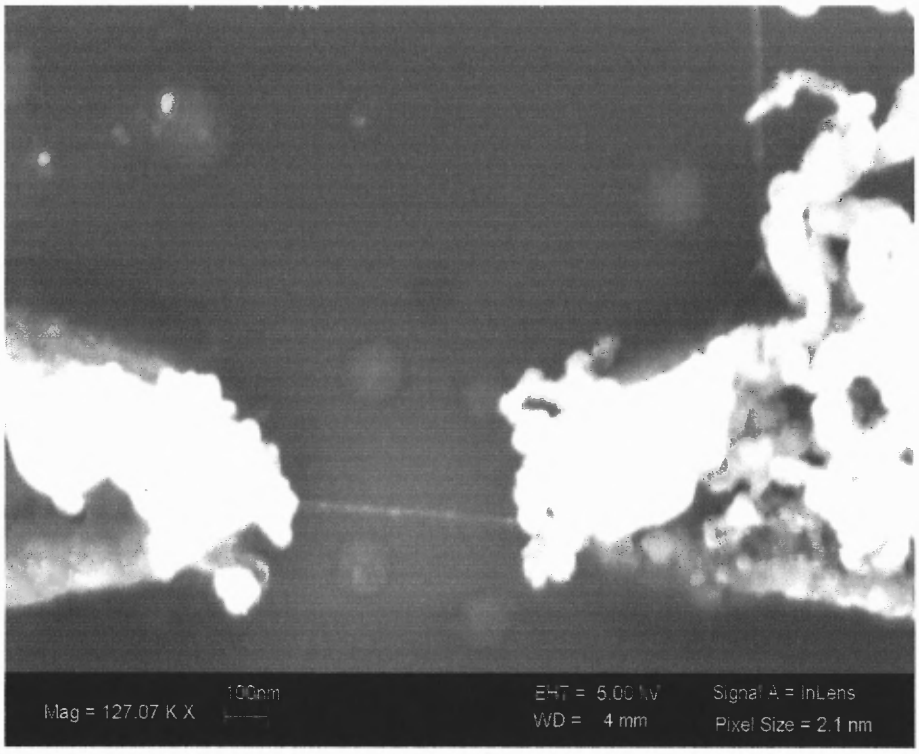

Figure 3.4 Carbon nanotube intra-connect grown by chemical vapor deposition using CO gas.

Ethanol CVD has been processed similarly to the CO CVD. Ethanol vapors were introduced into the quartz tube with an argon bubbler (Ar flow rate of 100 sccm). The argon and ethanol mixture was introduced into the quartz tube for 30 min (Figure 3.3(b)).

Methane gas (Figure 3.3(c)) was also used in our experiments. Here, the temperature was elevated to 550℃ under argon gas flow. Argon gas was pumped out and air was introduced for 10 minutes in order to oxidize the catalytic layer. The air was pumped out and an argon gas was introduced again. The sample was heated to 900℃ under argon flow. At 900 ℃, H_2 was introduced for 5 min with at a flow rate of 20 sccm. Then, methane and hydrogen mixture was introduced for one hour at a flow rate of 2000 sccm and 20 sccm, respectively. The sample was cooled down to room temperature under argon gas flow.

Methane gas was used to grow mostly single-walled carbon nanotubes. Ethanol and CO CVD had a tendency to result in mostly multi-walled carbon nanotubes.

3.3 Electrochemical Deposition of Conductive Polymer on CNT Intra-connects

Carbon nanotube intra-connects were electroplated with electrically conducting polymer, polypyrrole (PPy) and polycarbazole (PCZ). The electro-polymerization was carried out in a three-electrode-cell compartment. The working electrode was as-grown carbon nanotube intra-connect on metal electrode tips. A 1 mm thickness long platinum wire and Ag/AgCl electrode were used as a counter electrode and a reference electrode, respectively. A 273 EG&G Princeton Applied Research Potentiostat/Galvanostat was used to perform the electropolymerization process. Schematic of a three compartment electrochemical cell is shown in Figure 3.5.

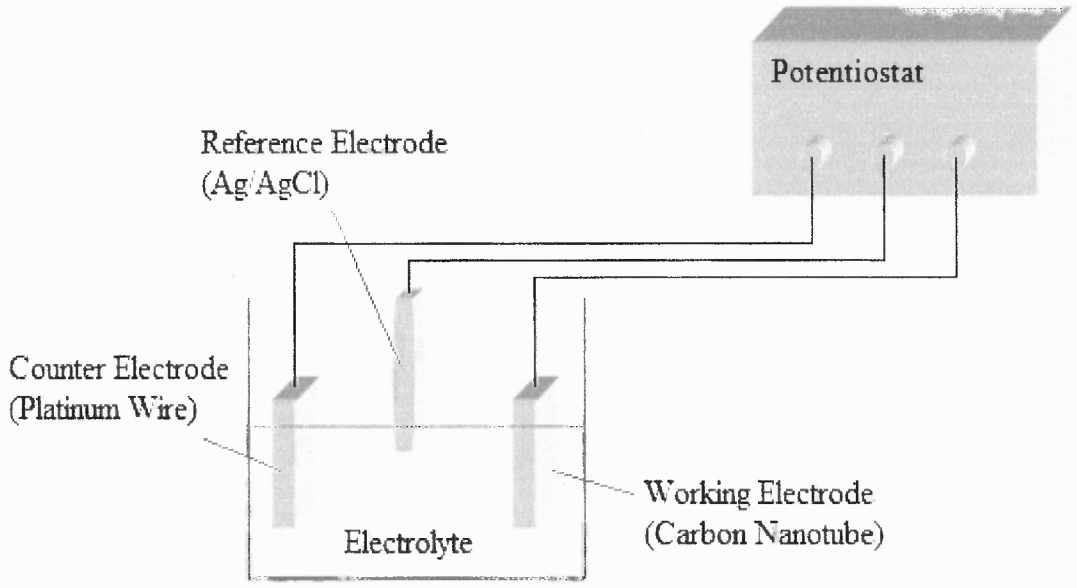

Figure 3.5 Schematic of electrochemical cell.

3.3.1 Cyclic Voltammetry

Cyclic voltammetry is used to study electron transfer mechanisms reversibility, reduction and oxidation potentials. The potential is cycled from an initial potential, E_i to a final potential, E_f and then back to E_i (Figure 3.6). The potential, at which maximum current occurs, is known as the peak potential, E_p. At this peak potential, the redox species are depleted at the electrode surface and the current is diffusion limited. The magnitude of the anodic peak current, I_{pa} and cathodic peak current I_{pc} is the rate at which the electrons are being transferred between the electrode and the redox species. Generally, the cyclic voltammetry process may be reversible or, irreversible [79].

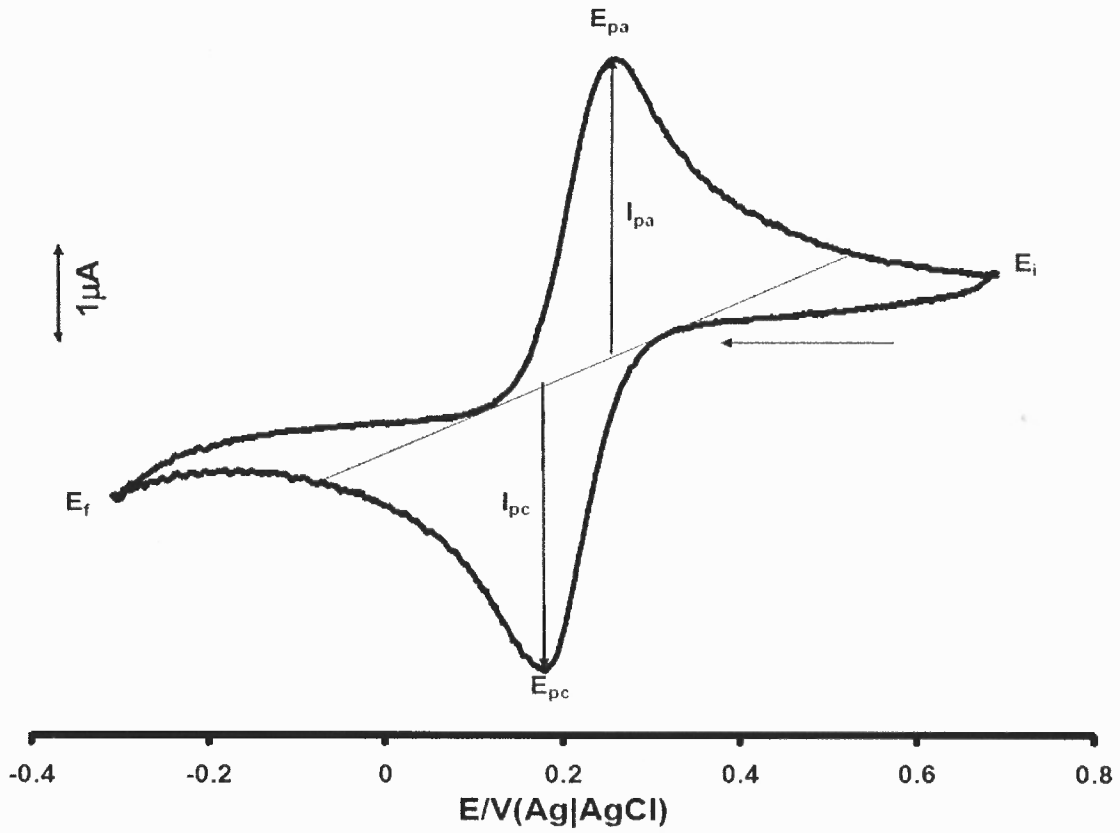

Figure 3.6 Typical cyclic voltammogram for a reversible process [79].

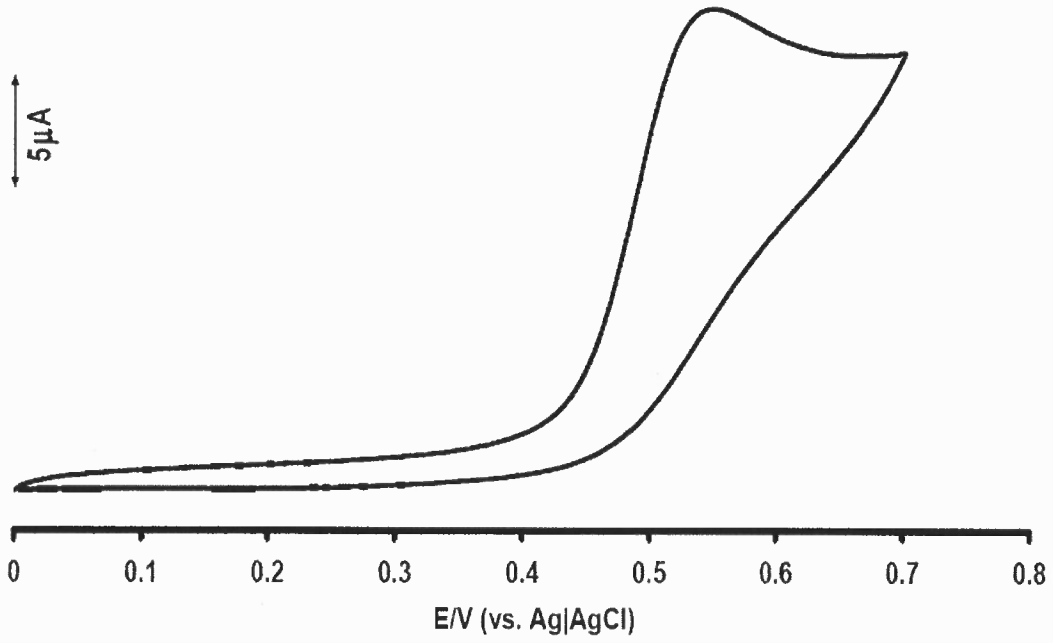

Figure 3.7 Typical cyclic voltammogram for an irreversible process [79].

In a reversible electrode reaction, the concentration of both the oxidized and the reduced species are in the equilibrium state. Figure 3.6 presents a typical cyclic voltammetry (CV) for a reversible electrode reaction. The half-wave potential ($E_{1/2}$) equals the formal potential ($E^{o'}$). The relation between the half-wave potential and the standard potential (E^{o}) is given by

$$E_{1/2} = E^{o'} = E^{o} + \frac{RT}{2F}\ln\frac{[O]}{[R]}. \tag{3.1}$$

Here, R is gas constant, T is temperature, F is Faraday's constant, [O] is the concentration of oxidized species (mol/L) and [R] is the concentration of reduced species (mol/L). The redox potential $E^{o'}$ is as follows:

$$E^{o'} = \frac{E_{pa} + E_{pc}}{2} \tag{3.2}$$

Where E_{pa} is the anodic peak potential and E_{pc} is the cathodic peak potential. The number of electrons transferred, n can be calculated as below:

$$\Delta E = E_{pc} - E_{pa} = \frac{RT}{nF}, \text{ at } 25\ ^{o}\text{C}\ \ \Delta E = \frac{0.059V}{n} \tag{3.3}$$

The peak current at 25 °C can be calculated by the Randles-Sevcik equation.

$$I_p = (2.69\times10^5)n^{3/2}[O]A(D\nu)^{1/2} \tag{3.4}$$

Where I_p is the peak current, A is the electrode area (cm^{-2}) and D is the diffusion coefficient (cm^2/s) and ν is the scan rate (V/s).

An irreversible electrode reaction is due to slow electron exchange or slow chemical reactions at the electrode surface. The electron transfer rate is insufficient to maintain the oxidation and reduction process at equilibrium. The peak current, I_p for an irreversible electrode reaction is as follows:

$$I_p = (2.99 \times 10^5) n[(1-\alpha)n]^{1/2} Ac(Dv)^{1/2} \quad (3.5)$$

Where α is the electron transfer rate, c is the concentration of the active species in mol/L. The CV experimental set up consist of a working electrode which can be gold, platinum, glassy carbon etc., a reference electrode against, which the potential is measured can be standard calomel electrode (SCE) or, silver/silver chloride (Ag/AgCl). The counter electrodes is typically made of platinum wire. During the CV, the solution is kept stationary and is not stirred in order to avoid movement of ions to the electrode surface by mechanical means [79].

3.3.2 Polypyrrole

Polypyrrole was synthesized by electrochemical oxidation of pyrrole. Using the CNT intra-connect as an electrode, the electro-polymerization process was carried out in a three-electrode-cell compartment consisting of an aqueous solution of 0.5M pyrrole and 0.5M potassium chloride (KCl) (Sigma-Aldrich) without further purification. All potentials were measured versus the Ag/AgCl reference electrode. A constant potential of 0.8 V (versus Ag/AgCl) was applied to electroplate the PPy for 30 sec. A black film, signifying the polymerization process, covered the carbon nanotube intra-connect. The sample was cleaned with deionized water and let dry out under nitrogen gas flow [80].

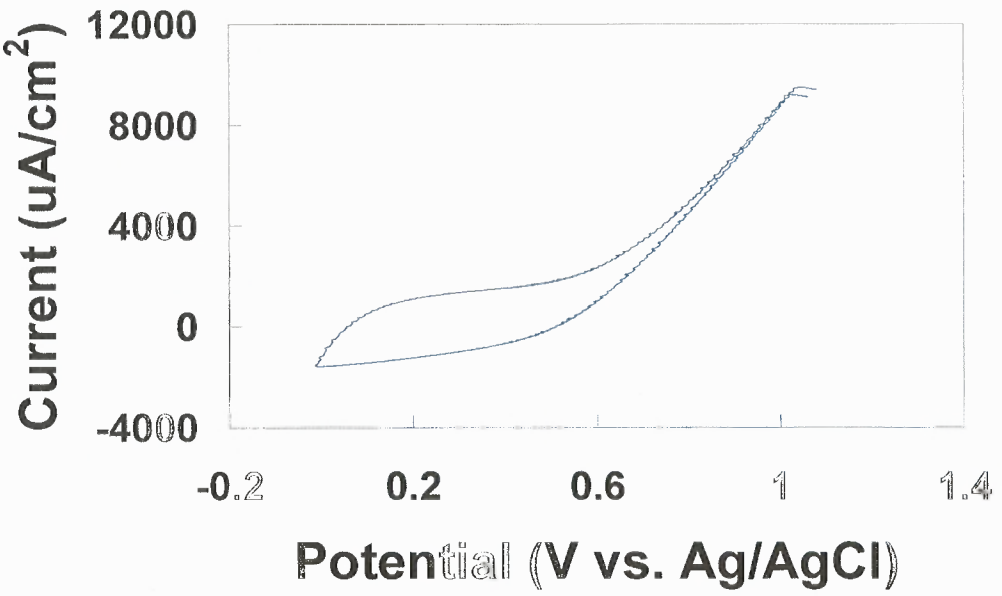

Figure 3.8 Cyclic voltammogram of pyrrole on conductive glass in deionized water. Scan rate of 100mV/s was used. The curve exhibits an irreversible trend.

3.3.3 Polycarbazole

The electrolyte was consisted of 0.02M carbazole monomer and 0.2M TBABF4 (tetrabutylammonium tetrafluoroborate) in acetonitrile. A constant potential bias of 1.2 V was applied to enable the deposition of PCZ [69, 70]. The film thickness was dictated by the deposition time, typically on the order of 30 sec and measured by use of atomic force microscope (AFM) later. A dark green film covered the metal electrodes and the carbon nanotube intra-connect alike yet, was limited to only conductive surfaces. The sample was later cleaned with deionized water and let dry out under nitrogen gas flow.

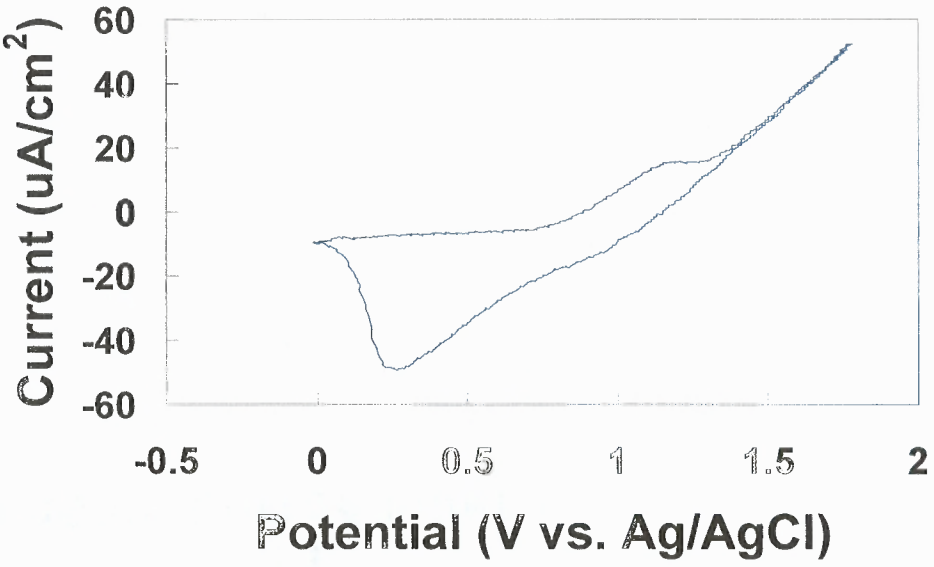

Figure 3.9 Cyclic Voltammogram of carbazole on conductive glass in acetonitrile. The scan rate was 100mV/s. The curve exhibits a quasi reversible trend.

3.4 I-V, I-V_g and Photoconductivity Measurement

The conductivity of CNT and CNT/ECP composite was characterized using Keithley 236 source-measure unit. The Keithely 236 was controlled by LabView software and connected to the computer through a GPIB board. All measurements, I-V, I-V_g and photoconductivity were compared before and after the electrodeposition of ECP on the CNT bridge. The I_{ds}-V_{ds} characteristics were measured from -0.5 V to 0.5 V or, from -1 V to 1 V. The I-V_g characteristics were measured at V_{ds}=1 V: the bias V_g was swept from 0 to -10 V repeatedly. The photoconductivity was measured after 10 minutes of exposure to white light radiation.

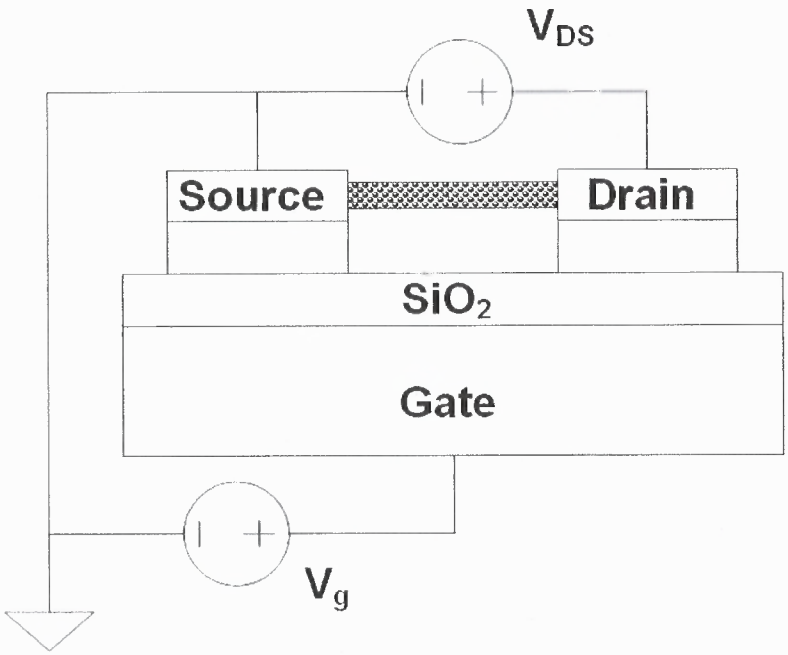

Figure 3.10 The configuration for electrical measurements.

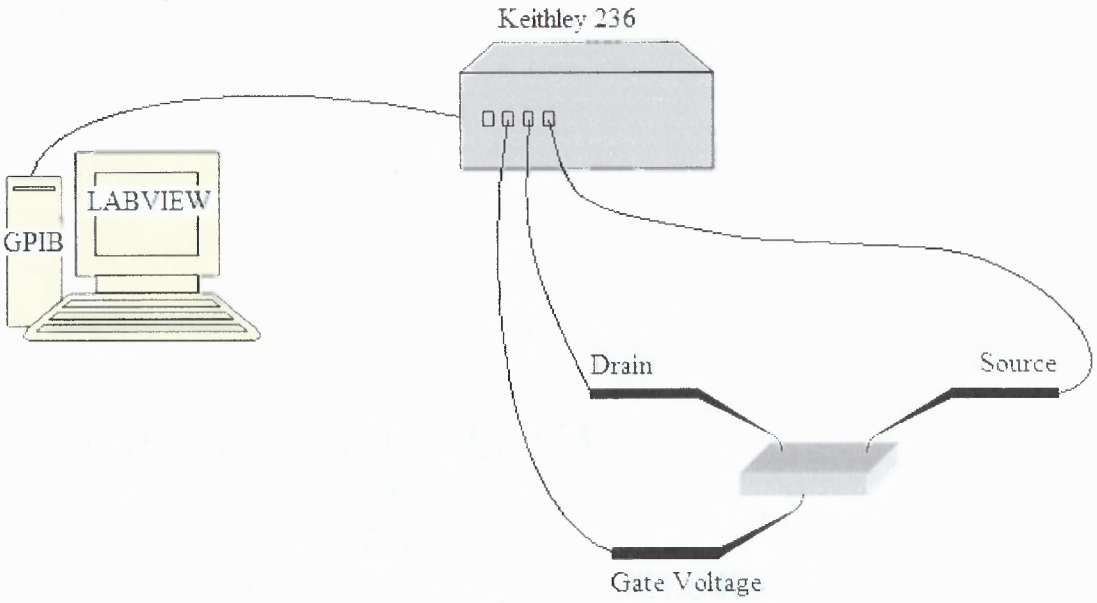

Figure 3.11 Probe station setup: the Keithley 236 was controlled by a LabView program through a GPIB board. Drain and Gate electrodes were properly grounded.

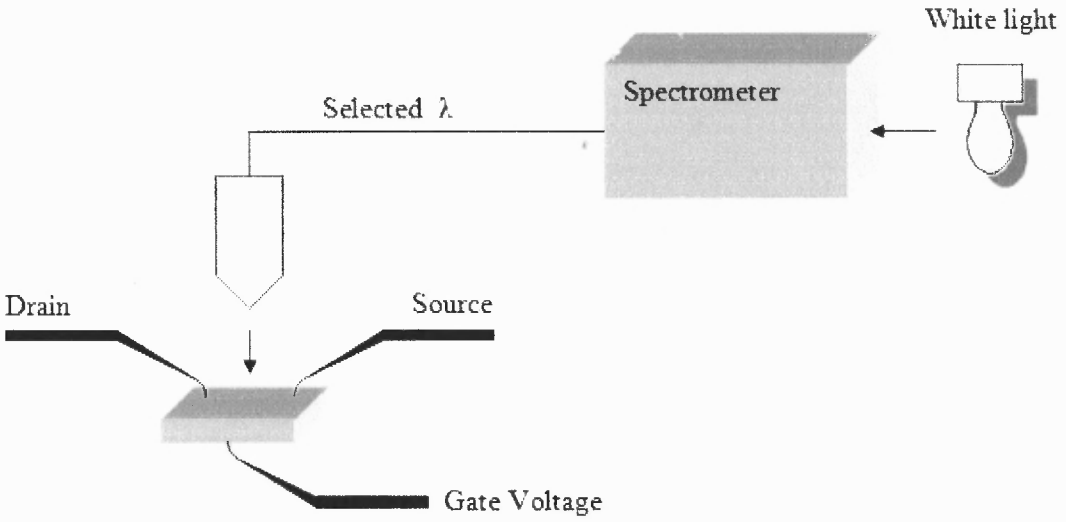

Figure 3.12 Configuration for photoconductance measurement. The sample was exposed to selected spectral bands of light.

3.5 Raman Spectroscopy

Raman spectroscopy is a useful technique to study the structures of carbon nanotubes and conductive polymers. The schematic of Raman spectroscopy setup is shown in Figure. 3.13. Raman spectra from CNT intra-connects were taken by using 514.5 nm argon ion laser, a double spectrometer and a charge coupled device (CCD) detector. The Raman spectra were collected for maximum for 30 minutes. An extended focal length x50 objective lens was used at laser intensities in the range of 10-40 mW. The metal electrodes were imaged in the far field and the laser beam was focused accurately between the electrodes' tips (Figure 3.14). The tip construction made it very easy to identify the CNT intra-connect under test. The diameter of laser spot size is a bit larger (>1 μm) than the spacing between the two electrodes and the Raman spectra could include signals from tubes which do not form a

conducting path. The background signal was subtracted from the signal away from the electrode region.

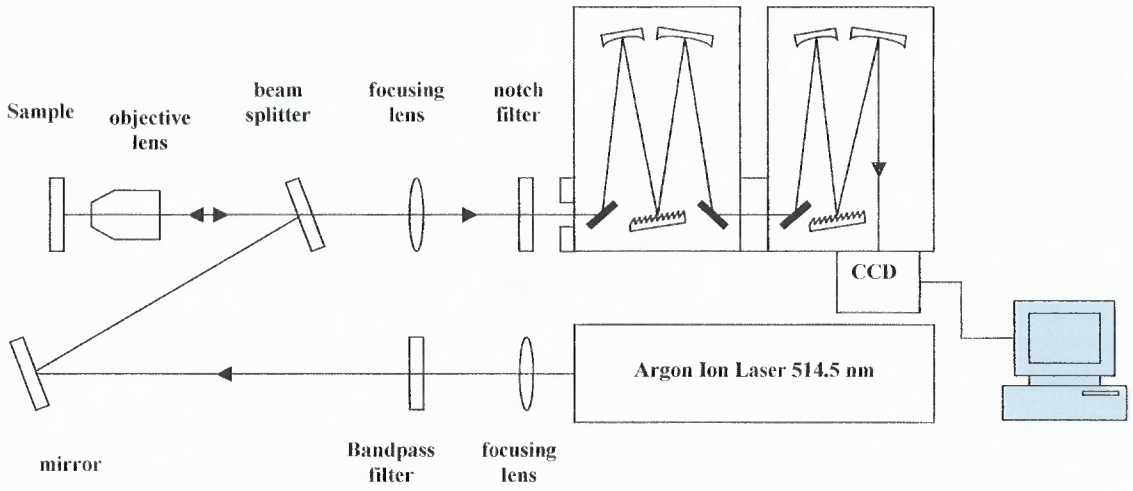

Figure 3.13 Schematic for the Raman spectroscopy setup.

Figure 3.14 Laser light was focused accurately between the two sharp electrodes to collect Raman scattering from carbon nanotube intra-connect.

CHAPTER 4

MWCNT/PPY

In this study, multi-walled carbon nanotube (MWCNT) intra-connects were grown by chemical vapor deposition using ethanol vapor at relatively low temperatures (~780 ^{o}C). MWCNT intra-connects were electroplated with electrically conducting polymer (ECP), polypyrrole (PPy). The growth of MWCNT intra-connects was made between very sharp metal electrodes at pre-determined positions as described in Chapter 3. The MWCNT intra-connects were then used as a working electrode for electroplating of conductive polymer, PPy. Characterizations were made by Raman spectroscopy and current-voltage measurements. The current-gate voltage (I_{ds}-V_{gs}) characteristics changed dramatically for the electroplated structures when the polymer exceeded a threshold thickness, on the order of 80 nm.

4.1 Electropolymerization and Raman Spectroscopy

Scanning electron microscope (SEM) pictures of electroplated MWCNT are shown in Figure 4.1. Raman scattering was measured to evaluate the intra-connects. The background signal was subtracted and the experimental data was fitted with several Gaussian distributions.

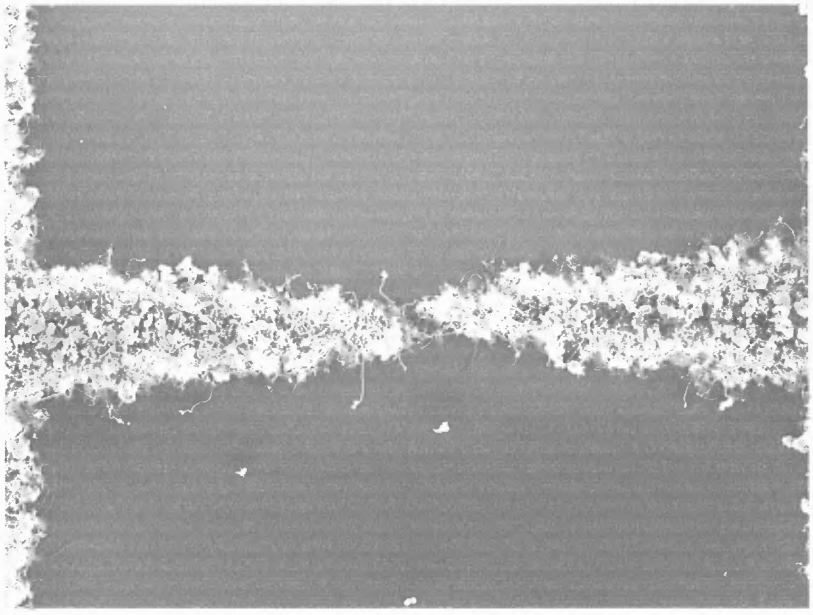

(a)

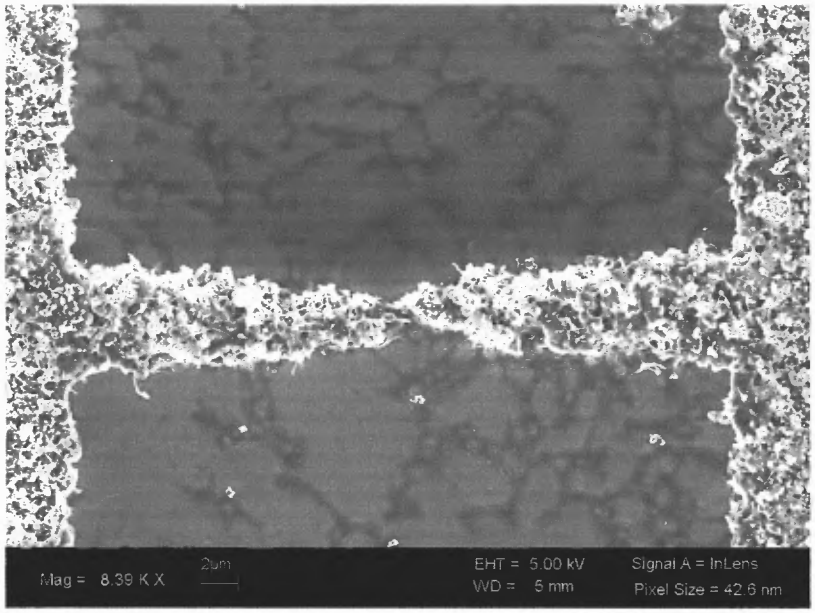

(b)

Figure 4.1 SEM images of multi-wall carbon nanotube intra-connects (a) before polymerization (b) after polymerization with PPy [80].

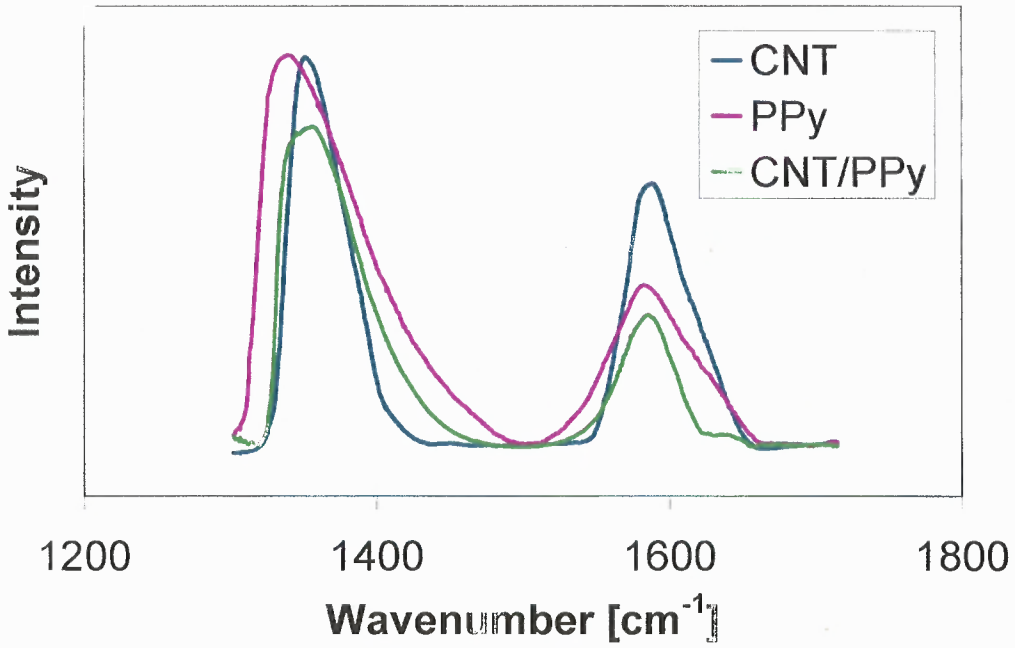

Figure 4.2 Raman spectra from multi-wall carbon nanotube intra-connects, electroplated PPy film on conductive glass and CNT/PPy intra-connects. The peaks from each component were at the following position: MWCNT intra-connects: 1350, 1585, 1619 cm^{-1}; PPy film: 1330, 1370, 1584 cm^{-1}; CNT/PPy intra-connects: 1357, 1585 cm^{-1}, respectively [80].

Figure 4.2 exhibits Raman spectra of multi-wall carbon nanotube (MWCNT) intra-connects, polypyrrole film and carbon nanotube/polypyrrole composites, respectively. Three major peaks were measured as expected for both CNT and PPy [81]. These are: CNT-only: 1350, 1585, 1619; PPy only: 1330, 1370, 1584 and CNT/PPy composites: 1357, 1585cm^{-1}, respectively. The relative peak position of CNT/PPy composites changed: the two CNT peaks at 1600 cm^{-1} merged into one, implying a weak interaction between the two layers. From these results and from the absence of an RBM peak, the Raman spectra indicate that these were MWCNT. No such signature was obtained when the laser spot was irradiating spots away from the electrode region.

4.2 Electrical and Optical Properties

Figure 4.3(a) shows current-voltage (I_{ds}-V_{ds}) characteristics for CNT and CNT/PPy intra-connects, respectively. The current was in μA range when 1 Volt was applied between the source and drain leads. After wrapping the CNT with PPy, the channel conductivity has been enhanced by more than ten times. The current value measured at V_{ds}=1 V was 2.97 μA for CNT only intra-connect, and it was 52.18 μA for the CNT/PPy intra-connect.

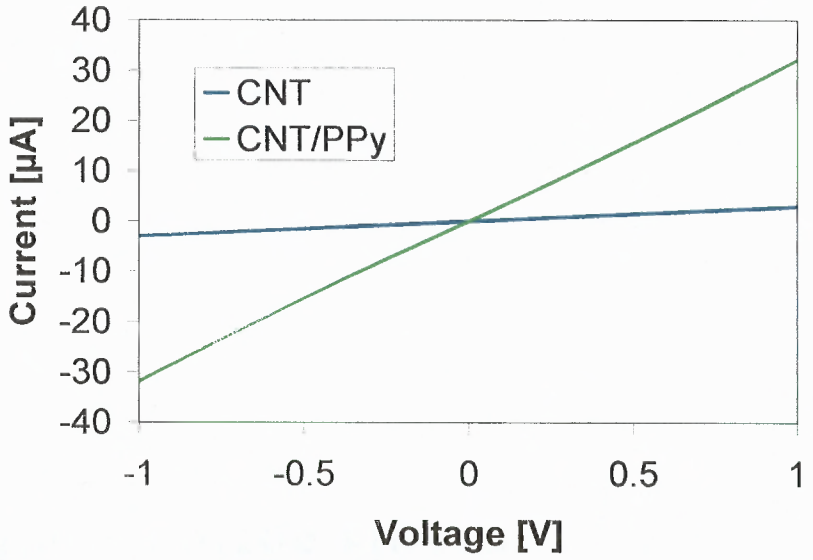

(a)

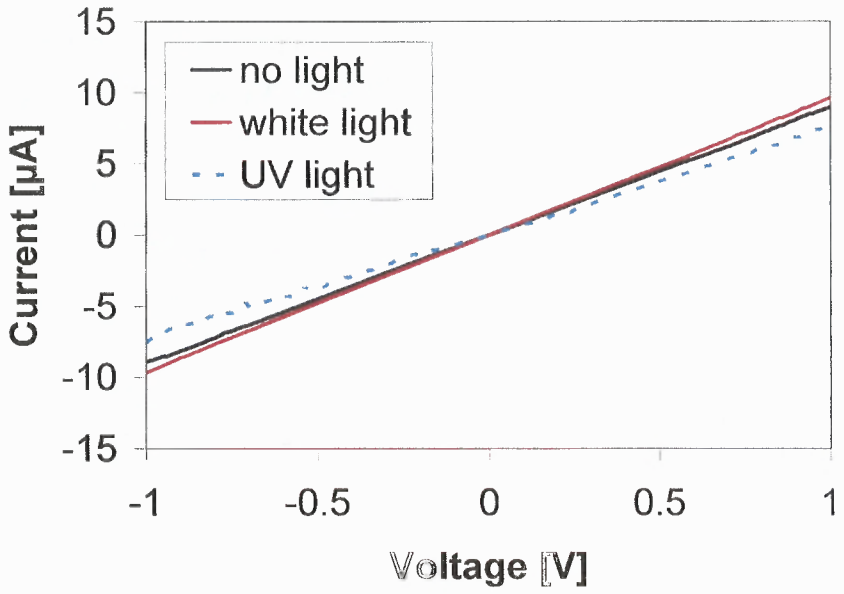

(b)

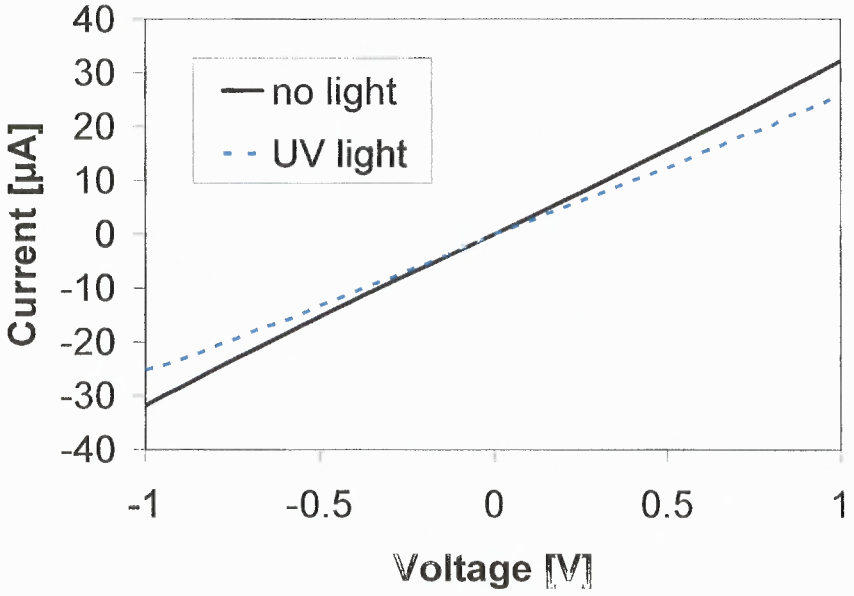

(c)

Figure 4.3 (a) I_{ds}-V_{ds} characteristics before and after polymerization of CNT intra-connects (b) Photosensitivity to white light and UV light on CNT only intra-connects (c) Photosensitivity to UV light to CNT/PPy intra-connect [80].

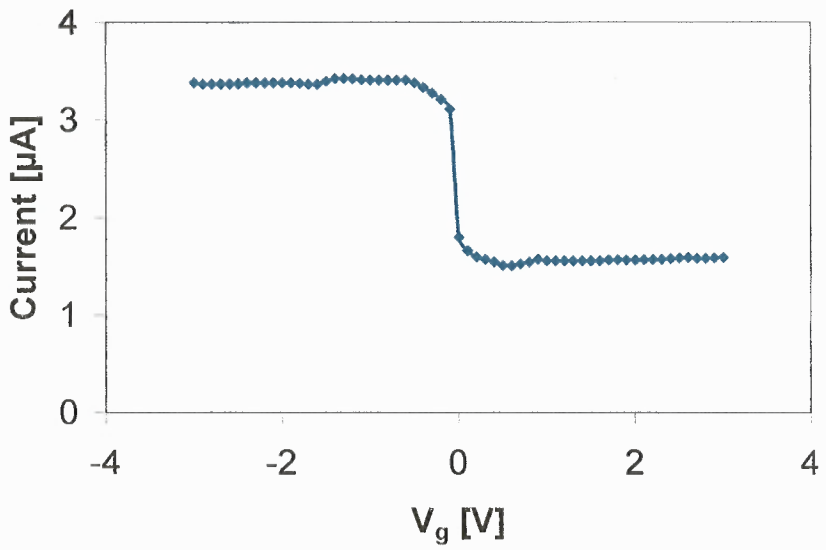
Current [μA]
4
3
2
1
0
-4
-2
0
2
4
V_g [V]

(a)

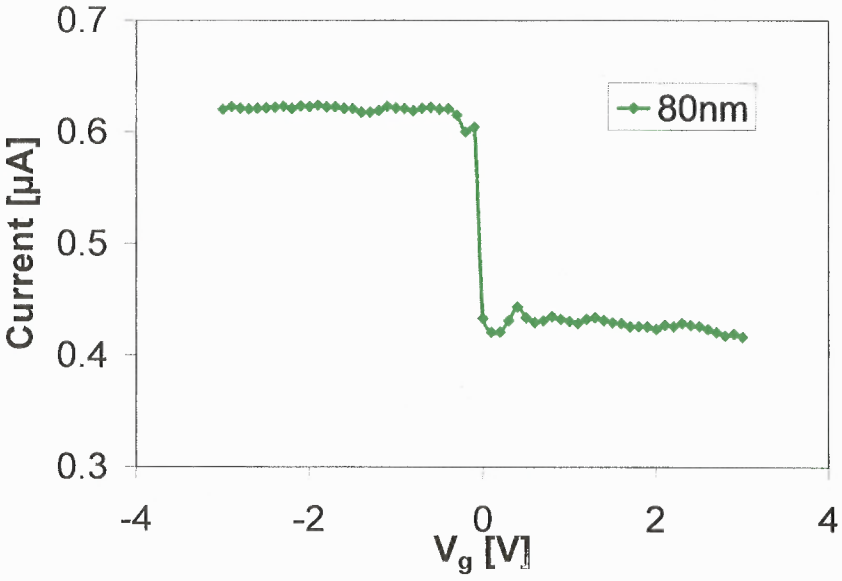
Current [μA]
0.7
0.6
0.5
0.4
0.3
80nm
-4
-2
0
2
4
V_g [V]

(b)

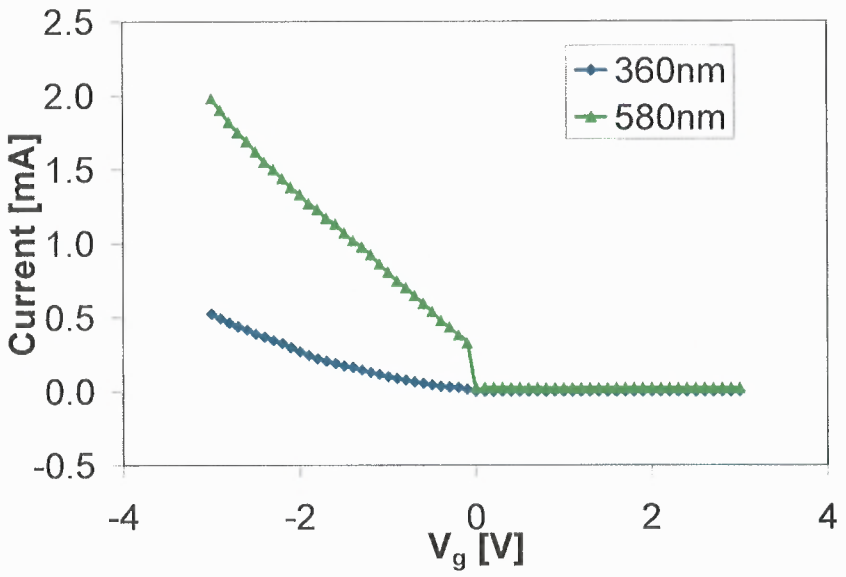

(c)

Figure 4.4 (a) I_{ds}-V_{gs} characteristics of multi-wall carbon nanotube intra-connect. (b) I_{ds}-V_{gs} characteristics from CNT/PPy intra-connect with 80nm thickness of PPy. (c) I_{ds}-V_{gs} characteristics from CNT/PPy intra-connect with thicker polymeric layer of 360 nm and 580 nm, respectively [80].

Photo-conductance was measured under white light and UV light exposure (Figure 4.3 (b)). The intensity of white light was 150 mW/cm^2 (λ>400 nm) and the CNT intra-connect exhibited moderate increase of photo-conductance. Under UV light exposure (intensity~4 mW/cm^2, λ=355 nm) the conductance decreased probably due to oxygen desorption.

Figure 4.3(c) shows photo-conductance from CNT/PPy intra-connect. Photo-conductance from CNT/PPy intra-connect was small due to the fact that only the CNT component is light sensitive. However, the CNT/PPy structure was very sensitive to UV light exposure (intensity~4 mW/cm^2, λ= 355 nm). The current dropped to zero and the intra-connect became open in less than a minute. It recovered to its previous state within a minute when the UV light source was removed. UV irradiation effects on CNT may be

attributed to oxygen desorption through reduction of hole carriers [82, 83]. As we shall see below, the effect on the PPy may be attributed to deep level impurities.

As-grown carbon nanotubes (CNT) are naturally p-type. Therefore, it requires negative gate voltage to operate in a gated configuration. A fixed 1 Volt was applied between the drain and source while the gate voltage was swept from -5 to +5 Volts. Silicon substrate was used as a back-gate electrode with 20 nm thick oxide layer (Figure 3.10) serving as the gate oxide. Figure 4.4(a) shows a typical I_{ds}–V_{gs} characteristic of an as-grown multi-wall CNT intra-connect. The current abruptly increased when a negative gate voltage was applied. The large saturation behavior may be due to weak gate dependence of the metallic-like MWCNT and the large gate capacitance. We also note that the position of the threshold voltage at which the transition occurs. The threshold value is small yet negative ($V_g < 0$ V) for the mostly MWCNT multiple and separated channels of this study. The threshold gate value is also negative however, much larger (on the order of −2 V to −5 V) for individual SWCNT intra-connects reported elsewhere [84]. Such observation accentuates the difference between SWCNT and MWCNT p-type channels. The current-gate voltage (I_{ds}-V_{gs}) characteristics changed dramatically for the electroplated structures when the polymer exceeded a threshold thickness, on the order of 80 nm (Figure 4.4 (b),(c)).

4.3 Model and Simulation

A simplified model is presented in Figure 4.5 (a). The multi-wall carbon nanotube intra-connect is assumed to be p-channel connected to the electrodes through back-to-back diodes. The model for multi-wall carbon nanotube intra-connects were simulated by MATHCAD. P-channel is characterized by a constant $C1=\mu \cdot C0 \cdot (W/L)$ where μ is channel mobility, C0 is the gate capacitance and W/L is the ratio between the channel width and channel length. The ratio W/L was very small since W was on the order of a few nanometer and L was 1 μm. The channel mobility and gate capacitance was large. Relatively large constant C1 value is led to a step behavior in the I_{ds}-V_{gs} characteristics (Fig 4.5 (b), from curves (1) to (2)). As the thickness of the polymeric sheath on the CNT intra-connect increases, W/L increases only slightly; the capacitance of the structure C0 remains basically unaffected however; the overall channel mobility is substantially reduced—by two orders of magnitude due to the low mobility value of the polymer. The mobility of carbon nanotube and the mobility of polypyrrole are approximately 5×10^4 $cm^2/V \cdot s$ and $500 cm^2/V \cdot s$, respectively [85, 86]. As a result, the I_{ds}–V_{gs} curve becomes more linear (Fig 4.5 (b). from curves 1 and 3). The difference between the current amplitudes of Figure 4.4 (a)-(c) is attributed to the decrease in the overall circuit resistance since the polymers coats the metal electrodes, leading to the intra-connect, as well. When the polymer coats the electrodes and the intra-connect, the contact barrier between the CNT channel and the electrodes is substantially reduced. The seemingly 2:1 factor between the ON and OFF states of the bridge depends on the p-channel and the con-tact diodes' properties. Ratios of 3:1 for these CNT intra-connects have been experimentally observed and corroborated by simulations.

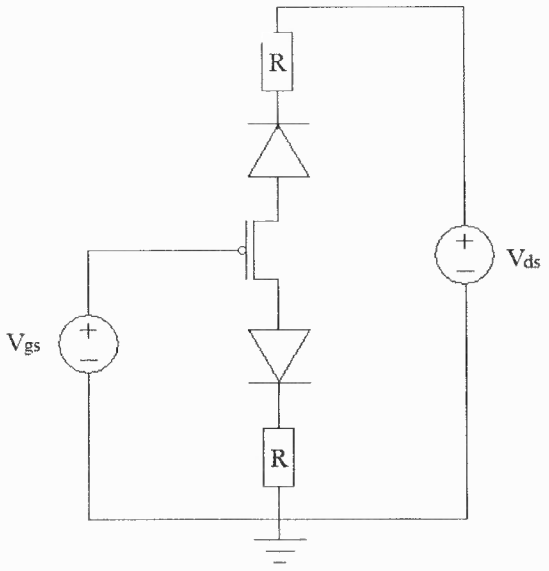

(a)

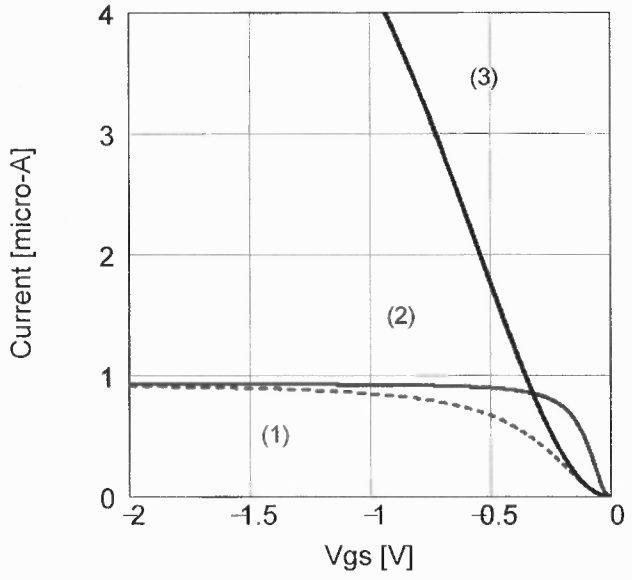

(b)

Figure 4.5 (a) Simplified equivalent circuit model of multi-wall CNT intra-connect (b) Simulated results (1) R=1MΩ, C1=10^{-5}. (2) R=1MΩ, C1=10^{-4}. (3) R=100kΩ, C1=10^{-5}. The threshold voltage from simulated curves was very small, V_T=0.01 V [80].

CHAPTER 5

SWCNT/NDR

As grown single-walled carbon nanotube (SWCNT) intra-connects grown by chemical vapor deposition process using methane/hydrogen gas mixture were investigated as gated structures. We demonstrated a negative differential resistance (NDR) effect at nonzero gate bias even with seemingly ohmic contacts. Large differential photo conductance (DPC) was associated with the NDR effect raising hopes for the fabrication of novel high-speed optoelectronic devices.

5.1 I_{ds}-V_{ds} Characteristics and Raman Spectra

Two examples will be discussed here, one exhibiting nonlinear and the other linear electrical characteristics.

Figure 5.1 (a)-(c) shows SEM, I_{ds}-V_{ds}, and Raman spectra of Sample 1. The nonlinear I-V curve at zero gate voltage indicates a presence of potential barrier between the tube and metal contact(s). The asymmetry in the curve points to one dominant barrier (otherwise, the curve would have been symmetric). Its Raman spectra are shown in Figure 5.1 (c) low frequency spectra exhibit a narrow single peak (5 cm^{-1} wide and limited only by the system resolution) for the radial breathing mode (RBM) at 191.9 cm^{-1}. The peak may indicate a metallic tube (12,6) with an average diameter of 1.252 nm. It exhibits a very large graphitic line at 1355 cm^{-1}, which may indicate defects or, large stress. The high frequency region exhibits two peaks at 1594 cm^{-1} and 1567 cm^{-1}, respectively. Their frequency difference 27 cm^{-1} corresponds to a tube diameter d = 1.716 nm if we follow [87]

and assume a metallic type tube. It corresponds to a tube diameter d = 1.329 nm assuming semiconductor type.

Sample 2 exhibits linear I_{ds}-V_{ds} characteristics at zero gate bias (Figure 5.1(e)). Its low frequency Raman spectrum consists of a broader single RBM peak (30 cm^{-1} wide) centered at 176.2 cm^{-1}, which implies semiconductor tube(s) (11,9) with an average diameter of 1.365 nm. It exhibits a large defect line at 1352 cm^{-1}. The high-frequency frequency exhibits two peaks at 1596 and 1578 cm^{-1}, respectively. Their difference 18 cm^{-1} implying tube diameters d = 2.101 nm and d = 1.628 nm for metallic or semiconductor type tubes, respectively.

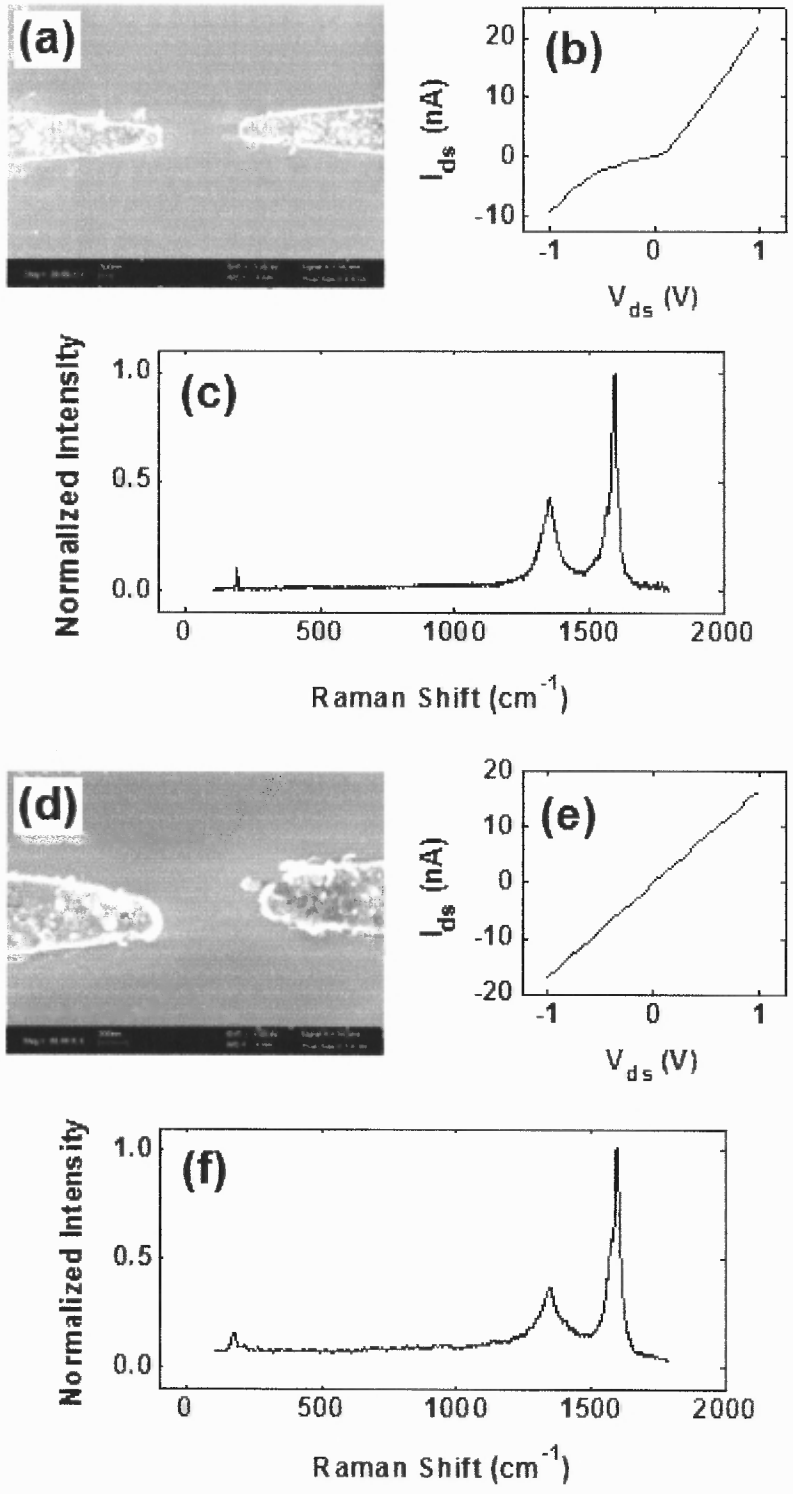

Figure 5.1 Sample #1: (a) SEM image of CNT intra-connect. (b) nonlinear I_{ds}-V_{ds} characteristic. (c) Raman spectra with RBM at 191.9 cm^{-1}. Sample #2: (d) SEM image of CNT intra-connect. (e) linear I_{ds}-V_{ds} characteristic. (f) Raman spectra with RBM at 176.2 cm^{-1} [84].

5.2 NDR in I_{ds}-V_{gs} Characteristics and Photoconductance

Electrical properties in the dark and under white light illumination were measured for Sample 1 (Figure 5.2) and Sample 2 (Figure 5.3). The channel formed by the intraconnects exhibited a natural *p*-type characteristics owing to the presence of oxygen in the tubes.

Figure 5.2(a) shows a map of V_{gs} vs V_{ds} for the non-illuminated intra-connect. Two negative differential resistance (NDR) regions may be observed in the I_{ds}-V_{gs} plot: one, in the range between -3 and -6 V and the other, around -9 V (Figure 5.2(b)-(c)). The NDR peak for the first region was shifting to the negative side as the V_{ds} value increased from 0.25 to 0.75 V (Figure 5.2(c)). The second NDR region was stable around -9 V. Characteristics of the same intraconnect under illumination are shown in Figure 5.2(d)-(f). Surprisingly, the light did not mask the NDR effect (Figure 5.2(f)) but locked it to the same V_{gs} range for all V_{ds} values used. The differential photo conductance (DPC, the difference between conductance in the dark and under light illumination) was fluctuating rapidly within the first NDR range (Figure 5.2(g)).

Figure 5.3(a) shows a map of V_{gs} vs V_{ds} for nonilluminated intraconnect. Two negative differential resistance (NDR) regions are observed in the I_{ds}-V_{gs} curve as well: one in the range between -3 and -6 V and another around -9 V (Figure 5.3(b),(c)). The NDR peak for the first region was shifting albeit in both negative and positive directions as V_{ds} increased from 0.25 to 0.75 V. The second NDR region was stable around -9 V. The same intraconnect under white light illumination is shown in Figure 5.3(d)-(f). Here, the light somewhat masked the NDR effect (Figure 5.2(f)) for the first V_{gs} region but left a small but noticeable presence around $V_{gs} \sim$ -9 V. The DPC was stable and exhibited a marked increase for increasing V_{ds} (Figure 5.3(g)).

NDR effect is the basis for many microwave oscillators. The effect may be attributed to two competing transport venues, for example, nonlinear drift and thermionic venues or tunneling and thermionic excitation processes. In addition, optimal construction typically breaks the symmetry between the contact to and from the channel. For example, a CNT channel extending between two different metals, which takes advantage of the metals' different work functions and the distribution of the tube's electronic density of states.

In contrast, both of our electrodes were made of the same metal and hence we resorted to a gated configuration. The gate bias affects the distribution of carriers along the tube. If we postulate the existence of a secondary interface between the CNT channel and electrode, possibly in a form of a point Schottky contact or a quantum dot (QD), gate biasing affects the distribution of electronic states across such barrier, as well. We point to the very small, 1 nm thick catalytic seed film in our structures, which may result in a point contact during the tube's growth process. Tunneling may now occur between the tube and discrete states in this metal dot.

The secondary NDR region for both samples may imply tunneling through a second QD band. Tunneling and transport must depend on the relative energy states' distribution between dot and channel, as well as, on the gate bias. NDR was also noted in our previous experiments while using another growth technique albeit at larger gate bias [88].

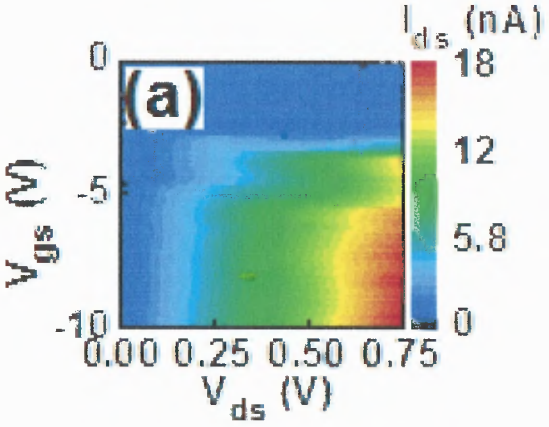
(a)
I_{ds} (nA)
18
12
5.8
0
0
-5
-10
V_{gs} (V)
0.00 0.25 0.50 0.75
V_{ds} (V)

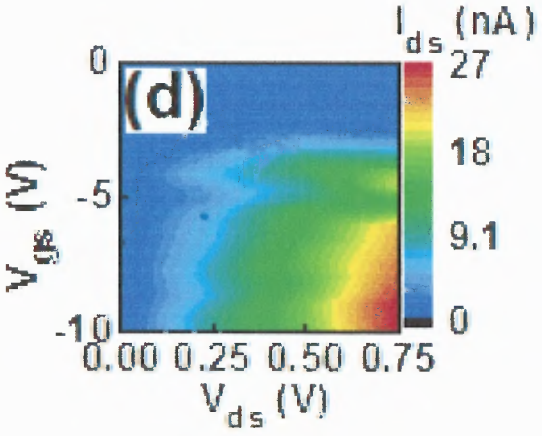
(d)
I_{ds} (nA)
27
18
9.1
0
0
-5
-10
V_{gs} (V)
0.00 0.25 0.50 0.75
V_{ds} (V)

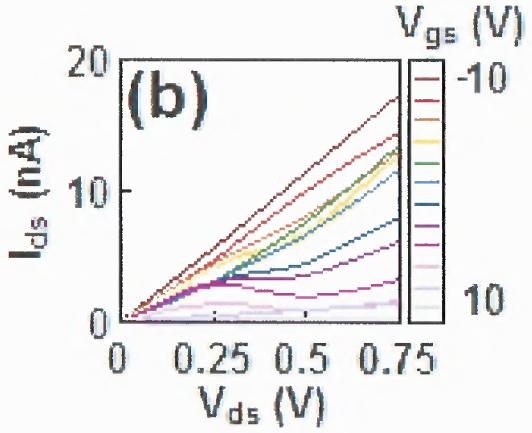
(b)
V_{gs} (V)
-10
10
20
10
0
I_{ds} (nA)
0 0.25 0.5 0.75
V_{ds} (V)

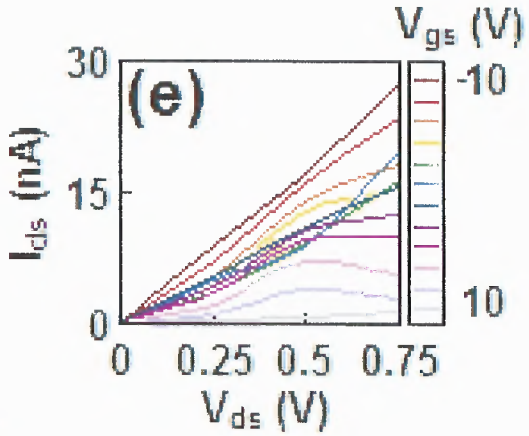
(e)
V_{gs} (V)
-10
10
30
15
0
I_{ds} (nA)
0 0.25 0.5 0.75
V_{ds} (V)

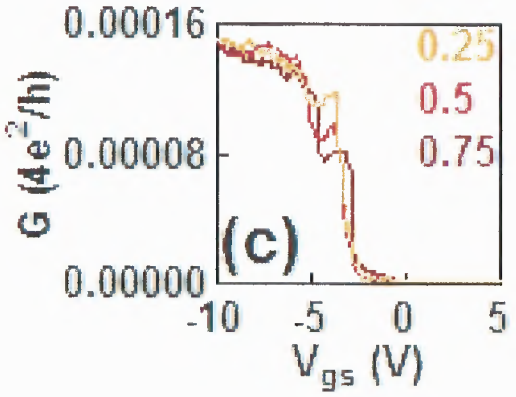
(c)
0.25
0.5
0.75
0.00016
0.00008
0.00000
G ($4e^2/h$)
-10 -5 0 5
V_{gs} (V)

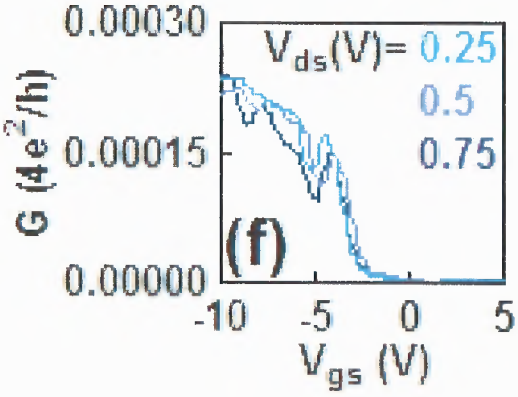
(f)
V_{ds}(V)= 0.25
0.5
0.75
0.00030
0.00015
0.00000
G ($4e^2/h$)
-10 -5 0 5
V_{gs} (V)

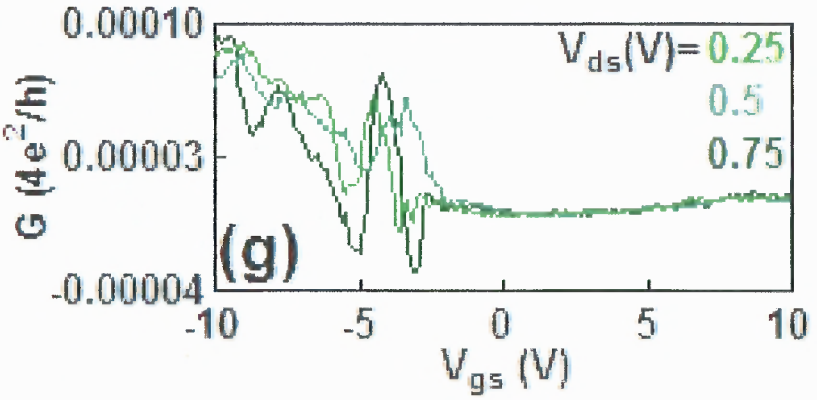

Figure 5.2 Electrical properties of sample #1 before and after white light exposure. (a) I_{ds}-V_{ds}-V_{gs} characteristics. Negative differential resistance was observed for V_{gs} between -2 and -6. (b) I_{ds}-V_{ds} characteristics for various V_{gs} values from +10 to -10. I_{ds}-V_{ds} curves become nonlinear when the gate voltages for a negative differential region are applied. (c) G-V_{gs} characteristics. Panel a is converted into conductance, G. (d) I_{ds} vs V_{gs} and V_{ds} characteristics after irradiation of white light. (e) I_{ds}-V_{ds} characteristic for various V_{gs} values from +10 to -10. I_{ds}-V_{ds} curves become nonlinear when the gate voltages for a negative differential region are applied. (f) G-V_{gs} characteristics under illumination. (g) Photo differential conductance [84].

Sample 1 is probably made of individual or of a few tubes as judged by the narrow Raman RBM spectra; its current only weakly dependent on gate voltage and one may attribute its behavior to mostly the Schottky point interface. Its sensitivity to the contact with electrodes led to the asymmetry in the I_{ds}-V_{ds} curve. In contrast, sample 2 is probably made of a small bundle thus is more likely to portray ohmic contact at zero gate bias.

Sample 2 is more responsive to the gate bias as expected of a semiconductor channel. Raman classification of the tubes may be distorted by stress and contact to the substrate. In addition and despite careful alignment (see Chapter 5.4), the laser spot may cover tubes, which do not contribute to electrical conduction yet, may be at resonance with the laser line thus, affecting the Raman spectra. This could imply that both samples were of semiconductor type if we mainly base our conclusion on a self-consistent value for the

tube's diameter. In that case, the samples differ only by the number of tubes in their respective bundles. Nevertheless, Raman spectroscopy is an important characterization tool, which corroborates the existence of nanotubes between electrodes and helps determine their type, thus complementing conductance measurements.

The characteristics of the channel under broadband optical excitation corroborated these findings, as well. Optical induced carriers in the channel overcame the tunneling process, hence the marked conductivity change for the first NDR region (around -5 V). The optical effect is smaller for the "nonlinear" sample 1 because of the interfering effect from the contact barrier. Moreover, since photo-excited carriers are composed of both types (holes and electrons), *n*-type characteristics at large positive gate voltages ought to be exhibited. Indications to such behavior are provided in Figure 5.3(g). Furthermore, when the graphs are plotted as log plots (not shown) such characteristics are greatly accentuated. Both panels (c) and (f) of Figure 5.2 indicate a relatively sharp "ON" transition, which implies large channel mobility with back-to-back leaky Schottky diodes. The ON transition in Figure 5.3(c),(f) tends to have quadratic behavior as expected from an ordinary semiconducting channel.

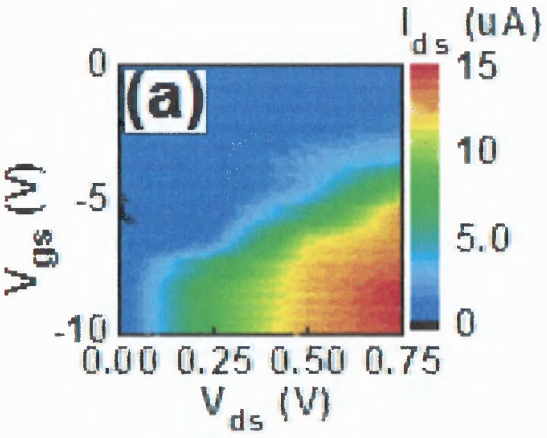
(a)
I_{ds} (uA)
15
10
5.0
0
0
-5
-10
V_{gs} (V)
0.00 0.25 0.50 0.75
V_{ds} (V)

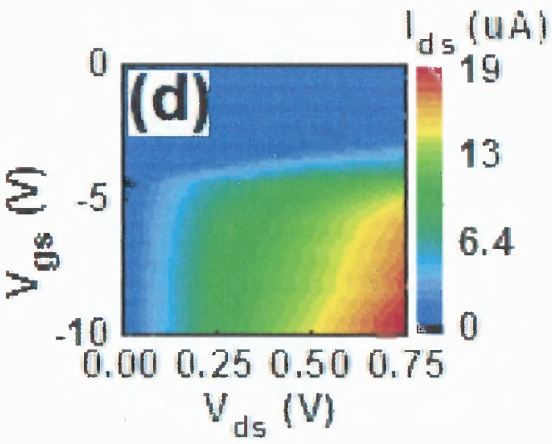
(d)
I_{ds} (uA)
19
13
6.4
0
0
-5
-10
V_{gs} (V)
0.00 0.25 0.50 0.75
V_{ds} (V)

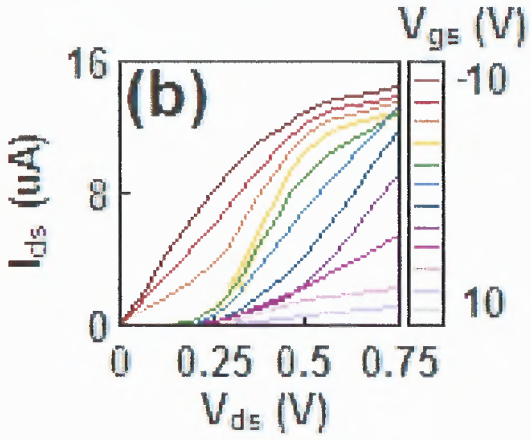
(b)
V_{gs} (V)
-10
10
16
8
0
I_{ds} (uA)
0 0.25 0.5 0.75
V_{ds} (V)

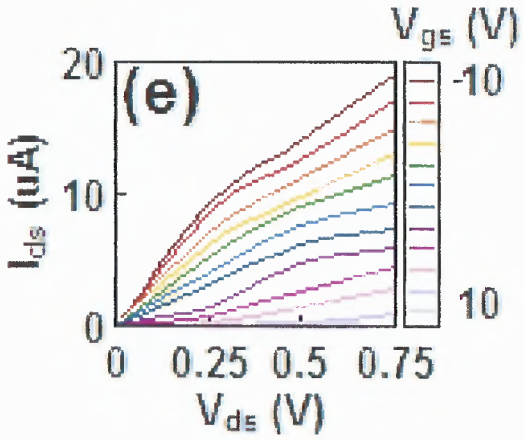
(e)
V_{gs} (V)
-10
10
20
10
0
I_{ds} (uA)
0 0.25 0.5 0.75
V_{ds} (V)

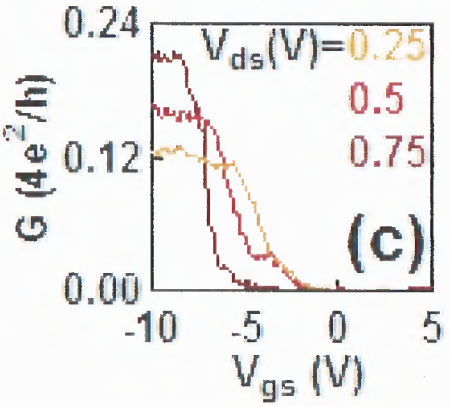
(c)
V_{ds}(V)=0.25
0.5
0.75
0.24
0.12
0.00
G ($4e^2/h$)
-10 -5 0 5
V_{gs} (V)

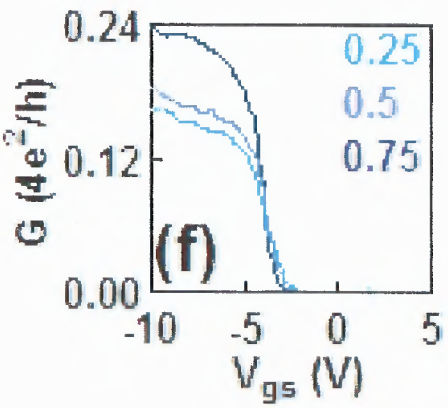
(f)
0.25
0.5
0.75
0.24
0.12
0.00
G ($4e^2/h$)
-10 -5 0 5
V_{gs} (V)

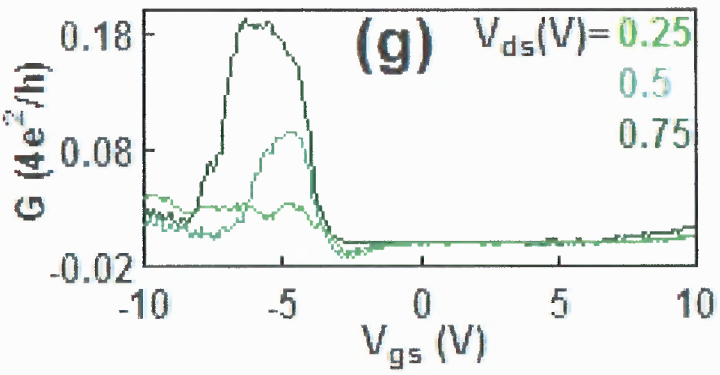

Figure 5.3 Electrical Electrical properties of Sample 2 before and after white light illumination. (a) I_{ds}-V_{gs}-V_{ds} characteristics. (b) I_{ds}-V_{ds} characteristic for various V_{gs} values from +10 to -10. (c) G-V_{gs} characteristics. Panel a is converted into conductance, G. (d) I_{ds}-V_{gs}-V_{ds} characteristics under white light illumination. Overall current was enhanced and the device became stable with less noise. (e) I_{ds}-V_{ds} characteristic for various V_{gs} values from +10 to -10. I_{ds}-V_{ds} curves become nonlinear when the gate voltages for a negative differential region are applied. (f) G-V_{gs} characteristics under illumination. (g) Photo differential conductance [84].

5.3 Hysteresis Measurement

Surface states play an important role in such devices. We observed hysteresis upon ramping the gate voltage in the negative and positive directions (Figure 5.4). The lower curves are always in the negative direction while the top curves are scanned from negative to positive gate bias values. The hysteresis did not change the presence of NDR which means that the latter is inherent to the tube/electrode contact but not to its surface. After a few scans, the hysteresis became narrower. This is to be expected of surface states. In addition, clockwise hysteresis is indicative of movable ions or, adsorbed water molecules (in contrast to charge trapped in the underlined oxide layer - the latter results in counterclockwise hysteresis curve). Yet, sample 1 exhibited a large hysteresis and sample 2 exhibited almost a replica of the curve in the negative and positive gate bias ramp. That may be understood if the channel of sample 1 is composed of only few or even individual

carbon nanotube. The effect of surface states must have been larger here than their effect on sample 2 with a larger bundle of tubes.

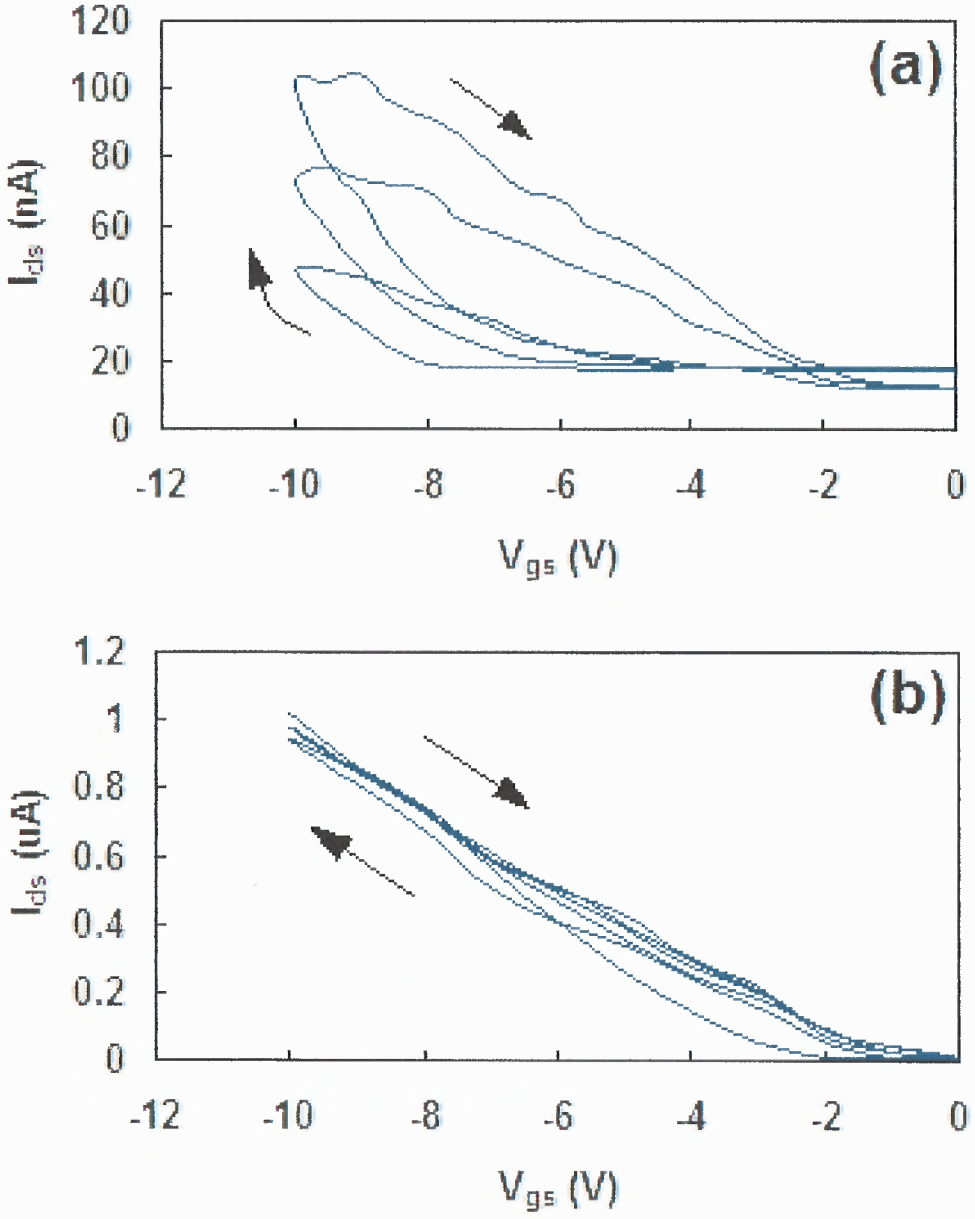

Figure 5.4 Hysteresis curves under dark conditions (a) Nonlinear case, sample #1 (b) Linear case, sample #2. The arrows point the direction of the scan. In panel a, the overall current increased for increasing numbers of scans until stabilizing [84].

5.4 Electrical Measurement from More Intra-connects

Good quality bridges are often barely seen in these SEM pictures, hence the use of Raman spectroscopy and conductivity measurements. Our present batch consisted of 14 samples (9 samples conducting: 4 – linear; 5 – nonlinear), is taking into account cases, which do not show up in SEM pictures yet, exhibited conductance and Raman signature. Temperature is critical to a successful SWCNT growth: lower yield (2 conductive samples out of 14) was exhibited at lower temperatures deviating only by 50 ^{o}C. Current-voltage (I-V) curves were measured using Keithley 236 with current noise level <1 pA using sharp probes (~5 μm, Cascade Microtech). The probes were placed under a microscope interfaced with a CCD camera for better inspection. Gate-current measurements were made with the Si wafer acting as a back electrode. The conduction through a CNT bridge at V_{ds}=1 V was at least three orders of magnitudes larger than the noise and/or the current through or, along the silicon and/or electrode/silicon path. The signal, carried by triax cables, was averaged during a period larger than the RC constant (τ < 0.03 sec) of the circuit. Two more examples of 'linear' and 'non-linear' contacts are shown in Figure 5.5 and Figure 5.6, respectively. The SEM images of the bridge under test are provided, as well. Clearly seen is the breakdown of the upper Co layer. The resistance of the electrode (~10 ohms/ 100 microns) did not change much before and after annealing. This is to be compared to the bridge resistance of several tens of megaohms. Both samples exhibited NDR around V_{gs}=−5 V and −10 V, respectively. The clearer picture is again for the 'linear case'. We note that previous measurements [88, 89] also exhibited NDR, which at the time, were not fully pursued. These bridges were fabricated using CVD with another precursor (CO) and similar layout of electrodes (with the exception of a thicker Co layer of 30 nm). Such

precursor requires lower processing temperatures (~750 ^{o}C). Thicker Co layer resulted in occasional growth of multi-walled carbon nanotubes. Due to the sensitivity of the process to temperature fluctuations, a critical factor is therefore, the actual temperature at the substrate surface. This is affected by several factors such as, the gas flow, the location of the sample in the CVD chamber, the heat capacity of the sample holder, etc.

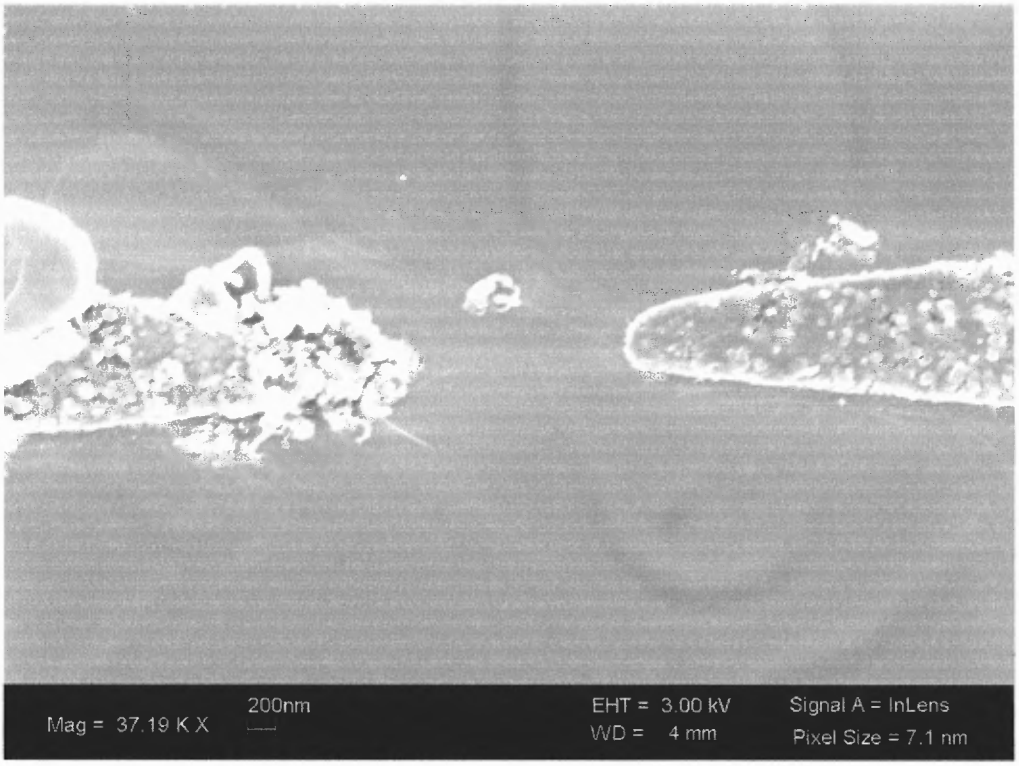

(a)

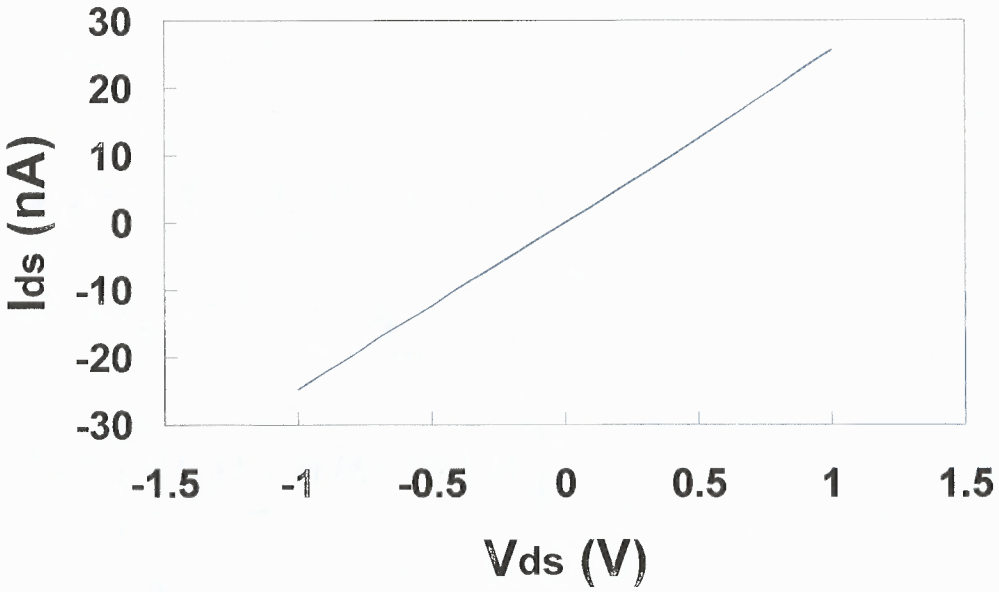

(b)

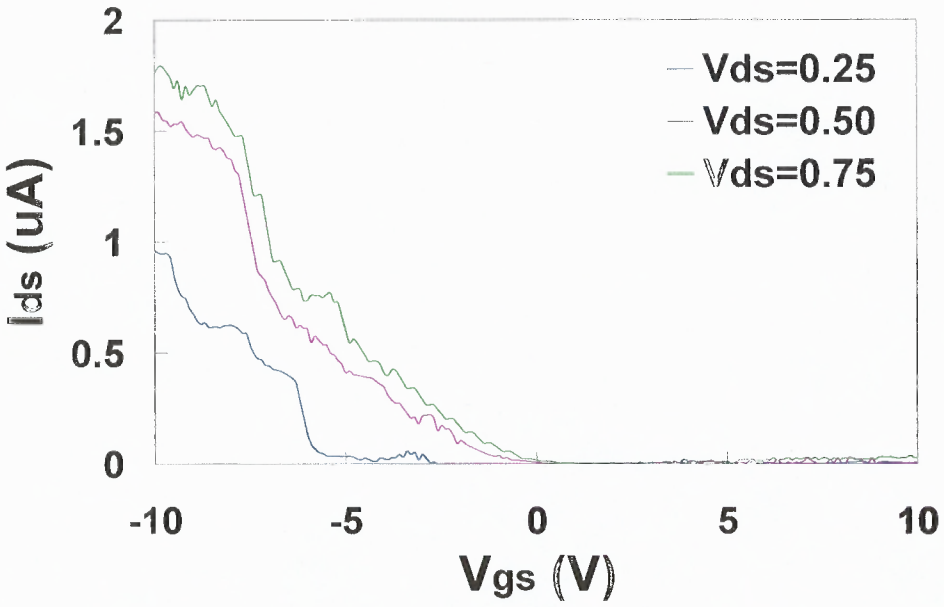

(c)

Figure 5.5 Another example of carbon nanotube intra-connects showing linear I_{ds}-V_{ds} characteristics and negative differential resistance in I_{ds}-V_{gs} characteristics. (a) SEM image of carbon nanotube intra-connects (b) I_{ds}-V_{ds} characteristics; linear (c) I_{ds}-V_{gs} characteristics; NDR is observed [84].

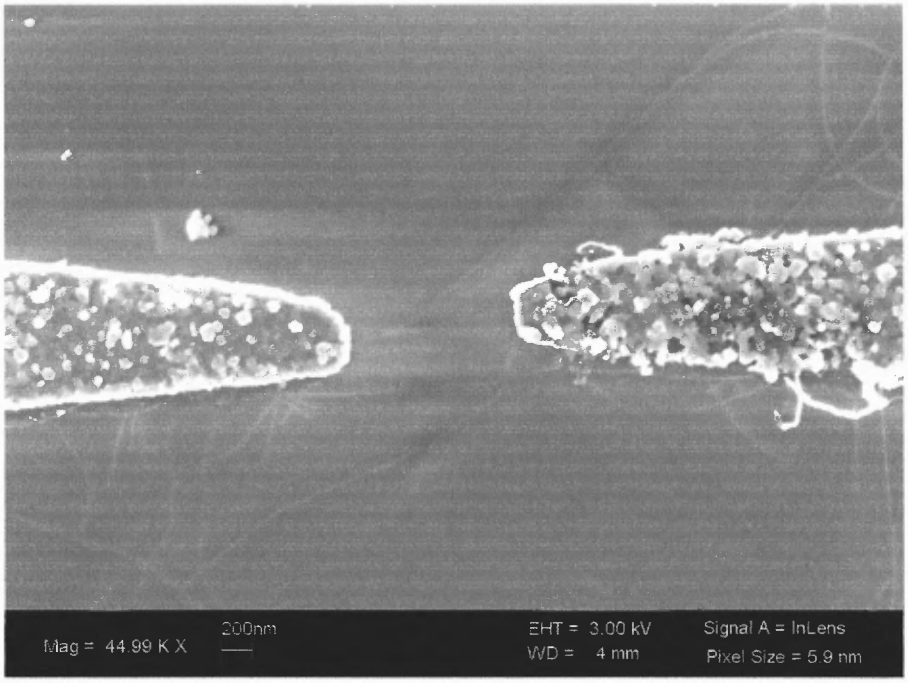
Mag = 44.99 K X
200nm
EHT = 3.00 kV
WD = 4 mm
Signal A = InLens
Pixel Size = 5.9 nm

(a)

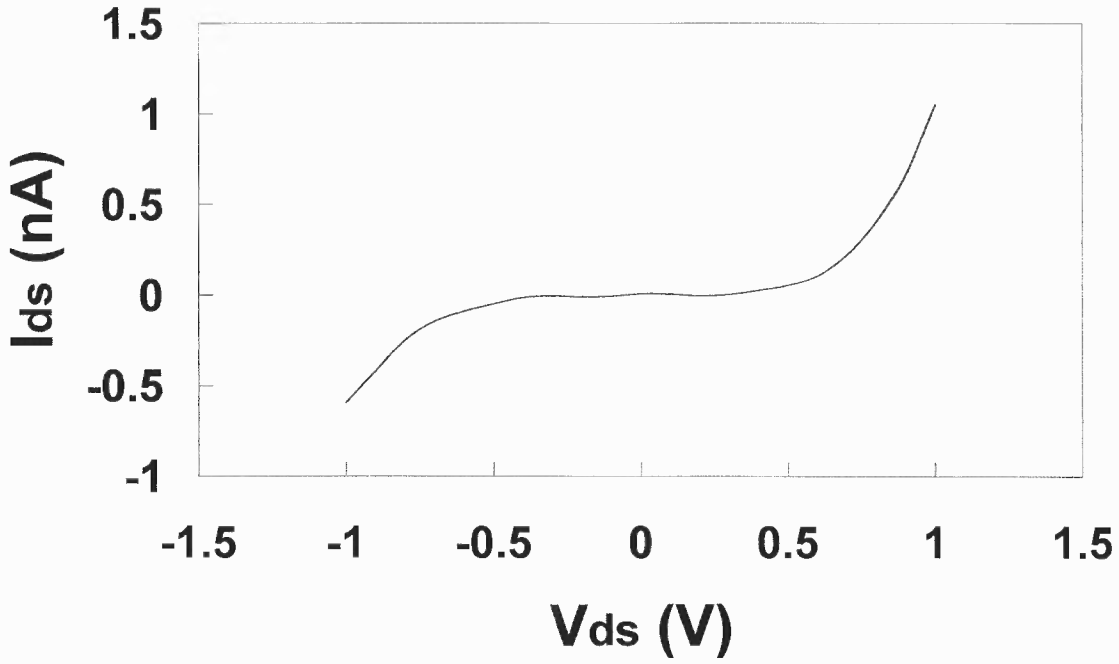
1.5
1
0.5
0
-0.5
-1
Ids (nA)
-1.5
-1
-0.5
0
0.5
1
1.5
Vds (V)

(b)

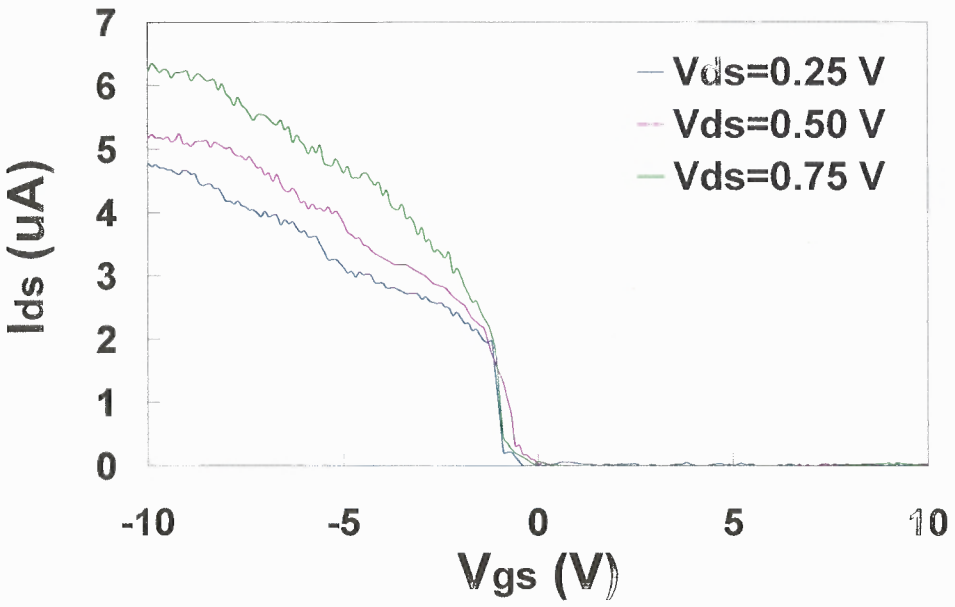

(c)

Figure 5.6 Examples of carbon nanotube intra-connects (a) SEM image (b) I_{ds}-V_{ds} characteristics; non-linear (c) I_{ds}-V_{gs} characteristics [84].

CHAPTER 6

SWCNT/PCZ

Devices made by individual CNT intra-connect have gained much interest since diameter of a CNT is just a few nanometers [90-92]. CNTs are functionalized with various conducting polymers for doping, sensors, FET, photovoltaic cell, organic light emitting devices, solar cell, etc [93-96]. However, functionalization has been studied mostly for bulk CNTs and relatively fewer works were devoted for single CNT since the growth of CNT between pre-defined positions is a challenging task [13]. Here, we present individually addressable CNT based FET which were functionalized with polycarbazole (PCZ) aiming at optical sensor applications. The CNT intra-connect was grown by chemical vapor deposition (CVD) and later electroplated with PCZ. Electrical properties, such as I_{ds}-V_{ds} and I_{ds}-V_{gs} characteristics were measured under dark and white light illumination. The effects of biasing and photosensitivity were assessed for both CNT and PCZ-plated intra-connects.

6.1 I_{ds}-V_{ds} Characteristics and Raman Spectra

Current-voltage (I_{ds}-V_{ds}) characteristics were measured from V_{ds}=-1 to +1 Volts under dark and white light illumination (150 mW/cm^2, >400 nm) for both CNT and PCZ-plated CNT intra-connect (Figure 6.1(a) and (c)). In both cases, the overall currents were increased when irradiated with white light. After electroplating the CNT intra-connect with PCZ, photosensitivity was greatly enhanced, by nearly ten times. Figure 6.1(b) and (d) show Raman spectra from the CNT and PCZ-plated CNT intra-connects, respectively. The radial

breathing mode (RBM) was located at 191.9 cm^{-1}. The peak corresponds to a metallic tube (12,6) with an average diameter of 1.252 nm (Figure 6.1(b)) [34], however, as mentioned before, the high-frequency peaks indicate semiconducting bridge. Figure 6.1(d) corroborates the existence of electroplated PCZ on the CNT intra-connect.

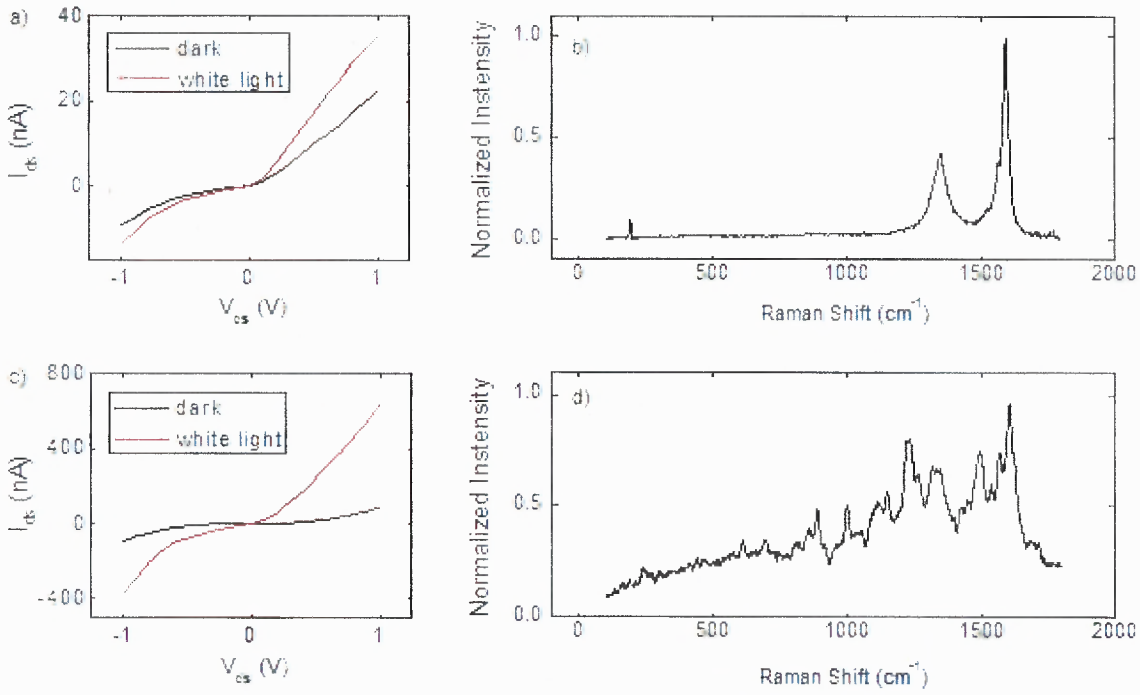

Figure 6.1 (a) I_{ds}-V_{ds} characteristics from individually addressable CNT intra-connect at dark and when exposed to white light irradiation. (b) Raman spectra from single CNT channel. The RBM peak is located at 191.9 cm^{-1}. (c) I_{ds}-V_{ds} characteristics from individually addressable CNT intra-connect wrapped with PCZ. at dark and under white light illumination. (d) Raman spectra from individually addressable CNT intra-connect wrapped with PCZ.

6.2 NDR in I_{ds}-V_{gs} Characteristics and Photoconductance

Figure 6.2(a) shows a current map of V_{gs} vs. V_{ds} for non-illuminated PCZ-plated intra-connect. Two negative differential resistance (NDR) regions are observed in the I_{ds}-V_{gs} curve as well: one in the range between 3 and –6 V and another around –9 V (Figure 6.2(b) and (c)). The NDR peak for the first region was shifting albeit in both negative and positive directions as V_{ds} increased from 0.25 V to 0.75 V. The second NDR region was stable around –9 V. The same intra-connect under illumination is shown in Figure 6.2(d)-(f). Here, the light somewhat masked the NDR effect (Figure 6.2(f)) for the first V_{gs} region but left a small but noticeable NDR effect around $V_{gs} \sim -9$ V. The differential optical conductance (the difference between conductance under darkness and light) was stable and exhibited a marked increase for increasing V_{ds} (Figure 6.2(g)).

Figure 6.3 shows the stability of current under dark and the sensitivity to white light when it was turned on and off, repeatedly. Figure 6.3(a) shows the stability of current at DC voltage of V_{ds}=1 V. The curve was featureless and the current was constant. The response to white light illumination was immediate (Figure 6.3(b)). Figure 6.3(c) shows the effect of current stability under a DC drain-source voltage of V_{ds}=1 V for PCZ-plated CNT intra-connects. The current increased and then saturated. The response to white light illumination is shown in Figure 6.3(d). The current increases immediately at the moment that white light was turned on, then, it exponentially decreased. The effect is due to the long life-time of the photo-excited charges in PCZ.

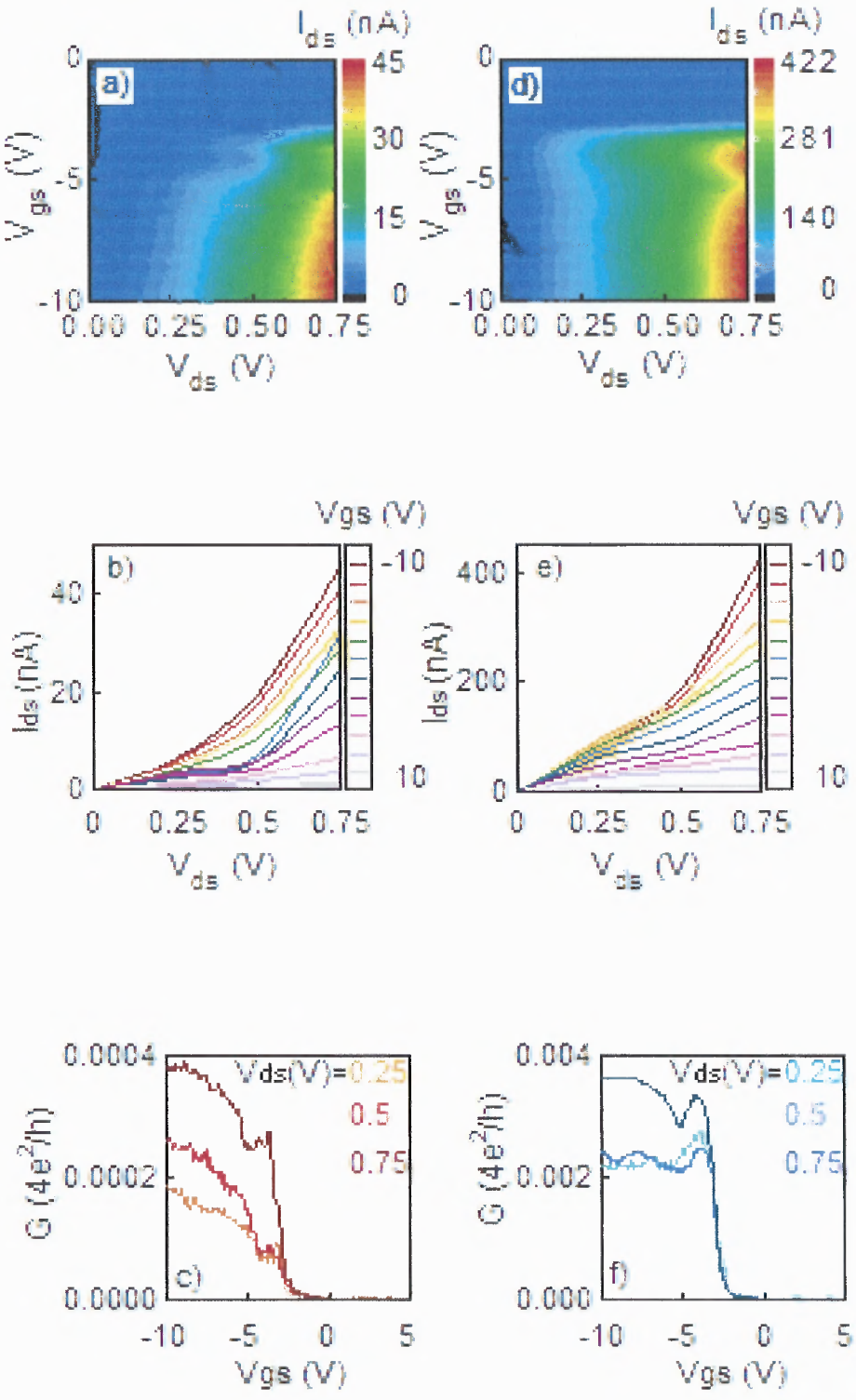
a)
d)
I_{ds} (nA)
45
30
15
0
422
281
140
0
V_{gs} (V)
0
-5
-10
0.00 0.25 0.50 0.75
V_{ds} (V)
b)
e)
Vgs (V)
-10
10
I_{ds} (nA)
40
20
0
400
200
0 0.25 0.5 0.75
c)
f)
Vds(V)=0.25
0.5
0.75
G ($4e^2/h$)
0.0004
0.0002
0.0000
0.004
0.002
0.000
-10 -5 0 5
Vgs (V)

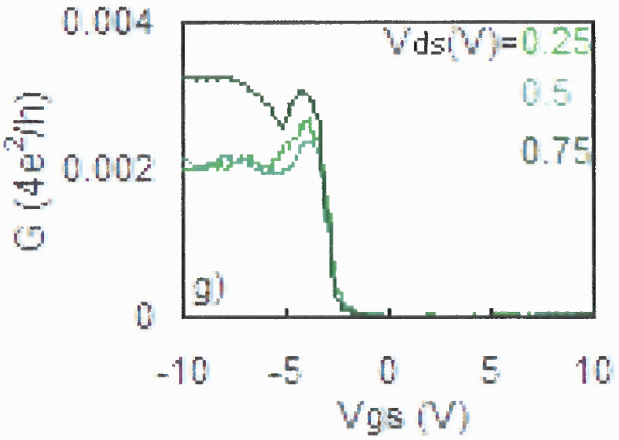

Figure 6.2 Electrical properties of CNT FET wrapped with PCZ under dark and white light illumination. (a) I_{ds} vs. V_{gs} and V_{ds} characteristics. Negative differential resistance was observed for V_{gs} between -2 and -6. (b) I_{ds}-V_{ds} characteristic for various V_{gs} values, from +10 to -10. I_{ds}-V_{ds} curves become nonlinear when gate voltages were applied. (c) G-V_{gs} characteristics. Figure 6.2a is converted into conductance, G (d) I_{ds} vs. V_{gs} and V_{ds} characteristics after irradiation of white light. (e) I_{ds}-V_{ds} characteristic for various V_{gs} values, from +10 to -10 Volts. I_{ds}-V_{ds} curves become nonlinear when gate bias was applied. (f) G-V_{gs} characteristics under white light illumination. (g) Differential photo-conductance.

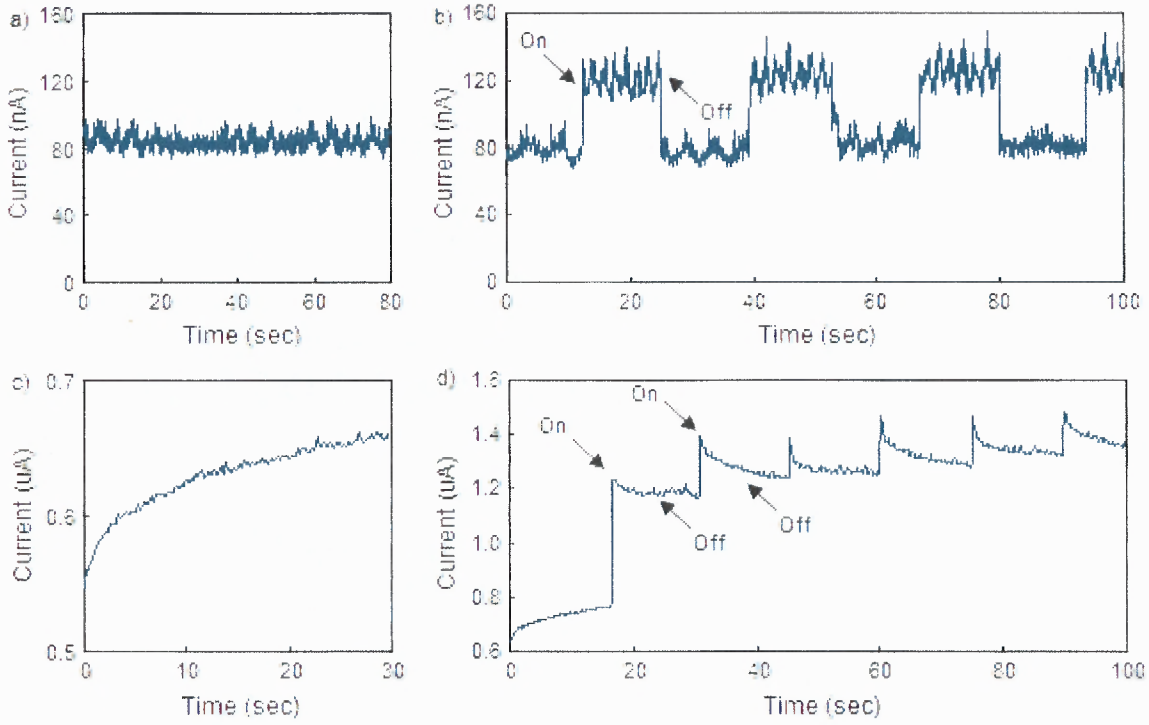

Figure 6.3 (a) Effect of biasing on individually addressable CNT intra-connect (V_{ds}=1V). (b) Sensitivity for white light illumination. (c) Effect of biasing on CNT intra-connect wrapped with PCZ. V_{ds}=1 V (d) Sensitivity to white light illumination.

CHAPTER 7

CONCLUSION

In this thesis, low-dimensional gated structures were investigated. The channel were based on carbon nanotube intra-connects. These were grown on pre-determined positions on a wafer by use of chemical vapor deposition (CVD) without any post-processing. Growth conditions were varied to obtain multi-walled carbon nanotubes (MWCNT), or single-walled carbon nanotubes (SWCNT) intra-connects. High yield, as high as 50%, was achieved for this growth technique.

Electroplated MWCNT with polypyrrole were successfully fabricated between two electrodes for potential electro-optic and bio-sensor applications. For the latter, a large response to a binding event is desired [29]. Such response may be enabled if the channel mobility dramatically changes from a very large value (channel saturation, Fig. 4.5(b) curve (2)) to a very small value (where initial linear behavior is observed, Fig. 4.5(b) curve (1)). These considerations dictate that the polymer thickness ought to be smaller than 80 nm.

Negative differential resistance (NDR) was demonstrated with carbon nanotube gated structures under bias regardless of the linearity (or nonlinearity) of the contacts. The effect was accompanied by a large differential phoconductance (DPC) effect. Since NDR enables the realization of microwave oscillators, one may envision that such DPC will be instrumental in designing new high-speed opto-electronic oscillators.

CHAPTER 8

FUTURE WORK

Controlled growth of carbon nanotubes remains a challenge despite advances in the field, part of which was described in this thesis. Negative differential resistance (NDR) is an important phenomenon, which may prove useful for future high-speed nano-optoelectronic devices: it deserves further exploration.

REFERENCES

[1] H. Boo, R.-A. Jeong, S. Park, K. S. Kim, K. H. An, Y. H. Lee, J. H. Han, H. C. Kim, and T. D. Chung, "Electrochemical Nanoneedle Biosensor Based on Multiwall Carbon Nanotube," *Analytical Chemistry,* vol. 78, p. 617, 2006.

[2] J. A. Misewich, R. Martel, P. Avouris, J. C. Tsang, S. Heinze, and J. Tersoff, "Electrically Induced Optical Emission from a Carbon Nanotube FET," *Science,* vol. 300, p. 783, 2003.

[3] H. W. C. Postma, T. Teepen, Z. Yao, M. Grifoni, and C. Dekker, "Carbon Nanotube Single-Electron Transistors at Room Temperature," *Science,* vol. 293, p. 76, 2001.

[4] M. Meyyappan, "Carbon nanotubes: Science and Applications," CRC Press, 2004.

[5] P. Chandrasekhar., "Conducting Polymers, Fundamentals and Applications: A Practical Approach," *Kluwer Academic, Boston,* p. 760, 1999.

[6] S. Iijima, "Helical microtubules of graphitic carbon," *Nature,* vol. 354, p. 56, 1991.

[7] R. H. Baughman, C. Cui, A. A. Zakhidov, Z. Iqbal, J. N. Barisci, G. M. Spinks, G. G. Wallace, A. Mazzoldi, D. De Rossi, A. G. Rinzler, O. Jaschinski, S. Roth, and M. Kertesz, "Carbon Nanotube Actuators," *Science,* vol. 284, p. 1340, 1999.

[8] G. Cellot, E. Cilia, S. Cipollone, V. Rancic, A. Sucapane, S. Giordani, L. Gambazzi, H. Markram, M. Grandolfo, D. Scaini, F. Gelain, L. Casalis, M. Prato, M. Giugliano, and L. Ballerini, "Carbon nanotubes might improve neuronal performance by favouring electrical shortcuts," *Nat Nano,* vol. 4, p. 126, 2009.

[9] E. W. Wong, P. E. Sheehan, and C. M. Lieber, "Nanobeam Mechanics: Elasticity, Strength, and Toughness of Nanorods and Nanotubes," *Science,* vol. 277, p. 1971, 1997.

[10] M.-F. Yu, O. Lourie, M. J. Dyer, K. Moloni, T. F. Kelly, and R. S. Ruoff, "Strength and Breaking Mechanism of Multiwalled Carbon Nanotubes Under Tensile Load," *Science,* vol. 287, p. 637, 2000.

[11] J. W. G. Wilder, L. C. Venema, A. G. Rinzler, R. E. Smalley, and C. Dekker, "Electronic structure of atomically resolved carbon nanotubes," *Nature,* vol. 391, p. 59, 1998.

[12] M. S. Dresselhaus, G. Dresselhaus, P. Avouris, "Carbon nanotubes: Synthesis, Structure, Properties and Applications," *Springer-Verlag, Berlin,* 2001.

[13] X. Liu, J. Ly, S. Han, D. Zhang, A. Requicha, M. E. Thompson, C. Zhou, "Synthesis and Electronic Properties of Individual Single-Walled Carbon Nanotube/Polypyrrole Composite Nanocables," *Advanced Materials,* vol. 17, p. 2727, 2005.

[14] J. Kong, H. T. Soh, A. M. Cassell, C. F. Quate, and H. Dai, "Synthesis of individual single-walled carbon nanotubes on patterned silicon wafers," *Nature,* vol. 395, p. 878, 1998.

[15] H. Shirakawa, E. J. Louis, A. G. MacDiarmid, C. K. Chiang and A. J. Heeger, "Synthesis of electrically conducting organic polymers: halogen derivatives of polyacetylene, (CH)x," *J. Chem. Soc., Chem. Commun.,* p. 578, 1977.

[16] T. A. Skotheim, R. L. Elsenbaumer, J. R. Reynolds, "Handbook of Conducting Polymers, 2nd ed," *Marcel Dekker, New York,* p. 1097, 1998.

[17] C. C. Bof Bufon and T. Heinzel, "Polypyrrole thin-film field-effect transistor," *Applied Physics Letters,* vol. 89, 012104, 2006.

[18] J. Wang, Y. L. Bunimovich, G. Sui, S. Savvas, J. Wang, Y. Guo, J. R. Heath and H.-R. Tseng, "Electrochemical fabrication of conducting polymer nanowires in an integrated microfluidic system," *Chemical Communications,* 2006.

[19] K. H. An, S. Y. Jeong, H. R. Hwang, Y. H. Lee, "Enhanced Sensitivity of a Gas Sensor Incorporating Single-Walled Carbon Nanotube-Polypyrrole Nanocomposites," *Advanced Materials,* vol. 16, p. 1005, 2004.

[20] M. J. Sailor, C. L. Curtis, "Conductiong polymer connections for molecular devices," *Advanced Materials,* vol. 6, p. 688, 1994.

[21] C. R. Martin, "Template Synthesis of Electronically Conductive Polymer Nanostructures," *Accounts of Chemical Research,* vol. 28, p. 61, 1995.

[22] A. Varesano, L. Dall'Acqua, and C. Tonin, "A study on the electrical conductivity decay of polypyrrole coated wool textiles," *Polymer Degradation and Stability,* vol. 89, p. 125, 2005.

[23] H. H. Kuhn, A. D. Child, and W. C. Kimbrell, "Toward real applications of conductive polymers," *Synthetic Metals,* vol. 71, p. 2139, 1995.

[24] A. M. Waller, R. G. Compton, *J. Chem. Soc., Faraday Trans.,* vol. 85, 1989.

[25] P. S. Heeger and A. J. Heeger, "Making sense of polymer-based biosensors," *Proceedings of the National Academy of Sciences of the United States of America,* vol. 96, p. 12219, 1999.

[26] K. Ramanathan, M. A. Bangar, M. Yun, W. Chen, A. Mulchandani, and N. V. Myung, "Individually Addressable Conducting Polymer Nanowires Array," *Nano Letters,* vol. 4, p. 1237, 2004.

[27] H. X. He, C. Z. Li, and N. J. Tao, "Conductance of polymer nanowires fabricated by a combined electrodeposition and mechanical break junction method," *Applied Physics Letters,* vol. 78, p. 811, 2001.

[28] J. Liu, Y. Lin, L. Liang, J. A. Voigt, D. L. Huber, Z. R. Tian, E. Coker, B. Mckenzie and M. J. Mcdermott, "Templateless Assembly of Molecularly Aligned Conductive Polymer Nanowires: A New Approach for Oriented Nanostructures," *Chemistry - A European Journal,* vol. 9, p. 604, 2003.

[29] M. A. Prelas, G. Popovici and L. K. Bigelow, "Handbook of Industrial Diamonds and Diamond Films," *New York,* 1997.

[30] B. T. Kelly, "Physics of Graphite," *Applied Science, London,* 1981.

[31] T. R. Ohno, G. H. Kroll, J. H. Weaver, L. P. F. Chibante, R. E. Smalley, "Doping of C60 with iodine," *Nature,* vol. 355, p. 401, 1992.

[32] H. W. Kroto, J. R. Heath, S. C. O'Brien, R. F. Curl, and R. E. Smalley, "C60: Buckminsterfullerene," *Nature,* vol. 318, p. 162, 1985.

[33] R. Saito, G. Dresselhaus and M. S. Dresselhaus, "Physical properties of carbon nanotubes," *Imperial College Press,* 1998.

[34] R. Krupke, F. Hennrich, H. Lohneysen, and M. M. Kappes, "Separation of Metallic from Semiconducting Single-Walled Carbon Nanotubes," *Science,* vol. 301, p. 344, 2003.

[35] J. J. Davis, K. S. Coleman, B. R. Azamian, C. B. Bagshaw, M. L. H. Green, "Chemical and Biochemical Sensing with Modified Single Walled Carbon Nanotubes," *Chemistry - A European Journal,* vol. 9, p. 3732, 2003.

[36] S. S. Wong, E. Joselevich, A. T. Woolley, C. L. Cheung and C. M. Lieber, "Covalently functionalized nanotubes as nanometresized probes in chemistry and biology," *Nature,* vol. 394, p. 52, 1998.

[37] S. Iijima and T. Ichihashi, "Single-shell carbon nanotubes of 1-nm diameter," *Nature,* vol. 363, p. 603, 1993.

[38] D. S. Bethune, R. D. Johnson, J. R. Salem, M. S. de Vries, and C. S. Yannoni, "Atoms in carbon cages: the structure and properties of endohedral fullerenes," *Nature,* vol. 366, p. 123, 1993.

[39] A. Thess, R. Lee, P. Nikolaev, H. Dai, P. Petit, J. Robert, C. Xu, Y. H. Lee, S. G. Kim, A. G. Rinzler, D. T. Colbert, G. E. Scuseria, D. Tomanek, J. E. Fischer, and R. E. Smalley, "Crystalline Ropes of Metallic Carbon Nanotubes," *Science,* vol. 273, p. 483, 1996.

[40] M. Wilson, "Nanotechnology: Basic Science and Emerging Technologies," 2002.

[41] B. I. Yakobson and R. E. Smalley, *American Scientist,* vol. 85, p. 324, 1997.

[42] T. W. Ebbesen and P. M. Ajayan, "Large-scale synthesis of carbon nanotubes," *Nature,* vol. 358, p. 220, 1992.

[43] C. D. Scott, S. Arepalli, P. Nikolaev and R.E. Smalley, "Growth mechanisms for single-wall carbon nanotubes in a laser-ablation process," *Applied Physics A: Materials Science & Processing,* vol. 72, p. 573, 2001.

[44] T. Guo, P. Nikolaev, A. Thess, D. T. Colbert, and R. E. Smalley, "Catalytic growth of single-walled manotubes by laser vaporization," *Chemical Physics Letters,* vol. 243, p. 49, 1995.

[45] B. C. Satishkumar, A. Govindarajb, R. Sen and C.N.R Rao, "Single-walled nanotubes by the pyrolysis of acetylene-organometallic mixtures " *Chemical Physics Letters,* vol. 293, p. 47, 1998.

[46] R. Sen, A. Govindarajb and C. N. R. Rao, "Carbon nanotubes by the metallocene route," *Chemical Physics Letters,* vol. 267, p. 276, 1997.

[47] Z. F. Ren, Z. P. Huang, J. W. Xu, J. H. Wang, P. Bush, M. P. Siegal, and P. N. Provencio, "Synthesis of Large Arrays of Well-Aligned Carbon Nanotubes on Glass," *Science,* vol. 282, p. 1105, 1998.

[48] M. S. Dresselhaus, G. Dresselhaus, and R. Saito, "Carbon fibers based on C60 and their symmetry," *Physical Review B,* vol. 45, p. 6234, 1992.

[49] M. S. Dresselhaus, G. Dresselhaus and P. Eklund, "Science of Fullerenes and Carbon Nanotubes," *Academic, San Diego,* 1996.

[50] Q. Cao and J. A. Rogers, "Ultrathin Films of Single-Walled Carbon Nanotubes for Electronics and Sensors: A Review of Fundamental and Applied Aspects," *Advanced Materials,* vol. 21, p. 29, 2009.

[51] S. Kim, S. Ju, J. H. Back, Y. Xuan, P. D. Ye, M. Shim, D. B. Janes and S. Mohammadi, "Fully Transparent Thin-Film Transistors Based on Aligned Carbon Nanotube Arrays and Indium Tin Oxide Electrodes," *Advanced Materials,* vol. 21, p. 564, 2009.

[52] Q. Cao, H.-S. Kim, N. Pimparkar, J. P. Kulkarni, C. Wang, M. Shim, K. Roy, M. A. Alam, and J. A. Rogers, "Medium-scale carbon nanotube thin-film integrated circuits on flexible plastic substrates," *Nature,* vol. 454, p. 495, 2008.

[53] R. Saito, G. Dresselhaus, and M. S. Dresselhaus, "Trigonal warping effect of carbon nanotubes," *Physical Review B,* vol. 61, p. 2981, 2000.

[54] P. R. Wallace, "The Band Theory of Graphite," *Physical Review,* vol. 71, p. 622, 1947.

[55] J. W. McClure, "Diamagnetism of Graphite," *Physical Review,* vol. 104, p. 666, 1956.

[56] J.-C. Charlier and J.-P. Issi, "Electronic structure and quantum transport in carbon nanotubes " *Applied Physics A: Materials Science & Processing,* vol. 67, p. 79, 1998.

[57] M. Bockrath, D. H. Cobden, P. L. McEuen, N. G. Chopra, A. Zettl, A. Thess, and R. E. Smalley, "Single-Electron Transport in Ropes of Carbon Nanotubes," *Science,* vol. 275, p. 1922, 1997.

[58] S. Frank, P. Poncharal, Z. L. Wang and W. A. de Heer, "Carbon Nanotube Quantum Resistors," *Science,* vol. 280, p. 1744, 1998.

[59] S. J. Tans, M. H. Devoret, H. Dai, A. Thess, R. E. Smalley, L. J. Geerligs, and C. Dekker, "Individual single-wall carbon nanotubes as quantum wires," *Nature,* vol. 386, p. 474, 1997.

[60] H. T. Soh, C. F. Quate, A. F. Morpurgo, C. M. Marcus, J. Kong, and H. Dai, "Integrated nanotube circuits: Controlled growth and ohmic contacting of single-walled carbon nanotubes," *Applied Physics Letters,* vol. 75, p. 627, 1999.

[61] P. J. F. Harris, "Carbon Nanotubes and Related Structures," *Cambridge University Press,* 2002.

[62] A. Hagen and T. Hertel, "Quantitative Analysis of Optical Spectra from Individual Single-Wall Carbon Nanotubes," *Nano Letters,* vol. 3, p. 383, 2003.

[63] S. Reich, C. Thomsen and J. Maultzsch, "Carbon Nanotubes: Basic Concepts and Physical Properties," *Wiley-VCH,* 2004.

[64] A. M. Rao, E. Richter, S. Bandow, B. Chase, P. C. Eklund, K. A. Williams, S. Fang, K. R. Subbaswamy, M. Menon, A. Thess, R. E. Smalley, G. Dresselhaus, and M. S. Dresselhaus, "Diameter-Selective Raman Scattering from Vibrational Modes in Carbon Nanotubes," *Science,* vol. 275, p. 187, 1997.

[65] http://nobelprize.org. (April 20, 2009)

[66] http://www.chemistrydaily.com. (April 20, 2009)

[67] M. P. Stevens, "Polymer Chemistry," *Oxford University Press,* 1999.

[68] Y. Furukawa, S. Tazawa, Y. Fujii, and I. Harada, "Raman spectra of polypyrrole and its 2,5-13C-substituted and C-deuterated analogues in doped and undoped states," *Synthetic Metals,* vol. 24, p. 329, 1988.

[69] H. Macit, S. Sen and M. Sacak, "Electrochemical synthesis and characterization of polycarbazole," *Journal of Applied Polymer Science,* vol. 96, p. 894, 2005.

[70] Y. Diamant, J. Chen, H. Han, B. Kamenev, L. Tsybeskov and H. Grebel, "Electrochemical polymerization, optical and electrical characterization of polycarbazole on single wall carbon nanotubes," *Synthetic Metals,* vol. 151, p. 202, 2005.

[71] C. Zhou, J. Kong, E. Yenilmez, and H. Dai, "Modulated Chemical Doping of Individual Carbon Nanotubes," *Science,* vol. 290, p. 1552, 2000.

[72] R. Martel, T. Schmidt, H. R. Shea, T. Hertel, and P. Avouris, "Single- and multi-wall carbon nanotube field-effect transistors," *Applied Physics Letters,* vol. 73, p. 2447, 1998.

[73] C. Zhou, J. Kong, and H. Dai, "Electrical measurements of individual semiconducting single-walled carbon nanotubes of various diameters," *Applied Physics Letters,* vol. 76, p. 1597, 2000.

[74] F. Leonard and J. Tersoff, "Multiple Functionality in Nanotube Transistors," *Physical Review Letters,* vol. 88, 258302, 2002.

[75] F. Leonard and J. Tersoff, "Novel Length Scales in Nanotube Devices," *Physical Review Letters,* vol. 83, p. 5174, 1999.

[76] F. Leonard and J. Tersoff, "Role of Fermi-Level Pinning in Nanotube Schottky Diodes," *Physical Review Letters,* vol. 84, p. 4693, 2000.

[77] V. Gomis, D. Bellver, N. Ferrer-Anglada, J. M. Rib, Z. El-Hachemi, and B. Movaghar, "Negative differential resistance and sample conductivity in polypyrrole films," *Synthetic Metals,* vol. 156, p. 1083, 2006.

[78] A. Javey, J. Guo, Q. Wang, M. Lundstrom, and H. Dai, "Ballistic carbon nanotube field-effect transistors," *Nature,* vol. 424, p. 654, 2003.

[79] B. O. Agboola, "Catalytic activities of Metallophthalocyanines towards Detection and Transformation of Pollutants," *PhD Thesis, Rhodes University,* 2007.

[80] S. W. Lee, A. Kornblit, D. Lopez and H. Grebel, "Electrical and optical properties of carbon nanotube/polypyrrole addressable intra-connects," *Synthetic Metals,* vol. 159, p. 462, 2009.

[81] T.-M. Wu and S.-H. Lin, "Synthesis, characterization, and electrical properties of polypyrrole/multiwalled carbon nanotube composites," *Journal of Polymer Science Part A: Polymer Chemistry,* vol. 44, p. 6449, 2006.

[82] R. J. Chen, N. R. Franklin, J. Kong, J. Cao, T. W. Tombler, Y. Zhang, and H. Dai, "Molecular photodesorption from single-walled carbon nanotubes," *Applied Physics Letters,* vol. 79, p. 2258, 2001.

[83] L. Valentini, I. Armentano, J. M. Kenny, S. Bidali and A. Mariani, "Interaction of oxygen with nanocomposites made of n-type conducting polymers and carbon nanotubes: role of charge transfer complex formation between nanotubes and poly(3-octylthiophene)," *Thin Solid Films,* vol. 476, p. 162, 2005.

[84] S. W. Lee, A. Kornblit, D. Lopez, S. V. Rotkin, A. A. Sirenko, and H. Grebel, "Negative Differential Resistance: Gate Controlled and Photoconductance Enhancement in Carbon Nanotube Intraconnects," *Nano Letters,* vol. 9, p. 1369, 2009.

[85] T. Durkop, T. Brintlinger, M. S. Fuhrer, H. Kuzmany, J. Fink, M. Mehring and S. Roth "Structural and Electronic Properties of Molecular Nanostructures," *AIP Conference Proceedings,* p. 242, 2002.

[86] E. Garcia-camarero, F. Arjona, C. Guillien, E. Fatas and C. Montemayor, "On the electrical anisotropy of conducting polypyrrole," *J. Mater. Sci,* vol. 25, p. 4914, 1990.

[87] A. Jorio, A. G. Souza Filho, G. Dresselhaus, M. S. Dresselhaus, A. K. Swan, M. S. Unlu, B. B. Goldberg, M. A. Pimenta, J. H. Hafner, C. M. Lieber, and R. Saito, "G-band resonant Raman study of 62 isolated single-wall carbon nanotubes," *Physical Review B,* vol. 65, p. 155412, 2002.

[88] D. Katz, D. Lopez, A. Kornblit, H. Grebel, "Carbon Nanotubes Bridges Spanning Across Metal Electrode Tips," *Journal of Nanoscience and Nanotechnology,* vol. 8, p. 4382, 2008.

[89] D. Katz, S.-W. Lee, D. Lopez, A. Kornblit, H. Grebel, "Synthesis of Carbon Nanotubes: Controlled Interconnects Growth.," *J. Vac. Sci. and Tech., B,* vol. B25, p. 1191, 2007.

[90] J. Cao, Q. Wang, D. Wang and H. Dai, "Suspended Carbon Nanotube Quantum Wires with Two Gates," *Small,* vol. 1, p. 138, 2005.

[91] A. Javey, J. Guo, M. Paulsson, Q. Wang, D. Mann, M. Lundstrom, and H. Dai, "High-Field Quasiballistic Transport in Short Carbon Nanotubes," *Physical Review Letters,* vol. 92, 106804, 2004.

[92] T. W. Tombler, C. Zhou, L. Alexseyev, J. Kong, H. Dai, L. Liu, C. S. Jayanthi, M. Tang, and S.-Y. Wu, "Reversible electromechanical characteristics of carbon nanotubes under local-probe manipulation," *Nature,* vol. 405, p. 769, 2000.

[93] Z. Xu, Y. Wu, B. Hu, I. N. Ivanov, and D. B. Geohegan, "Carbon nanotube effects on electroluminescence and photovoltaic response in conjugated polymers," *Applied Physics Letters,* vol. 87, 263118-3, 2005.

[94] H. S. Woo, R. Czerw, S. Webster, D. L. Carroll, J. Ballato, A. E. Strevens, D. O'Brien, and W. J. Blau, "Hole blocking in carbon nanotube--polymer composite organic light-emitting diodes based on poly (m-phenylene vinylene-co-2, 5-dioctoxy-p-phenylene vinylene)," *Applied Physics Letters,* vol. 77, p. 1393, 2000.

[95] M. W. Rowell, M. A. Topinka, M. D. McGehee, H.-J. Prall, G. Dennler, N. S. Sariciftci, L. Hu, and G. Gruner, "Organic solar cells with carbon nanotube network electrodes," *Applied Physics Letters,* vol. 88, 233506-3, 2006.

[96] M. C. Kum, K. A. Joshi, W. Chen, N. V. Myung, and A. Mulchandani, "Biomolecules-carbon nanotubes doped conducting polymer nanocomposites and their sensor application," *Talanta,* vol. 74, p. 370, 2007.